
UNIVERSIDADE D
COIMBRA

Tânia Patrícia de Almeida Sousa

# Photophysical Processes of Tetrazolones: A Theoretical Approach Based on DFT and TD-DFT

**Dissertação no âmbito do Mestrado em Biologia Computacional orientada pelo Professor Doutor Pedro Jorge dos Santos Branco Caridade e co-orientada pelo Professor Doutor Carlos Alberto Lourenço de Serpa Soares apresentada ao Departamento de Ciências da Vida da Faculdade de Ciências e Tecnologia da Universidade de Coimbra.**

Julho de 2023

# Photophysical Processes of Tetrazolones: A Theoretical Approach Based on DFT and TD-DFT

UNIVERSIDADE D
COIMBRA

Dissertação no âmbito do Mestrado em Biologia Computacional orientada pelo Professor Doutor Pedro Jorge dos Santos Branco Caridade e co-orientada pelo Professor Doutor Carlos Alberto Lourenço de Serpa Soares apresentada ao Departamento de Ciências da Vida da Faculdade de Ciências e Tecnologia da Universidade de Coimbra

Tânia Patrícia de Almeida Sousa

July 25, 2023

# Abstract

In this work a characterization of the photophysical processes of 1-phenyl-4-allyl-tetrazol-5-one (ATZ), 1-phenyl- 4-ciclohexanyl-tetrazol-5-one (CTZ) and 1-phenyl-4-(3-methyl–cylohexanyl)-tetrazol-5-one (3CTZ) is carried out in methanol at the density functional theory (DFT) and time-dependent DFT (TD-DFT) level of theory. The latter characterization is done based on two different methods for rate constant computation: path integral approach (PIA) and Fourier simplified transformed formula (FSTF). In general both methods yielded similar results, allowing the conclusion that the non-radiative processes are dominant over the radiative ones for all the approached tetrazolones. Due to the possibility of two photochemical pathways of intramolecular proton transfer in CTZ and 3CTZ, an energy analysis of the minimal energy path (MEP), of both ways, is carried out using Nudget Elastic Band (NEB) method. Parallel to the NEB, a study on the use of molecular polarizability as a marker for selectivity was also performed. The results from the two analysis are in agreement, with the intramolecular proton transfer by the cyclohexanyl group in CTZ being the most probable path to take place since it produces the more energetically stable product and with the lowest polarizability value. Regarding 3CTZ, results show that the product with lower polarizability and energetically more stable is formed when the intramolecular proton transfer takes places by the phenyl group. Because there are evidences that show a correlation between the molecular polarizability and the dielectric constant of the solvent (polarity), a final study was performed in order to address if in other protic solvents with different dielectric constants the chosen path would still be the same. The results show that with an increase of the solvent's polarity there was also an increase in the molecule's polarizability value. Regarding the influence on the choice of photochemical path, the chosen intramolecular proton transfer groups were the same as in methanol, cyclohexanyl for CTZ and transfer by the phenyl group for 3CTZ.

***Keywords***— Tetrazolones, photophysical processes, DFT and TD-DFT,NEB, polarizability.

# Resumo

Neste trabalho foi realizada a caracterização dos processos fotofísicos da 1-fenil-4-alil-tetrazol-5-ona (ATZ), 1-fenil-4-ciclohexanil-tetrazol-5-ona (CTZ) e 1-fenil-4-(3-metil-ciclohexanil)-tetrazol-5-ona (3CTZ) em metanol ao nível da teoria de *Density Functional Theory (DFT)* e *Time-Dependent DFT (TD-DFT)*. O cálculo das constantes de velocidade de cada processo foi feito com duas abordagens diferentes: *Path Integral Approach (PIA)* e *Fourier Simplified Transformed Formula (FSTF)*. De forma geral, ambos os métodos produziram resultados similares sendo a principal conclusão de que existe uma predominância dos processos não-radiativos sobre os radiativos para todas as tetrazolonas estudadas.

Pelo facto de a transferência intramolecular do protão na CTZ e 3CTZ se poder dar por duas vias diferentes (grupo ciclohexanil ou fenil) foi levada a cabo uma análise energética do caminho de energia mínima, de ambas os caminhos, recorrendo ao *Nudget Elastic Band (NEB)*. Em paralelo realizou-se também um estudo na utilização da polarizabilidade molecular com um marcador na seletividade de vias fotoquímicas. Ambas as análises permitiram concluir que a transferência de protão intramolecular é favorecida pelo grupo ciclohexanil na CTZ sendo a via com as espécies energeticamente mais estáveis e que leva à formação do produto com menor polarizabilidade molecular (menor reatividade). Relativamente à 3CTZ, a via favorecida é com transferência de protão pelo grupo fenil.

Por último, foi realizado um estudo na correlação do efeito da polaridade do solvent na polarizabilidade molecular. O objetivo passou por tentar perceber se para solventes próticos com diferentes polaridades (constantes dielétricas) a escolha das vias para a transferência intramolecular de protão na CTZ e 3CTZ permaneceria a mesma. Os resultados desta análise permitiram concluir que, de facto, com o aumento da polaridade do solvente existe também um aumento da polarizabilidade molecular. No que toca às duas opções de via fotoquímica, para a CTZ a transferência de protão pelo grupo ciclohexanil prevalece tal como para a 3CTZ se mantém a transferência de protão pelo grupo fenil.

***Palavras-Chave***— Tetrazolonas, processos fotofísicos, DFT, TD-DFT, NEB, polarizabilidade.

# Dedication

To Austin, Vó Mina and Scott.

# Acknowledgements

I would like to start by thanking professors Pedro Jorge dos Santos Branco Caridade and Carlos Alberto Lourenço de Serpa Soares for the opportunity of doing my master's thesis with them and for all the knowledge and experience that I was able to retrieve.

To my mother, father, brother and grand parents I do not have words to express my gratitude for all your love and support through out this last six years. Particularly to my parents, your sacrifice to provide me this opportunity is not, and never will, be forgotten. I do love you all with all of my heart.

To my boyfriend, and best friend, Daniel all the pages in this master's thesis would not be enough to write down how much I am grateful for having you by my side, for you love, patience, kindness and comprehension. I do love you dearly. To my cat Shiva, although you are small and unable to read this, I would like you to know that without you all my college years would have been unbearable, thank you for existing. Mommy loves you!

António, one of my beloved and trusted friends, I can not thank you enough for the support and companionship through out this amazing, and crazy, experience. I really do hope that you find peace and may this world be kind to you as you deserve.

Nuno Brito, you know what I wanted to write down but let's just say " Good job :) " at being one of my dearest friends. I wish you all the happiness in this world, thanks for everything.

To Gil, Giorgio, Filipe and Maria thank you for all the fun and laughs in our endless nights and afternoons of Magic the Gathering and Dungeons and Dragons, it really was key to escape the tiredness of these last year's reality.

To Sofia, and Marcos, two incredible people that I have in my life, that helped me, and guided me in my most difficult and darkest times. If I was able to carry out this master's work its because of you. Thank you!

Bohdana and Carolina, my oldest, trusted and beloved friends you know how much our friendship means to me. I love you so much, thank you for everything!

I would like to finish my acknowledges by thanking to my former professor João Gil, a person that I take as an idol in the scientific world and, more importantly, a very close friend. You are by my side since the first year of my Bachelor's degree, and never let me give up and stop believing in myself. I can today recognize that, in fact, I do have the fiber to do it! This work is also for you!

# Contents

# Acronyms

**3CTZ** 1-phenyl-4-(3-methyl–cylohexanyl)-tetrazol-5-one

**5Z** Quintuple Zeta

**AO** Atomic Orbital

**ATZ** 1-phenyl-4-allyl-tetrazol-5-one

**CTZ** -phenyl- 4-ciclohexanyl-tetrazol-5-one

**CPCM** Conductor-Like Polarizable Continuum Model

**DFT** Density Functional Theory

**DRE** Duschinsky Rotation Effect

**FC** Franck-Condon

**FCP** Franck-Condon Principle

**FSTF** Fourier Simplified Transformed Formula

**GGA** Generalised Gradient Approximation

**GTO** Gaussian Type Orbital

**HZ** Herzberg-Teller

**HK** Hohenberg-Kohn

**IC** Internal Conversion

**ISC** Inter-System Crossing

**KS** Kohn-Sham

**LDA** Local Density Approach

**MO** Molecular Orbital

**meta-GGA** meta-Generalised Gradient Approximation

**MHP** Maximum Hardness Principle

**NEB** Nudget Elastic Band

**PIA** Path Integral Approach

**QZ** Quadropole Zeta

**RISC** Reverse Inter-System Crossing

**RG** Runge and Gross

**SOC** Spin-Orbit Coupling

**STO** Slater Type Orbital

**TD-DFT** Time Dependent Density Functional Theory

**TDPT** Time Dependent Perturbation Theory

**TF** Thomas-Fermi

**TZ** Triple Zeta

**ZPE** Zero Point Energy

# List of Figures

# List of Tables

# Chapter 1

# Structural and photochemical analysis of tetrazolones

Before studying the photophysical processes of a molecular system it is important to grasp and understand its structural and physical-chemical properties and photochemical pathways in order to allow a holistic comprehension of the results.

With this in mind, this chapter presents a structural analysis of tetrazole compounds and their photophysical properties.The latter will be followed by an introduction to tetrazole's isomer distribution in different phases, applications of tetrazole compounds and a perspective of tetrazolones as a substituted tetrazole.

Later on a detailed analysis of 1-phenyl-4-allyl-tetrazol-5-one (ATZ), 1-phenyl-4-ciclohexanyl-tetrazol-5-one (CTZ) and 1-phenyl-4-(3-methyl–cylohexanyl)-tetrazol-5-one (3CTZ) photochemical pathways will be carried out.

To conclude the study of tetrazolone's photochemistry a brief discussion on the relevance of computational and theoretical studies to provide a better understanding of the photo-mechanistic intricacies to overcome some limitations regarding tetrazolone's photochemical applications, is presented.

## 1.1 Introduction

The combination of simple natural resources to produce new and more complex compounds dates back to pre-historic ages where humans combined different pigments, such as ochre, with vegetable oils to produce ink for rock art.

With the human evolution, the technology had remarkable advances that allowed the *synthesis* of highly specific compounds that could not be found in nature. Synthetic compounds are very useful not only for industrial purposes, but also for research, as they allow a better understanding of the structure of the compound itself. One good example of this are the tetrazolones.

## 1.2 Structural Properties of Tetrazoles

Tetrazolones belong to a very large family of molecules called tetrazoles. Tetrazole compounds are part of a class of synthetic molecules structurally characterized by the presence of a five member ring composed by four nitrogen atoms and one carbon atom.

Among the group of stable unsubstituted heterocyclic systems, the tetrazole's ring conformation with no substitutions holds the highest number of nitrogen atoms. Due to this structural feature, tetrazoles exhibit some of their most common physical chemical properties such as extreme values of acidity, complex formation constants and basicity [1].

The ring directly bounded hydrogen atoms can easily undergo cleavage[1], *i.e.*, have labile character, thus allowing the existence of three structural isomers: 1H-tetrazole (1H), 2H-tetrazole (2H) and 5H-tetrazole (5H) shown in Figure 1.1.

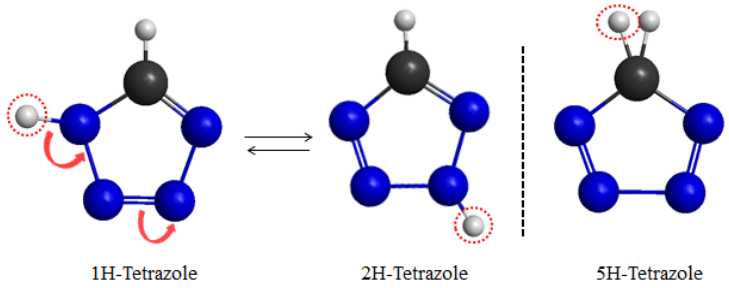


Figure 1.1: Isomerization mechanism of 1H-Tetrazole (left) to 2H-Tetrazole (center) and 5H-Tetrazole (right).

The 1H, and 2H isomers are also said to be tautomers since they coexist in an equilibrium and can easily interconvert [2–4]. Especially for the tetrazole family, *annular tautomerism* is the most common type of interconversion due to the diverse positions that the proton can have within the heterocyclic system [1, 5, 6].

## 1.3 Population distribution of tetrazole isomers

Experimental research based on X-ray diffraction methods, have shown that in the solid state only 1H was detected [2, 7]. In the liquid phase, particularly in polar solutions such as water, dimethylsulfoxide (DMSO), dimethylformamide (DMF), dioxane and acetone, 1H was also confirmed to be the dominant species [8–10]. Photo-electronic [11] and mass spectroscopy [2] studies stipulated that 2H would be the predominant isomer in the gas phase. Later, with the use of Infrared (IR) spectroscopy and electronic structure calculations, it was possible to conclude that, in fact, 2H dominates in the gaseous phase [12].

It was also shown that the dielectric constant ($\varepsilon$) of different media could also interfere with the 1H, 2H tautomeric equilibrium. For instance, 1H is dominant in solutions with $\varepsilon \geq 7$ [13] whereas 2H has the lowest energy for solutions with $\varepsilon < 7$ [13, 14].

Regarding 5H isomer, although it is suggested to be a detectable species [15], until now, no experimental observations have been made.

## 1.4 Applications of tetrazole compounds

In the last decades, the use of tetrazoles throughout medicine [16, 17], highly energetic materials [18–20], coordination chemistry [21–24] and imaging technology [25–27] has become more popular. Furthermore, tetrazole compounds have come to play a key role in agriculture as regulators of both plant maturation and undesired vegetation and as fungicides[28].

More recently, these compounds also emerged as a new target for pharmaceutical industries to produce antihistamine [29], pain-relieving[30], anti-inflammatory[31], antibiotic[32] and anti-high blood pressure drugs[33–36]. Particularly in the medicinal chemistry field, tetrazoles also possess a very wide range of applications due to the possibility of acting as a chemical substitute , *i.e bioisosteres*, for the carboxylic acid[37–41].

This replacement is possible because tetrazoles allow similar receptor-ligand interactions as they exhibit chemical-physical properties common to those of the carboxilic acid, such as size, electrostatic potential and behaviour of both acid and base [42]. As an added advantage for the pharmaceutical and medicinal chemistry fields, tetrazole compounds have an easier penetration into the cellular membrane since they have a more delocalized charge and exhibit a higher lipophilic behaviour[43–45].

## 1.5 Tetrazolones as a substituted tetrazol

Based on where and how many substitutions are carried out within the tetrazole's ring, it is possible to classify tetrazole's derivatives as: 1-, 2-, 5- monosubstituted; 1,5-, 1,4- or 2,5- disubstituted and trisubstituted tetrazolium salts.

Particularly relevant for the work on this thesis is the subclass of 5-monosubstituted tetrazoles, or tetrazol-5-one, also known as tetrazolones.

Tetrazolones are structurally characterized by the presence of a carbonyl group, at the ring's $5^{th}$ position, and also for the popular substitutions on the $1^{st}$ and $4^{th}$ positions. Figure 1.2 below shows a schematic representation of 1H-tetrazole and a tetrazol-5-one for structural comparison.

Throughout this thesis, an extensive and detailed study will be carried out on three species of tetrazolones, 1-phenyl-4-allyl-tetrazol-5-one (ATZ), 1-phenyl-4-ciclohexanyl-tetrazol-5-one (CTZ) and 1-phenyl-4-(3-methyl-cyclohexanyl)-tetrazol-5-one (3CTZ), whose chemical structures are schematized below in figures 1.3, 1.4 and 1.5.

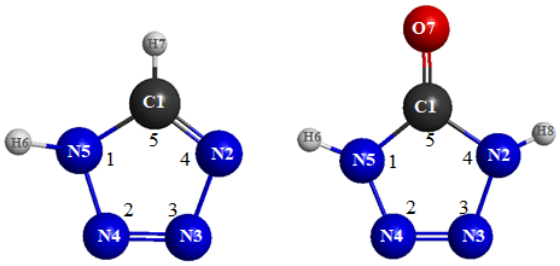


Figure 1.2: Structural comparison between a unsubstituted tetrazol (left) and tetrazol-5-one (right).

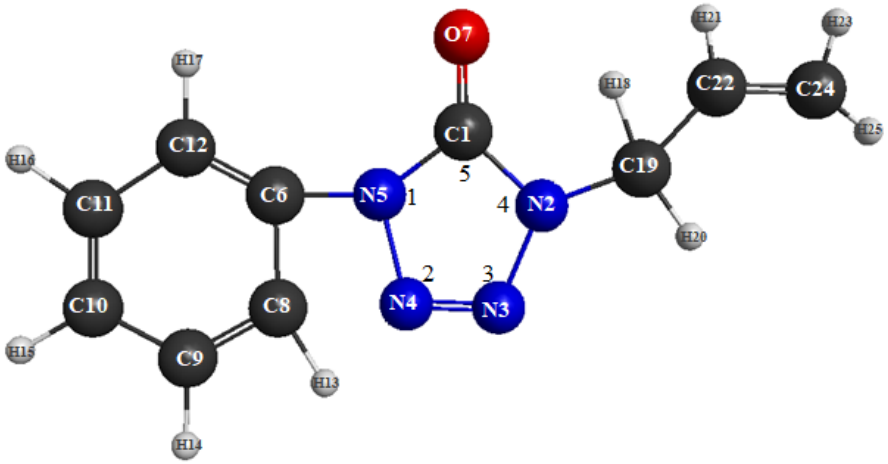


Figure 1.3: Chemical structure of ATZ.

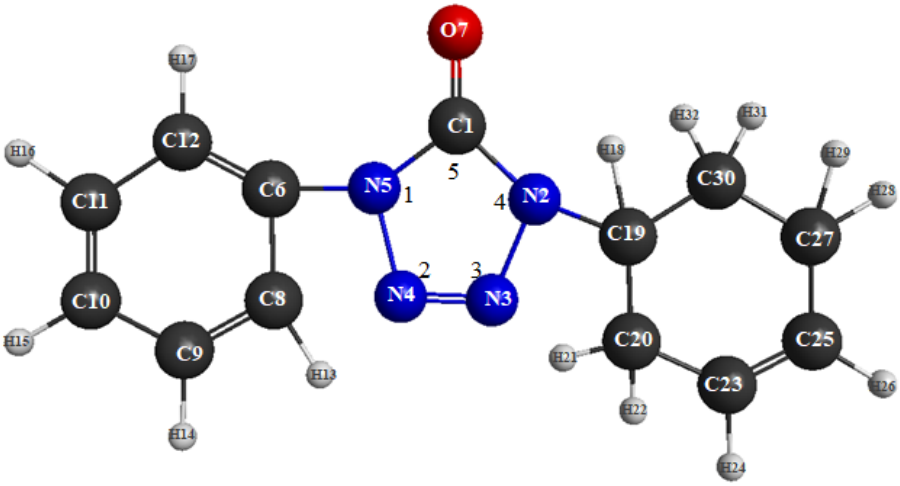


Figure 1.4: Chemical structure of CTZ.

Regarding tetrazolone's applications, as a member of the family of tetrazole compounds, they exhibit similar physical properties as tetrazoles and hence have similar applications. Particularly for tetrazolones their use is more extensive within the chemical synthesis, coordination chemistry and highly energetic chemistry areas[46, 47].

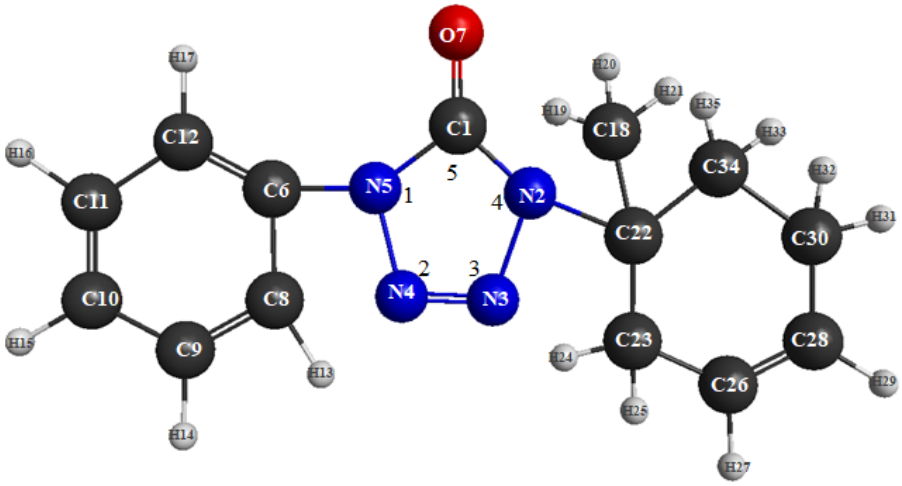


Figure 1.5: Chemical structure of 3CTZ.

## 1.6 A closer look into the main photochemical mechanisms of tetrazole compounds

After photon absorption, the most common photochemical pathway of tetrazole compounds is the tetrazole's ring cleavage with or without molecular nitrogen ($N_2$) photo-extrusion[48, 49]. The later process occurs, typically, in one of two ways: in a single step, a new ring of three members is forged by means of a concerted mechanism[50, 51] in two steps with the formation of radicals and zwitterionic species[50, 51].

The resulting products from ring cleavage are typically azides, aziridines and isocyanites[47, 52, 53], the amount of which is majorly determined by the conformational flexibility of the ring's substituent groups [48, 49, 54–57].

The presence of labile hydrogen atoms, directly bound to the ring or in the substituent groups, can also give rise to other photochemical pathways such as photo-induced tautomerism [48, 49]. Very often in tetrazole compounds it is found that the above described photochemical pathways can take place simultaneously[48, 49].

## 1.7 Photochemistry of ATZ

Regarding ATZ's subfamily, their photochemistry is mainly composed of five pathways packed with a vast array of products such as, isocyanates, anilines, azides, azacycloheptatetraenes, diaziridinones, pyrimidones and benzimidazolones[47, 52, 53].

A relevant aspect on ATZ's photochemistry is whether the solvent has the ability to form hydrogen bonds with itself, *i.e.*, protic solvent, or if it has not, *i.e.*, aprotic solvent. For instance, pyrimidones, can only be obtained with protic solvents. This is because an extra stabilization of the product

comes to play due to the hydrogen bonds between the solvent and the pyrimidone. Furthermore, the latter interaction can also favor the deactivation of the excited state through reversible proton-transfer mechanisms [58]. On the other hand, with the use of an aprotic solvent, the latter process evolves to the formation of isocyanates and anilines[47, 50].

If the pathway is centered on the tetrazole's ring cleavage then isocyanates and azides are produced. In the particular case of azides formation process, if the ring cleavage is followed by $N_2$ photo-extrusion azacycloheptatetraenes will be formed. It is also possible that only $N_2$ photo-extrusion takes place, and when it does, diaziridinones and benzimidazolones are the expected products.

Besides the effects of solvent and the conformational details on ATZ's photochemistry, there is another aspect that can narrow the choice of the pathway which is where the reaction takes place: matrix or solution. The study of photochemical reactions in matrix narrows the number of pathways due to the spacial restrictions imposed by the matrix itself. Due to this feature, mechanisms that include big conformational changes, or $N_2$ diffusion can become quite limited, such examples are the mechanisms of azacycloheptatetraenes and diaziridinones production[52]. The work on this thesis will be focused on the pyrimidone's formation process from ATZ, in a protic solvent, specifically methanol. Figure (1.6) below shows a schematic representation of pyrimidone formation process in methanol.

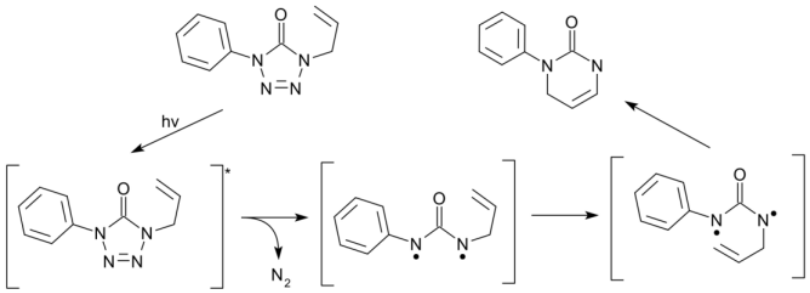


Figure 1.6: Photochemical mechanism of ATZ in methanol adapted from[50, 59].

ATZ photochemical pathway in methanol starts with the photo absorption by the ground state followed by a transition to an excited state. Within the excited state $N_2$ extrusion takes place which leads to the formation of a triplet biradical intermediate [50, 59]. Through a conformational change in the allyl group, of the latter intermediate, and an intramolecular proton-transfer mechanism[50] the pyrimidone is formed.

## 1.8 Photochemical pathway of CTZ

CTZ photochemical pathway is very similar to ATZ. The main difference between these two mechanisms is regarding the carbon atom where the proton-transfer takes place. In the case of CTZ this transfer occurs in the first unsaturated carbon leading to the formation of a five member ring and not a six member ring as it is in ATZ. Figure 1.7 shows a schematic representation of CTZ photochemical

pathway in a protic solvent.

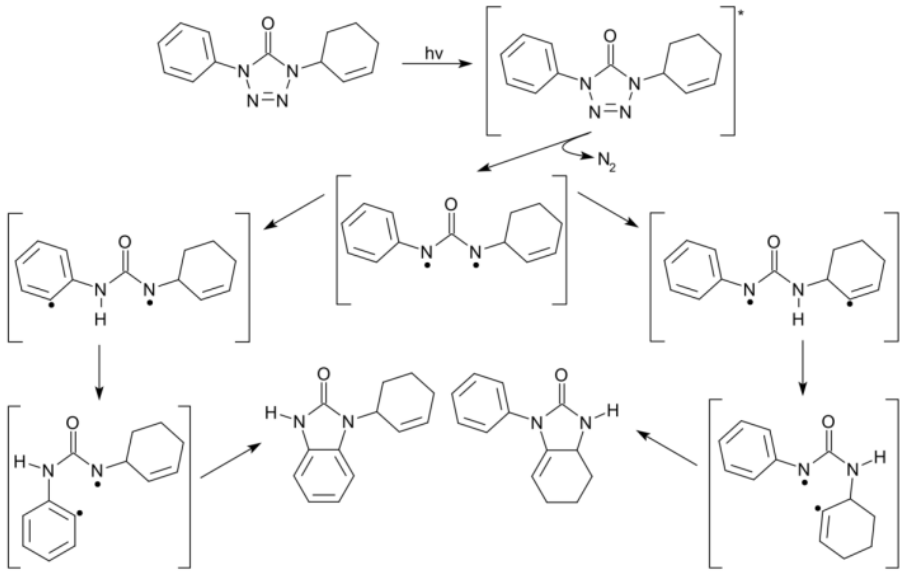


Figure 1.7: Photochemical mechanism of CTZ in methanol adapted from[47]

Analysing CTZ's photochemical pathway it is possible to notice that after the formation of the birradical triplet the intramolecular pronto transfer happen by the cyclohexanyl or phenyl group, leading to the formation of a pyrimidone or benzimidazolone, respectively.

## 1.9 Photochemical pathway of 3CTZ

In the case of 3CTZ, the substitution of the allyl group by a methyl group induces steric hindrance which in turn leads to the formation of a benzimidazolone as a product[47].

Although a divergence exists between 3CTZ and CTZ mechanisms, these two photochemical pathways possess *two similarities*: formation of a triplet biradical intermediate and the proton-transfer.

For 3CTZ the intermediate structural change happens in the phenyl and the mechanism of proton-transfer takes place between the carbon atom of the phenyl group and the nitrogen atom bound to it. Figure 1.8 shows a schematic representation of 3CTZ photochemical pathway in a protic solvent (methanol).

Similarly to CTZ, in 3CTZ one also has the presence of two possible paths for the intramolecular proton transfer step, by the cyclohexanyl or the phenyl group.

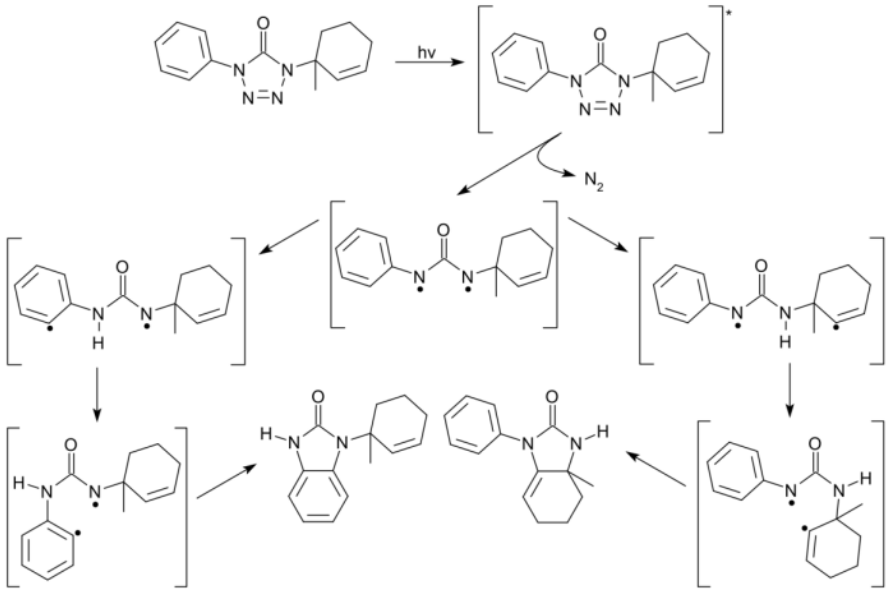


Figure 1.8: Photochemical mechanism of 3CTZ in methanol adapted from[47].

## 1.10 Photochemistry of tetrazole compounds ... a challenge?

Despite their wide range of applications, tetrazole's photochemistry remains a puzzle for photochemists[60], the reason for this being the vast number of photodegradation pathways that this family of molecules possesses.

Particularly for synthetic implementations, the use of tetrazole compounds can become a rather formidable task since the aim of this field is to achieve high yields and selectivity[60]. One way to overcome these limitations is through the better understanding of the mechanistic intricacies of tetrazole's photochemical pathways.

This knowledge can be acquired through computational calculations and theoretical studies of the latter mechanisms. The interpretation, and comparison, of different properties such as stability, energy barriers and rate constants of different photophysical processes can help to elucidate which mechanisms are more dominant and more likely to take place.

# Chapter 2

# Photophysical processes: a theoretical overview

Photophysical processes are light-matter interaction dependent phenomena. Hence, a good understanding of the latter mechanisms are crucial to properly discuss these processes.

This chapter presents the basic theoretical and fundamental concepts of light-matter interactions and electronic state transitions, such as the excited electronic state availability, population distribution and Fermi's golden rule. The study of electronic state transitions will be completed with the presentation of the transition rules.

To conclude, the last part of the chapter will be focused on approach the main excited state deactivation mechanisms.

## 2.1 Introduction

The human contact with the chemical effects of light, *i.e.*, *photochemistry*, dates back to the Bronze Age with the dyeing of clothes with Tyrian purple. Phoenicians collected the precursor of the dye from the gland of a snail shellfish and exposed it to sunlight to give rise to a color change from a yellowish color to a deep purple. Understanding the interaction of light with matter began in the early seventeenth century, with the study of the nature of light. At that time, Sir Isaac Newton performed experiments that made him believe that light was composed of colored particles. In the same century, Christiaan Huygens put forward the theory that light was a wave, later corroborated by Thomas Young with his double-slit experiment. In the nineteenth century James Clerk Maxwell developed his theory of electrodynamics that predicted the existence of electromagnetic waves. It was only in the twentieth century that the dual behavior of light was proven and that Albert Einstein described light as photons.

## 2.2 Interaction of light with matter

When a photon interacts with matter, *e.g*, a molecular system, there are five different possible interaction mechanisms: *absorption*, *emission*, *scattering*, *transmission* and *reflection*. Throughout this thesis only absorption and emission mechanisms will be covered in detail in order to aid further understanding of the rate constant derivation and emission spectra.

Due to energy quantization [61], photon absorption can only occur if the frequency of the incident photon is *equal* to the energy difference between the involved energy levels. After photon absorption the molecular system is shifted from its lowest energy state, *i.e.*, *fundamental state*, to a more energetic state called an *excited state*.

## 2.3 Availability of excited states and population distribution

The number of electronic excited states that are available at a certain temperature, in thermal equilibrium [62], is given by the *partition function (Z)*[63],

$$Z = \sum_i g_i \exp\left(-\frac{E_i}{k_B T}\right) \tag{2.1}$$

where $k_B$ is the Boltzmann constant, $T$ is temperature, $g_i$ is the degeneracy and $E_i$ is the energy of the state $i$. Although the term $E_i$ was previously presented as the energy of state $i$, it can also be attributed as the energy of electronic, vibrational and rotational levels.

Generally the value of the partition function is bigger than one but, in the special case of the energy gap between states being large with respect to $k_B T$, the ground state will be the most populated state [63] and $Z = 1$. The *probability* of the system to be in a specific state $i$, at thermal equilibrium[62], is given by the *Boltzmann distribution*[63],

$$P_i = g_i \exp\left(-\frac{E_i}{k_B T}\right) Z^{-1} \tag{2.2}$$

with the probability distribution function $P_i$ being normalized in such way that $\sum_i P(i) = 1$. Gathering all the information, one piece is still missing to properly discuss photophysical processes, the *transition between states*.

## 2.4 Fermi's golden rule

The probability of a transition to occur *per* unit time, *i.e.*, *transition rate*, of a quantum system is given by the Fermi's Golden rule[64],

$$\kappa_{if} = \frac{2\pi}{\hbar} \langle \phi_i | \hat{H} | \phi_f \rangle^2 \delta(E_i - E_f) \tag{2.3}$$

where $\kappa_{if}$ is the rate constant of the transition, $\hbar$ is the reduced Planck's constant, $\hat{H}$ is the operator that describes the interaction between the two states, *i.e.*, *coupling* and $\phi_i$, $\phi_f$, $E_i$, $E_f$ are the wave functions and energy of the initial and final states, respectively.

Photophysical processes are associated with *electronic transitions* which are photon-electron interaction dependent mechanisms. To describe transitions of this nature one must switch to the framework of time dependent perturbation theory (TDPT)[65]to be able to answer the question *"how does the quantum system evolve in time when perturbed?"* This change is useful because in electronic transitions the photon acts as a perturbation to the system. Thus eq (2.3) can be adapted in light of TDPT as[66],

$$\kappa(\omega)_{if} = \frac{4\omega^3 n^2}{3\hbar c^3} \langle \phi_i | \hat{\mu} | \phi_f \rangle^2 \delta(E_i - E_f \pm \hbar\omega) \tag{2.4}$$

with $\omega$ being the photon frequency, $n$ the solvent's refractive index, $c$ the speed of light and $\hat{\mu}$ the dipole operator, or *transition moment*[1]. The reason why there is a change in the operator from eq (2.3) to eq (2.4) is because in photon-electron interactions the dominant component is the electric dipole transition[63]. Although there are numerous states between which transitions can take place, not all of them are allowed.

## 2.5 Transition rules

*Selection rules*, also called *transition rules*, are a set of constrains that dictate which transitions are plausible. To understand these rules one must first take a step back and look in greater detail to the transition moment. Because the photon absorption occurs in a much faster time scale than nuclear movement, the operator in eq (2.4) can be expressed as a product of three integrals[63],

$$\hat{M} = \int \phi_i \hat{\mu} \phi_f \mathrm{d}\tau_\mathrm{e} \int \mathrm{S_i S_f d}\tau_\mathrm{S} \int \theta_\mathrm{i} \theta_\mathrm{f} \mathrm{d}\tau_\mathrm{N} \tag{2.5}$$

where the first term is the electronic transition moment, the second and third terms are the spin and nuclear vibration overlap integrals, respectively. If the transition moment is zero the transition is *forbidden* otherwise is said to be *allowed*. Even though some transitions are called forbidden, it does not mean that they do not occur, but rather that their spectral intensity will be lower[67] since the intensity is proportional to the squared value of $\hat{M}$ [63].

Nonetheless, it is more frequent to see the electronic transitions' intensity (strength) expressed in terms of the oscillator strength, $f_\mathrm{oscillator}$, [63], an dimensionless quantity that can be defined as,

$$f^{ab}_\mathrm{oscillator} = \frac{2m_e\omega_{ab}}{3\hbar e^2} |M_{ab}|^2 \tag{2.6}$$

[1]From now on the transition dipole moment will be denoted with $\hat{M}$ to avoid possible confusion with the dipole moment $\vec{\mu}$

where $a, b$ denote the states involved in the transition, $m_e$ is the electron mass and charge, respectively, $\omega_{ab}$ is the transition frequency and $M_{ab}$ the transition dipole moment. Strong transitions vary in the range of $0.1 < f_{\text{oscillator}} < 1$ and the weak ones in $10^{-2} < f_{\text{oscillator}} < 10^{-6}$[63]. Another interesting feature of allowed and forbidden transitions is their *time scale*.

The lifetime ($\Gamma$) of a decaying mechanism is defined as $\Gamma = \sum_i k(\omega)_{if}^{-1}$, meaning that transitions with high rate constants (large values of M) have a short lifetime, *i.e.*, are fast[68]. For this reason, forbidden transitions are characteristically slower than allowed transitions.

Selection rules belong to one of two types: *spin* or *symmetry*. The *spin selection rule* states that if the transition has spin multiplicity conservation, *i.e* singlet-singlet or triplet-triplet transitions, the integral $\int S_i S_f \mathrm{d}\tau_{\mathrm{S}}$ is equal to the unity and the transition is *spin allowed*[63]. For transitions with no spin multiplicity conservation $\int S_i S_f \mathrm{d}\tau_{\mathrm{S}}$ is zero, due to the orthogonality of $S_i S_f$, and the transition is *spin forbidden*[63].

However, in some cases, the interaction between the spin and the orbital angular momentum, *i.e.*, *spin-orbit coupling*, can be strong enough to "lift" this prohibition and allow the mix of states with different spin multiplicities. Spin-forbidden transitions become more intense as the atomic number increases[69] because the spin-orbit coupling is more prominent than in light atoms, also known as the *heavy atom effect*.

Particularly for molecular systems with an inversion center, *i.e.*, *centrosymmetric*, the *symmetry rule*, or *Laporte rule*, constrains the electronic transitions based on *parity conservation*. To understand how one must take a closer look at the first term of eq (2.5). Because $\hat{\mathrm{M}}$ is defined in a Cartesian reference system[67], the transition dipole moment can also be separated into its three odd Cartesian components[67],

$$\int \phi_i \hat{\mu} \phi_f \mathrm{d}\tau_{\mathrm{e}} = \int \phi_{\mathrm{i}} \hat{\mu}_{\mathrm{x}} \phi_{\mathrm{f}} \mathrm{d}\tau_{\mathrm{e}} + \int \phi_{\mathrm{i}} \hat{\mu}_{\mathrm{y}} \phi_{\mathrm{f}} \mathrm{d}\tau_{\mathrm{e}} + \int \phi_{\mathrm{i}} \hat{\mu}_{\mathrm{z}} \phi_{\mathrm{f}} \mathrm{d}\tau_{\mathrm{e}} \tag{2.7}$$

If *both* $\phi_i$ and $\phi_f$ are *even or odd*, the integrating function will also be *odd* because $\hat{\mu}$ is odd[67]. Thus the integral in eq (2.7) is zero and the transition is *symmetry-forbidden*[67]. Otherwise, if there is no parity conservation the integrating function is even, the outcome of eq (2.7) is non-zero and the transition is *symmetry-allowed*[67]. From a molecular point of view this means that transitions between $s-s, d-d, p-p$ orbitals are symmetry-forbidden and between $s-p, p-d, d-f$ are symmetry-allowed.

Even though the latter are forbidden transitions, sometimes it is possible for them to appear as low intensity bands, the reason being the interaction between the vibrational and electronic levels, *i.e.*, *vibronic coupling*, and the *orbital mixing*[63, 67, 69]. For example, in metallic complexes, the vibronic coupling can lead to a momentaneaous break of symmetry and orbital mixing, thus lifting the prohibition of $d-d$ transitions. Experimental research shows that a Laporte-forbidden d-d transition tends to be much more intense than a spin-forbidden transition[69].

## 2.6 Excited state deactivation mechanisms

As previously mentioned, after photon absorption the molecular system is shifted to an excited state. The deactivation of the latter can occur through two main decay mechanisms: *radiative*, includes the emission of a photon with a wavelength bigger or equal to the excitation wavelength; *non-radiative* with no photon emission and the excess energy is converted into vibrational energy, resulting in an increase of the system's temperature. Usually during the de-excitation process, there is a competition between radiative and non-radiative pathways amid different electronic, vibrational and spin states[70].

Radiative transitions comprise *absorption, fluorescence* and *phosphorescence*, whereas non-radiative transitions include *internal conversion, inter-system crossing* and *vibrational relaxation*. All these photophysical processes are represented in an energy diagram called the *Jablonski diagram* that also contains the electronic states and the transitions amid them. Figure (2.1) shows a schematic representation of this diagram.

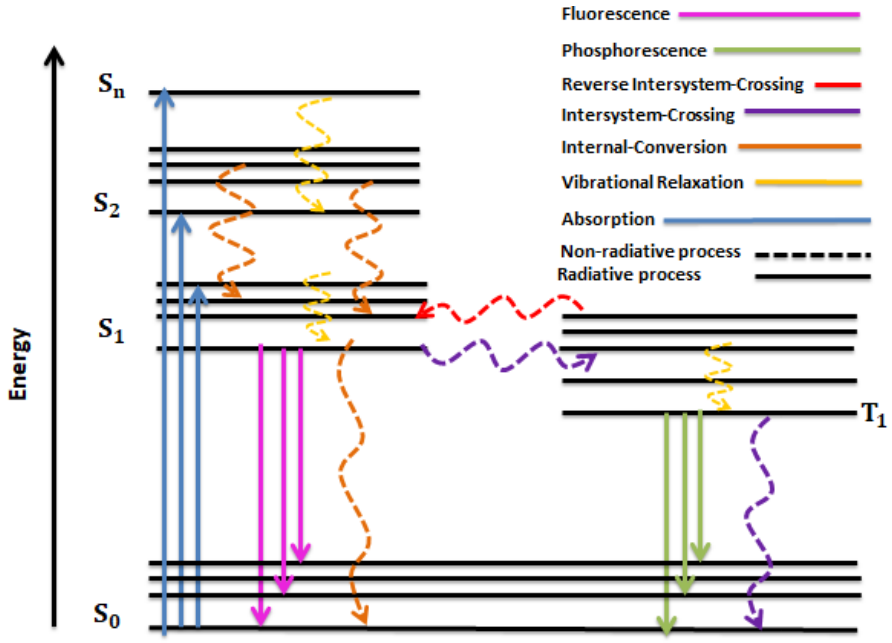


Figure 2.1: Jablonski diagram.

*Fluorescence* is a photophysical phenomenon that emerges from the interaction of the transition dipole moment between singlet spin states $S_1 - S_0$ and an electromagnetic field[70].

On the other hand, *phosphorescence* arises from the interaction of the transition dipole moment between singlet-triplet spin states $T_1 - S_0$ and an electromagnetic field[70]. It is a direct transition mechanism after *inter-system crossing* (ISC). The latter process consists of a transition from a singlet excited state to a triplet excited state or *vice versa* also called *reversed inter-system crossing* (RISC).

*Internal conversion* (IC) phenomenon happens alternatively to *vibrational relaxation* if there is a strong overlap of the vibrational and electronic levels[70, 71]. One thing remains to be analyzed, the time scale of these photophysical processes which are represented below in Table (2.1). It is now

Table 2.1: Time scales of different photophysical processes [72].

| **Photophysical process** | **Electronic Transition** | **Type** | **Time Scale** |
|---|---|---|---|
| Internal Conversion | $S_n \rightarrow S_1$ | spin allowed | $10^{-14} - 10^{-11}$ s |
| Vibrational relaxation | $S_n^* \rightarrow S_n$ | spin-allowed | $10^{-12} - 10^{-10}$ s |
| Fluorescence | $S_0 \rightarrow S_1$ | spin-allowed | $10^{-9} - 10^{-6}$ s |
| Phosphorescence | $T_1 \rightarrow S_0$ | spin-forbidden | $10^{-3} - 10^{2}$ s |
| Intersystem-Crossing | $S_1 \rightarrow T_1$ | spin-forbidden | $10^{-11} - 10^{-6}$ |

interesting to understand why some photophysical processes are faster than others. For instance, IC and vibrational relaxation are the fastest mechanisms, *i.e.*, have the smallest lifetimes, because they are allowed transitions. Fluorescence comes as an exception in this due to the strong competition with the internal conversion process.

On the other hand, ISC and phosphorescence, spin-forbidden transitions, are slower mechanisms with higher lifetimes. The reason why it is actually possible to have these processes is due to the spin-orbit coupling[73].

To each one of these photophysical processes there is an associated rate constant. The derivation and computation of the latter will be further presented in the methodology chapter.

# Chapter 3

# Electrostatics

One of the goals of this work is to test molecular polarizability as a property that can be used to understand the selectivity in photochemical reactions. This property is related to the response of a molecular system to an external electric field.

Hence, this chapter starts with the presentation of the theoretical and fundamental concepts of classical electromagnetism in order to better understand the polarizability.

The basics of classical electrostatics that will be discussed are Coulomb's law, divergence and curl of an electrostatic field, Gauss's law and electric potential.

Subsequently, the multipole expansion and rigorous definition of the dipole moment, and its induction in dielectrics, are presented to make a bridge to the definition of polarizability.

The final part of the chapter will cover the molecular polarizability as a property that can be used for selectivity studies in chemical reactions through its connection with hardness and molecular reactivity.

## 3.1 Introduction

Electrostatic phenomena have been known to mankind since ancient times. The first mention of an electrostatic phenomenon remotes back to 600 B.C., when the Greek philosopher Thales of Miletus perceived that, if rubbed, ambar could acquire the ability to pick up dust and leaves.

Later, around 300 B.C. another Greek philosopher Theophrastus found out that other materials could had electric properties. Unfortunately, neither Thales or Theophrastus had a scientific explanation for the behaviours manifested by the materials. What both philosophers understood was that every so often two objects would attract or repel each other. This observation lead to the developing of the idea of opposite charges.

Only around the eighteen century physicists started to mathematically describe the electrostatic phenomena. Later, by the end of the century the physicist Charles-Augustin de Coulomb stated the

law that would allow the quantification of the amount of force between two electric charged bodies and the discussion of the quantity of electric charge in a meaningful way.

## 3.2 Coulomb's Law

Coulomb derived its law experimentally through the use of a torsion balance to study the force of attraction/repulsion between electrically charged bodies. The aim of this experiment was to try to establish the magnitude of this interaction and its dependence on the distance between two charges.

More rigorously, Coulomb's law states that the magnitude of the electrostatic force of attraction, or repulsion, on a test charge, $Q$, at rest, due to a single point charge, $q$, is directly proportional to the product of the charges and inversely proportional to the square of the distance between them [74]

,

$$\vec{F} = \frac{1}{4\pi\epsilon_0}\frac{qQ}{r^2}\hat{r} \tag{3.1}$$

where $\epsilon_0$ is the vacuum permittivity and $r$ is the distance from $r'$ (position of the point charge) to $R$ (position of test charge Q) defined as,

$$\vec{r} = \vec{R} - \vec{r'} \tag{3.2}$$

with $r$ being its magnitude and $\hat{r}$ the direction.

Physically, the force obtained from eq (3.1) is the result of the *local* interaction of $Q$, with the electrostatic field that $q$ originates around itself in all space. Hence, the electrostatic field, $\vec{E}$, can be defined as the force *per unit* test charge at a given point,

$$\vec{E} = \frac{\vec{F}}{Q} \Leftrightarrow \vec{E} = \frac{1}{4\pi\epsilon_0}\frac{q}{r^2} \tag{3.3}$$

The vector function $\vec{E}$ has two particular characteristics: 1) *position dependence*, due to the fact that $r$ has dependence on the field location point; 2) *its direction* is considered to be the force exerted on the positive charge, i.e, for a positive source charge, $q^+$, the direction of $\vec{E}$ points radially outwards and for a negative source charge, $q^-$, points radially inwards.

So far, the scenario described by Coulomb's law only allows the computation of the force due to a single point charge but, what if there is a collection of single point charges? The answer to this question is rather simple when considering the *superposition principle*- the net feedback due to two or more stimuli is the sum of the responses that each stimulus individually would have caused[74]. Regarding our system, this means that the total force on $Q$ can be computed as,

$$\vec{F} = \vec{F_1} + \vec{F_2} + \vec{F_3} + \cdots = \frac{1}{4\pi\epsilon_0}\Big(\frac{q_1 Q}{r_1^2}\hat{r} + \frac{q_2 Q}{r_2^2}\hat{r} + \frac{q_3 Q}{r_3^2}\hat{r} + \cdots\Big) \tag{3.4}$$

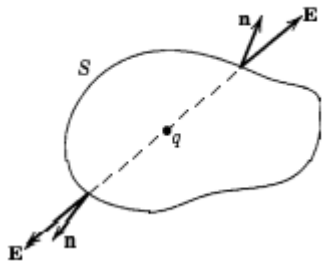


Figure 3.1: Point charge $q$ closed in a surface $S$ [75].

As consequence of that,

$$\vec{E}(\vec{r}) = \frac{1}{4\pi\epsilon_0}\sum_{i=1}^{n}\frac{q_i}{r_i^2}\hat{r_i} \tag{3.5}$$

Besides the previously mentioned characteristics of $\vec{E}$, another relevant information is the fact that it is determined by the configuration of the source charges. Nonetheless, it is important to point out that eq (3.5) assumes that the collection of charges is composed by *discrete* point charges, but it is also possible that the charges are *continuously* distributed over a region. Therefore, the sum in eq (3.5) evolves to the integral form and $\vec{E}$ can be defined as,

$$\vec{E}(\vec{r}) = \frac{1}{4\pi\epsilon_0}\int\frac{1}{r^2}\hat{r}\mathrm{d}q \tag{3.6}$$

In nature, it is possible to have different types of continuous charge distributions: spread out along a *line*, where $\mathrm{d}q = \lambda\mathrm{d}l'$ and $\lambda$ is the charge *per unit* length; over a *surface*, where $\mathrm{d}q = \sigma\mathrm{d}a'$ and $\sigma$ is the charge *per unit* area; fill a *volume*, where $\mathrm{d}q = \rho\mathrm{d}\tau'$ and $\rho$ is the charge *per unit* volume.

Woefully, the resolution of these integrals, depending on the system, can be formidable. Therefore, it is important to have *"tools"* to avoid these integrals. The two more relevant for electrostatic problems are the divergence and the curl of $\vec{E}$.

## 3.3 Divergence and Curl of Electrostatic fields

Let $q$ be a point charge within a closed surface $S$, $\hat{n}$ the normal and $\mathrm{d}a$ the element of a surface area, as it is depicted in Figure 3.1. Towards this scenario, the natural question that emerges is: "What would be the flux of $\vec{E}$ out of this arbitrary closed surface S?"

The flux of the electric field, $\phi$, can be defined as the electric field passing across a given area multiplied by the area of $S$ perpendicular to $\vec{E}$ [75],

$$\mathrm{d}\phi = \vec{E}\cdot\mathrm{d}a\hat{n} = \frac{q}{4\pi\epsilon_0} \tag{3.7}$$

Taking the integral of the normal component of $\vec{E}$ around the entire surface,

$$\oint_S \vec{E} \cdot \mathrm{d}a\hat{n} = \begin{cases} q/\epsilon_0, & \text{if } q \text{ is inside S} \\ 0, & \text{if } q \text{ is outside S} \end{cases} \tag{3.8}$$

This result depicts the integral form of the Gauss Law for a single point charge. If instead of a point charge there is a group of charges scattered inside $S$, eq (3.8) becomes,

$$\oint_S \vec{E} \cdot \mathrm{d}a\hat{n} = \sum_{i=1}^{n} \Big( \oint_S \vec{E}_i \cdot \mathrm{d}a\hat{n} \Big) = \sum_{i=1}^{n} \Big( \frac{q_i}{\epsilon_0} \Big) = \frac{Q_{inside}}{\epsilon_0} \tag{3.9}$$

From the integral form of eq (3.9), it is possible to derive the differential form by employing the *divergence theorem* – the surface integral of a well behaved vector field over a closed surface, is equivalent to the volume integral of the divergence atop the region inside the surface [75],

$$\int_V (\boldsymbol{\nabla} \cdot \vec{E}) \mathrm{d}\tau = \int_V \Big( \frac{\rho}{\epsilon_0} \Big) \mathrm{d}\tau \tag{3.10}$$

$$\boldsymbol{\nabla} \cdot \vec{E} = \frac{\rho}{\epsilon_0} \tag{3.11}$$

The result presented in eq (3.11) is known as the Gauss-Ostrogradsky theorem. Since the study of the divergence of $\vec{E}$ is completed, all we need is the *vorticity* of $\vec{E}$. The technique to study the latest property is through the curl of $\vec{E}$. The curl is related to the way that the vectors that compose the field rotate from one point to another.

If one recalls the radial property of $\vec{E}$ previously mentioned, it becomes obvious that the curl of $\vec{E}$ should be zero. To have a more rigorous definition, let us consider the line integral of the scalar product of $\vec{E}$ with an infinitesimal line segment $\mathrm{d}\vec{l}$ from one point $a$ to $b$[74],

$$\int_a^b \vec{E} \cdot \mathrm{d}\vec{l}$$

considering the *Stoke's theorem* – the path integral of a vector field over a closed contour is equal to the flux of its curl along the enclosed surface [75] , it is possible to rewrite eq (3.12),

$$\oint_C \vec{E} \cdot \mathrm{d}\vec{l} = \int_S (\boldsymbol{\nabla} \times \vec{E}) \mathrm{d}\vec{l} = 0 \tag{3.12}$$

$$\boldsymbol{\nabla} \times \vec{E} = 0 \tag{3.13}$$

## 3.4 Electric potential

Due to eq (3.13), and because there is no dependence in the path when computing the line integral, it is possible to write

$$V(\vec{r}) = \int_O^r \vec{E} \cdot \mathrm{d}\vec{l} \tag{3.14}$$

$V$ is the *electric potential*, and $O$ is a reference point.The most convenient form of eq (3.14) is when calculating $V$ between two points $a$ and $b$,

$$V(b) - V(a) = -\int_a^b \vec{E} \cdot \mathrm{d}\vec{l} \tag{3.15}$$

Resorting to the fundamental gradient theorem [74] it is possible to rearrange eq (3.15) in such a way that,

$$V(b) - V(a) = \int_a^b (\nabla V) \cdot \mathrm{d}\vec{l} \tag{3.16}$$

which leads to the following result,

$$\int_a^b (\nabla V) \cdot \mathrm{d}\vec{l} = -\int_a^b \vec{E} \cdot \mathrm{d}\vec{l} \Leftrightarrow \vec{E} = -\nabla V \tag{3.17}$$

Recalling the electric field of a continuous charge distribution, it is now possible to define its electric potential,

$$V(\vec{r}) = \frac{1}{4\pi\epsilon_0} \int \frac{\rho}{r'} \mathrm{d}\tau' \tag{3.18}$$

where $r'$ is the position of the charge distribution, $r = \infty$ and $V = 0$. A very important detail of the electric potential is that it also respects the superposition principle.

## 3.5 Multipole Expansion

Ongoing with the latest general expression of the electric potential of a continuous charge distribution, it is possible to define $r$ in such a way that,

$$r^2 = R^2 + r'^2 - 2Rr' \cos\theta \tag{3.19}$$

For this purpose it is important to clarify that $\vec{r}^{'}$ is the position of the charges and $\vec{r}$ is the distance from the charges to a point assigned by $\vec{R}$. For points in space that are away from the distribution

and for which $R \gg r'$[74], it is possible to expand eq(3.19) in a Taylor Series,

$$\frac{1}{r} = \frac{1}{R}\Bigg[1 + \Big(\frac{r'}{R}\Big)\cos\theta + \Big(\frac{r'}{R}\Big)^2\Big(\frac{3\cos^2\theta - 1}{2}\Big) + \Big(\frac{r'}{R}\Big)^3\Big(\frac{5\cos^3\theta - 3\cos\theta}{2}\Big) + \cdots\Bigg] \tag{3.20}$$

and in terms of the potential it becomes,

$$V(\vec{r}) = \frac{1}{4\pi\epsilon_0}\Big[\frac{1}{R}\int \rho(r')\mathrm{d}\tau' + \frac{1}{\mathrm{R}^2}\int \rho(\mathrm{r}')\mathrm{r}'\cos(\theta)\mathrm{d}\tau' + \frac{1}{R^3}\int (r')^2\rho(r')\Big(\frac{3\cos^2(\theta) - 1}{2}\Big)\mathrm{d}\tau' + \cdots\Big] \tag{3.21}$$

The result in eq (3.21) is the multipole expansion of the potential, where the first term is the potential of a *monopole*, the second one (and the most important for this work) is the potential of a *dipole*, and the third the potential of the *quadropole*.

## 3.6 Dipole moment

From now on, it is important to precisely distinguish two types of dipoles: the ideal and the physical.

The *physical electric dipole* is composed of two opposite charges ($q^+$ and $q^-$) separated by a distance $d$, whereas the *ideal dipole* exists for the artificial limit where $d \to 0$ and $q \to \infty$[74]. From eq (3.21) it is possible to extract the potential of a physical dipole,

$$V(\vec{r}) = \frac{1}{4\pi\epsilon_0}\frac{1}{R^2}\int \rho(r')r'\cos(\theta)\mathrm{d}\tau' \tag{3.22}$$

but since $\theta$ is the angle between $r'$ and $R$ then,

$$r'\cos(\theta) = \vec{r}' \cdot \hat{r} \tag{3.23}$$

which allows the simplification of the integral expression to,

$$V_{\mathrm{dipole}}(\vec{r}) = \frac{1}{4\pi\epsilon_0}\frac{1}{R^2}\int \rho(r')\vec{r}' \cdot \hat{r}\mathrm{d}\tau' \tag{3.24}$$

The integral term in eq (3.24) is the so called *dipole moment, $\vec{p}$,*

$$\vec{p} = \int \rho(r')\vec{r}' \cdot \mathrm{d}\tau' \tag{3.25}$$

As it was for the electric field, the dipole moment is dependent on the size, shape and density of the charge distribution[75].

## 3.7 Induced dipoles

Now that the dipole moment is rigorously defined, the goal is to understand the response of a dielectric (atom or molecule) to an external electric field.

Firstly, a dielectric can be defined as an electric insulator that can become polarized with the external application of an electric field[74]. This leads, and partially answers, to the following question: "What happens to a neutral atom (dielectric) when an electric field is applied? "

As an initial guess, since the atom is electrically neutral, one may think that no effect would emerge from this interaction, which is not true. The correct answer is dependent on one factor the *intensity* of $\vec{E}$. If $\vec{E}$ has a *weak* intensity, an equilibrium is established leaving the atom *polarized* [76], that is, the nucleus is pulled in the direction of the field and the electrons in the opposite direction. This small distortion of the charges constitutes an *induced* dipole moment.

By contrast, if $\vec{E}$ is an *intense* field, the atom can become a conductor (ionized) since the applied field is strong enough to excite the more energetic electrons. For the purpose of this thesis, only the first case will be further developed.

## 3.8 Polarizability

For the weak electric field scenario, the result of the interaction is the induction of a small dipole moment [76] , $\vec{p}_{\text{ind}}$, that points in the same direction as $\vec{E}$ and is proportional to the intensity of $\vec{E}$,

$$\vec{p}_{\text{ind}} = \alpha \vec{E} \tag{3.26}$$

where the constant of proportionality is the atomic *polarizability*. Before going deeper within the concept of polarizability, it is important to point out that eq (3.27) is defined for a field that is aligned with the molecule axis. For instance, if the field is applied at some angle, in respect to the molecule's axis, it is important to break down $\vec{E}$ in its parallel and perpendicular components and then multiply by the respective polarizability [74],

$$\vec{p}_{\text{ind}} = \alpha_{\parallel} \vec{E}_{\parallel} + \alpha_{\perp} \vec{E}_{\perp} \tag{3.27}$$

For this particular case where the field is not aligned with the axis, the induced dipole moment is not in the same direction as $\vec{E}$. Also, there is a certain subtlety in eq(3.27), which is the assumption of an *isotropic* medium, uniform in all spatial orientations. For the case of an *anisotropic* medium, the

polarizability is described as a rank tensor of second order[74],

$$\begin{cases} \vec{p}_{\text{ind,xx}} = \alpha_{xx}\vec{E}_{xx} + \alpha_{xy}\vec{E}_{xy} + \alpha_{xz}\vec{E}_{xz} \\ \vec{p}_{\text{ind,yy}} = \alpha_{yx}\vec{E}_{yx} + \alpha_{yy}\vec{E}_{yy} + \alpha_{yz}\vec{E}_{yz} \\ \vec{p}_{\text{ind,zz}} = \alpha_{zx}\vec{E}_{zx} + \alpha_{zy}\vec{E}_{zy} + \alpha_{zz}\vec{E}_{zz} \end{cases} \tag{3.28}$$

Due to *reciprocity relationships* the latest system simplifies from nine different components to only six. In the matrix form, and considering the latest assumption, one obtains the polarizability matrix, $\alpha$,

$$\begin{bmatrix} \alpha_{xx} & \alpha_{xy} & \alpha_{xz} \\ \alpha_{xy} & \alpha_{yy} & \alpha_{yz} \\ \alpha_{xz} & \alpha_{yz} & \alpha_{zz} \end{bmatrix} \tag{3.29}$$

The observable quantity is the *mean* polarizability which can be obtained by the trace of the matrix $\alpha$ [77],

$$\overline{\alpha} = \frac{1}{3}\Big(\alpha_{xx} + \alpha_{yy} + \alpha_{zz}\Big) \tag{3.30}$$

## 3.9 Calculation of the molecular polarizability

With the concept of polarizability derived, it is important to understand how is this molecular property computed.

Within the many variants of computational methods for electronic structure calculations, usually the main goal is to obtain the energy and physical properties of a molecular system.

When dealing with electrical properties one needs to have in mind that they are a measure of the response of the electron density in the presence of an electric field. In order to account for this external stimulus, a power series expansion of the energy can be done considering a small external electric field $\vec{\chi}$ [78],

$$\begin{aligned} E(\vec{\chi}) = E(0) + \sum_i \left(\frac{\partial E(\vec{\chi})}{\partial \chi_i}\right)_0 \chi_i + \frac{1}{2}\sum_{i,j}\left(\frac{\partial^2 E(\vec{\chi})}{\partial\chi_i\partial\chi_j}\right)_0 \chi_i\chi_j + \\ \frac{1}{6}\sum_{i,j,k}\left(\frac{\partial^3 E(\vec{\chi})}{\partial\chi_i\partial\chi_j\partial\chi_k}\right)_0 \chi_i\chi_j\chi_k + \cdots \end{aligned} \tag{3.31}$$

The first term in eq (3.31) is the total unperturbed energy of the system and the second, third and fourth terms are the energy due to the static dipole moment, polarizability and first hyperpolarizabily respectively [78].The terms within parenthesis in eq (3.31) correspond to the components of the respective properties.

A very important aspect of this derivation is that it does not consider a time dependency, and as

a consequence the properties are calculated statically [78].

To complete the study of the molecular polarizability, only a final step remains, which is the understanding of how can this property be useful to approach a problem of selectivity in photochemical reactions.

## 3.10 Polarizability as a marker for molecular selectivity in photochemical reactions

In 1987, through his experimental and theoretical research, Pearson noticed that *there seems to be a rule of nature that molecules arrange themselves to be as hard as possible*[79], which would later be stated as the maximum hardness principle (MHP). Hardness is a property that can be defined as the second derivative of the electronic energy with respect to the number of electrons, $N$, considering a constant external potential $v(\vec{r})$ [77],

$$\eta = \frac{1}{2}\left(\frac{\partial^2 E}{\partial N^2}\right)_{v(\vec{r})} \tag{3.32}$$

With that said, two quite natural questions arise: " What could possibly be the link between hardness and polarizability? And how can this be useful ?"

Some years ago, Fuentealba and Reyes[80] and Ghanty and Ghosh[81] showed that as the hardness values decreased there was an increase in the molecular reactivity [77], and also found that polarizability is inversely proportional to the third power of hardness which makes possible the link between polarizability with molecular stability as the latter property is deeply connected with reactivity.

The relevance of these results for the purpose of this thesis lies in the connection between polarizability and the reactivity of a molecular system. As aforementioned, the aim is to clarify which photochemical path 3CTZ and CTZ mechanisms will take, and what products will be formed. The idea is then to address the stability of each product through the study of their polarizability and bridge it with its own reactivity which ultimately will allow to conclude which product is more probable to be obtained.

# Chapter 4

# Methodology: Electronic structure calculations

This chapter is focused on the methodology that was used through out this thesis. The goal is to present the rate constant derivation, and its computational details, and review the fundamental concepts behind density functional theory (DFT) and time dependent density functional theory (TD-DFT).

In the first part, a theoretical derivation of the rate constants is carried out in two different frameworks: Fourier simplified transformed formula (FSTF) and the Path integral approach (PIA).

The goal of the second part is to present the basic fundamental concepts of electronic structure theory, such as the Schrödinger equation, molecular Hamiltonian, Born-Oppenheimer Approximation and Variational principle, to build the necessary foundations for further DFT and TD-DFT formalisms. Following this line, next the Hohenberg-Kohn theorem, Kohn-Sham equations and the exchange and correlation energy are introduced.

This section finishes with the presentation of DFT and TD-DFT formalisms and their application for the computation of molecular properties. In the end, some relevant computational details are also discussed such as the basis set and the iterative behaviour of DFT and TD-DFT.

## 4.1 Rate constant derivation

In order to properly describe a photophysical process one still needs, the computation of the rate constant. In this thesis two different methods were considered for the latter task: Fourier simplified transformed formula (FSTF)[71] and the Path integral approach (PIA)[82, 83].

### 4.1.1 FSTF method

Let's start with the IC photophysical process. As previously mentioned, this process happens because of the overlap of vibrational and electronic states [70, 71]. Hence, to derive IC's rate constant ($k_{\mathrm{IC}}$), the perturbation operator in eq (2.3) must be substituted for the first-order vibronic coupling operator[71]. With this, one obtains a general expression for the rate constant $k_{\mathrm{IC},m}$ of each $m^{th}$ vibrational mode [70],

$$k_{\mathrm{IC}_m} = \frac{2\pi}{\hbar} R_m \sum_{v_k, v_l} \frac{\exp(-\beta E_{kv_k})}{Z_{v_k}} P_m \delta(E_{kl} + E_{l_{vl}} - E_{k_{vk}}) \tag{4.1}$$

$$R_m = \frac{\hbar^2 V_m^2}{\Delta {E_{FC}}^2} \tag{4.2}$$

$$V_m = \left\langle \phi_k \left| \frac{\partial \hat{U}_{en}}{\partial Q_m} \right| \phi_l \right\rangle \tag{4.3}$$

$$P_m = -\hbar^2 \left\langle \Theta_l \left| \frac{\partial \Theta_k}{\partial Q_m} \right\rangle \right\langle \Theta_k \left| \frac{\partial \Theta_l}{\partial Q_m} \right\rangle \tag{4.4}$$

where $m$ represents the $m^{th}$ vibrational mode, $R_m$ has units of energy, $V_m$ is the magnitude of the vibronic coupling amid singlet states $S_k$ and $S_l$ ($k \neq l$ and $k, l \geq 1$), $Q_m$ are the normal coordinates of the vibrational mode, $\hat{U}_{en}$ is the electron-nuclear potential of the molecular system, $\Delta E_{\mathrm{FC}}$ is the vertical excitation energy difference between $S_0 - S_k$ and $S_0 - S_l$ (FC stands for Franck-Condon), $\Theta_k$, $\Theta_l$, $\phi_k$ and $\phi_l$ represent the vibrational and electronic wave functions of the states $S_k$ and $S_l$, respectively. $E_{kl}$ denotes the adiabatic energy difference between singlet states $S_k$ and $S_l$, which is computed between the ground and excited state in the equilibrium geometry, and $E_{k_{vk}}$ and $E_{l_{vl}}$ are their respective vibrational energies. The term $\beta^{-1} = k_B T$ with $k_{\mathrm{B}}$ being the Boltzmann constant, $T$ the temperature and $Z_{v_k}$ the vibrational partition function of the $S_k$ electronic state. From eq (4.1), one can calculate the IC constant of each individual vibrational mode but, in order to obtain $k_{\mathrm{IC}}$, one must do a sum over all $k_{\mathrm{IC_m}}$

$$k_{\mathrm{IC}} = \sum_m k_{\mathrm{IC_m}} \tag{4.5}$$

Usually, the computation of rate constants is done within the frequency domain and involves taking into account all the initial states that are thermally available[83]. Specially for a low frequency scenario, this can become a quite difficult task due to the large number of initial states that might be available [83].

To overcome this problem, one can work with the general expression of the Dirac function in its Fourier transformed formula and switch to the time domain [84, 85],

$$\delta(\omega) = \frac{1}{2\pi} \int_{-\infty}^{+\infty} \exp(i\omega t) \mathrm{dt} \tag{4.6}$$

The further application of eq (4.6) in the rate constant derivation/computation is what gives this

method its name. Before proceeding with the derivation, it is important to point out that in eq (4.6) the *Duschinsky rotation effect* (DRE) is not considered in order to avoid complex multidimensional integrals [86–88]. The latter is a linear transformation approximation that relates two sets of normal coordinates, for example electronic ground state and an excited state, through a displacement vector[89].

Nevertheless research has shown that DRE is very important for various molecular systems, particularly for those that have harsh changes in their geometry [86, 90].

Incorporating eq (4.6) in eq (4.1) one gets the time domain expression for $k_{\mathrm{IC_m}}$ calculation [70, 71],

$$k_{\mathrm{IC}_m} = \frac{1}{\hbar^2} R_m \int_{-\infty}^{+\infty} \exp(i\omega_{kl}t) Z_{vk}^{-1} \rho_{\mathrm{IC_m}}(t,T)\mathrm{dt} \tag{4.7}$$

with $\omega_{kl} = E_{kl}/\hbar$ and $\rho_{\mathrm{IC_m}}(t,T)$ being the thermal vibration correlation function for the $m^{th}$ vibrational mode. Although the derivation so far was done for singlet states, the IC process can also happen between triplet states. To account for such behaviour, $S_k$, $S_l$ and $\Delta E_{\mathrm{FC}}$ ( as $S_0 - S_k$ and $S_0 - S_l$) in Eq. (4.1) must be replaced for $T_k$, $T_l$ and $\Delta E_{\mathrm{FC}}$ (as $S_0 - T_k$ and $S_0 - T_l$) with ($k \neq l$ and $k, l \geq 1$), respectively.

Regarding ISC's rate constant($k_{\mathrm{ISC}}$), because this photophysical process is due to spin-orbit coupling [73], the perturbation operator in eq (2.3) should be replaced with the first order spin-coupling operator ($\hat{H}_{\mathrm{SOC}}$) [73],

$$\hat{H}_{\mathrm{SOC}} = \frac{\alpha^2}{2} \sum_{i,j} Z_{\mathrm{eff}}(\vec{r_{ij}})^{-3} (\vec{r_{ij}} \times \vec{P_i}) \cdot \vec{s_i} \tag{4.8}$$

where $\alpha$ is the fine structure constant, $Z_{\mathrm{eff}}$ is the effective nuclear charge, $r_{ij}$ is the distance between electron $i$ and nuclei $j$, $\vec{P_i}$ is the momentum vector of electron $i$ and $\vec{s_i}$ is the spin-angular momentum vector of electron $i$. With the latter operator substitution one has,

$$k_{\mathrm{ISC},M_s} = \frac{2\pi}{\hbar} \langle \phi_k | \hat{H}_{\mathrm{SOC}} | \phi_l^{M_s} \rangle^2 \sum_{v_k, v_l} \frac{\exp(-\beta E_{kv_k})}{Z_{v_k}} \times \langle \Theta_k | \Theta_l^{M_s} \rangle^2 \delta(E_{kl} + E_{l_{vl}} - E_{k_{vk}}) \tag{4.9}$$

where $\phi_k$ and $\phi_l^{\mathrm{M_s}}$ denote the electronic wave functions, of $S_k$ and $T_l^{\mathrm{M_s}}$ states, and $\Theta_l$ and $\Theta_k$ are the vibronic wave functions of the $T_l^{\mathrm{Ms}}$ and $S_k$ electronic states. The $M_s$ in eq (4.9) stands for the three degenerated spin multiplicities of the triplet state $T_l^{\mathrm{M_s}}$($M_s$=0,±1).

The strength of the spin-orbit coupling between $\phi_k$ and $\phi_l^{\mathrm{Ms}}$, considering the triplet in thermal equilibrium, is given by[70, 71],

$$|\mathrm{SOC}| = \sqrt{\left( \sum_{M_s=0,\pm1} |\langle \phi_k | \hat{H}_{\mathrm{SOC}} | \phi_l^{M_s} \rangle|^2 \right)} \tag{4.10}$$

Rewriting eq (4.9) in terms of eq (4.10) one has,

$$k_{\mathrm{ISC},M_s} = \frac{2\pi}{\hbar}|\mathrm{SOC}|^2 \sum_{v_k,v_l} \frac{\exp(-\beta E_{kv_k})}{Z_{v_k}} \langle \Theta_k | \Theta_l^{M_s} \rangle^2 \delta(E_{kl} + E_{l_{vl}} - E_{k_{vk}}) \tag{4.11}$$

Adapting eq (4.11) within the Fourier transformed framework,

$$k_{\mathrm{ISC},M_s} = \frac{1}{\hbar^2}|\mathrm{SOC}|^2 \int_{-\infty}^{+\infty} \exp(i\omega_{kl}t)dt \tag{4.12}$$

To obtain $k_{ISC}$ all the triplet spin multiplicities need to be accounted for. Hence, $k_{ISC}$ is defined as a sum over all $k_{\mathrm{ISC},M_s}$,

$$k_{\mathrm{ISC}} = k_{\mathrm{ISC}}T^{(1)} + k_{\mathrm{ISC}}T^{(0)} + k_{\mathrm{ISC}}T^{(-1)} \tag{4.13}$$

The computation of rate constants for radiative deactivation mechanisms, such as fluorescence ($k_{\mathrm{F}}$) and phosphorescence ($k_{\mathrm{P}}$), can be accomplished through the integration of the differential spontaneous photon emission rate $\sigma(\omega)_{\mathrm{em}}$ [70],

$$k = \int_0^{+\infty} \sigma_{em}(\omega)\mathrm{d}\omega \tag{4.14}$$

with $\sigma(\omega)_{\mathrm{em}}$ defined as[85, 91, 92],

$$\sigma_{em}(\omega) = \frac{4\omega^3}{3c^3} \sum_{\nu_f,\nu_i} Z_{\nu k}(T) |\langle \Theta_{f\nu f} | \vec{\mu}_{fi} | \Theta_{i\nu i} \rangle|^2 \delta(E_{kl} + E_{l_{vl}} - E_{k_{vk}} - \hbar\omega) \tag{4.15}$$

in eq (4.15) the term $Z_{\nu_k}^{-1}\rho_{em,kl}^{\mathrm{HT}}(t,T)$ is equal to the unity because the energetic difference between $S_1 - S_0$ is large when compared to $k_{\mathrm{B}}T$ (see chapter II, subsection 2.1.2). The same reasoning can be done for phosphorescence. Combining eq (4.14) with eq (4.15), and switching to the time domain, one has

$$\sigma_{em}(\omega) = \frac{2\omega^3}{3\pi\hbar c^3}|\vec{\mu}_{fi}|^2 \int_{-\infty}^{+\infty} \exp\Big(-i(\omega - \omega_{kl})t\Big)dt \tag{4.16}$$

For both fluorescence and phosphorescence the transition dipole moment in eq (4.15) can be written as $\vec{\mu}_{F,01}$ and $\vec{\mu}_{P,01}$, respectively, where zero stands for the ground state (final state) and one for the $S_1$ or $T_1$ (initial state) depending if it is $\vec{\mu}_F$ or $\vec{\mu}_P$. Gathering all, it is possible to write the following expression for ($k_{\mathrm{F}}$) and phosphorescence ($k_{\mathrm{P}}$) computation,

$$k_F = \frac{2\omega^3}{3\pi\hbar c^3}|\vec{\mu}_{F,01}|^2 \int_0^{+\infty} \left\{ \int_{-\infty}^{+\infty} \exp\Big(-i(\omega - \omega_{kl})t\Big)\mathrm{dt} \right\} \mathrm{d}\omega \tag{4.17}$$

$$k_P = \frac{2\omega^3}{3\pi\hbar c^3}|\vec{\mu}_{P,01}|^2 \int_0^{+\infty} \left\{ \int_{-\infty}^{+\infty} \exp\Big(-i(\omega - \omega_{kl})t\Big)\mathrm{dt} \right\} \mathrm{d}\omega \tag{4.18}$$

### 4.1.2 Simplified formulation based on FSTF

Based on the latter derivation, Katsuyuki *et al.* deduced a set of more simplified expressions for rate constant calculation[71]. In order to assure the convergence of the integrals in eqs (4.7, 4.12, 4.17, 4.18) the authors multiplied them by a distribution function ($D(E)$) of the Lorentzian ($L(E)$) or Gaussian ($G(E)$) type[71],

$$D(E_{kl} \pm \hbar\omega_m) = \frac{1}{\pi} \frac{\gamma}{(E_{kl} \pm \hbar\omega_m)^2 + (\gamma^2)} \tag{4.19}$$

$$L(E_{kl}) = \exp(-\gamma|t|) = \frac{1}{\pi} \frac{\gamma}{E_{kl}^2 + \gamma^2} \tag{4.20}$$

$$G(E_{kl}) = \exp\left(-\frac{\sigma^2 t^2}{2}\right) = \frac{1}{\sqrt{2\pi}} \frac{1}{\sigma} \exp\left[\left(-\frac{E_{kl}^2}{2\sigma^2}\right)\right] \tag{4.21}$$

$$\gamma = \frac{\text{fwhm}}{2} \tag{4.22}$$

$$\sigma = \frac{\text{fwhm}}{2\sqrt{2\ln 2}} \tag{4.23}$$

where fwhm is the full width at half maximum which can be directly calculated from the absorption/emission spectrum. These distribution functions also take into account the dephasing effects between the molecule and the solvent[93]. For a homogeneous dephasing, the Lorentzian distribution should be used and for inhomogeneous dephasing the Gaussian distribution[70].

Regarding $k_{\text{IC}}$ calculation, the simplified formulation is defined as follows[71],

$$k_{\text{IC},m} = \frac{2\pi\hbar^3}{\Delta E_{\text{FC}}^2} V_m^2 A_m \tag{4.24}$$

$$\begin{aligned} A_m = \sinh\left(\frac{1}{2}\beta\hbar\omega_m\right) \sum_{v_m=0}^{M} \exp\left\{\left[-\left(\frac{1}{2} + v_m\right)\beta\hbar\omega_m\right]\right\} \times \\ \frac{1}{S}\{v_m D(E_{kl} + \hbar\omega_m) + (v_m + 1) D(E_{kl} - \hbar\omega_m)\} \end{aligned} \tag{4.25}$$

$$S = \frac{1}{4\pi\epsilon_0} \frac{e^2}{a_{\text{B}} hc} \tag{4.26}$$

where $\epsilon_0$ is the vacuum permittivity, $e$ is the electron charge, $a_{\text{B}}$ is the Bohr radius and $M$ denotes the number of vibrational modes $M = 3N - 6$ for non linear molecules and $M = 3N - 5$ for linear molecules. The vibronic coupling term $V_m$ is with respect to the normal coordinates $\left(\frac{\partial V}{\partial Q}\right)$, but when one does the calculation the output is the vibronic coupling in Cartesian coordinates $\left(\frac{\partial V}{\partial x}\right)$. Hence, the following transformation is needed,

$$\left\langle \left| \frac{\partial V}{\partial x} \right| \right\rangle = \frac{\partial V}{\partial Q} \frac{\partial Q}{\partial x} \tag{4.27}$$

$$\left\langle \left| \frac{\partial V}{\partial Q} \frac{\partial Q}{\partial x} \right| \right\rangle = \left\langle \left| \frac{\partial V}{\partial x} \right| \right\rangle \tag{4.28}$$

$$\left\langle \left| \frac{\partial V}{\partial Q} \right| \right\rangle = \left\langle \left| \left( \frac{\partial Q}{\partial x} \right)^{-1} \right| \right\rangle \left\langle \left| \frac{\partial V}{\partial x} \right| \right\rangle \tag{4.29}$$

with the normal coordinate $Q$ defined as[94],

$$Q = \sqrt{\frac{\omega_\alpha}{\hbar}} \sum_{k=1}^{3N} L_{k\alpha} \sqrt{M_k} \delta x_k \tag{4.30}$$

where $N$ is the number of atoms of the molecular system. The term $\frac{\partial Q}{\partial x}$ can be obtained through the differentiation of eq (4.30) in respect of $x$,

$$\frac{\partial Q}{\partial x} = \sqrt{\frac{\omega_\alpha}{\hbar}} \sum_{k=1}^{3N} L_{k\alpha} \sqrt{M_k} \tag{4.31}$$

which leads to,

$$V_m = \left\langle \left| \frac{\partial V}{\partial Q} \right| \right\rangle = \left( \sqrt{\frac{\omega_\alpha}{\hbar}} \sum_{k=1}^{3N} L_{k\alpha} \sqrt{M_k} \right)^{-1} \times \frac{\partial V}{\partial x} \tag{4.32}$$

For $k_{\mathrm{ISC}}$, the authors expanded eq (4.12) by including the dephasing effects[71],

$$k_{\mathrm{ISC},M_s} = \frac{2\pi}{\hbar} |\mathrm{SOC}|^2 L(E_{kl}) \tag{4.33}$$

$$k_{\mathrm{ISC},M_s} = \frac{2\pi}{\hbar} |\mathrm{SOC}|^2 G(E_{kl}) \tag{4.34}$$

Regarding $k_{\mathrm{F}}$ and $k_{\mathrm{P}}$, the simplified formulation of eqs (4.17) and (4.18) is given by[71],

$$k_{\mathrm{F}} = \frac{4(\hbar\omega_F)^3}{3\hbar^4 c^3} |\vec{\mu}_{F,01}|^2 \tag{4.35}$$

$$k_{\mathrm{P}} = \frac{4(\hbar\omega_{\mathrm{F}})^3}{3\hbar^4 c^3} |\vec{\mu}_{P,01}|^2 \tag{4.36}$$

where $\omega_F$ and $\omega_P$ are the adiabatic energy difference between $S_0 - S_1$ and $S_0 - T_1$ respectively. Eqs (4.35) and (4.36) could also be expanded with the dephasing effects but, the integral of a Gaussian, or Lorentzian, distribution is equal to one.

### 4.1.3 PIA method

Based on the work of Lin [95], Shuai [70] and Barone [84], Souza *et al.* [83] developed a way to calculate radiative rate constants ($k_{\mathrm{F}}$ and $k_{\mathrm{P}}$) with the path integral approach. Regarding non-radiative constants ($k_{\mathrm{IC}}$ and $k_{\mathrm{ISC}}$), their calculation is also PIA based but a theoretical derivation has not yet been published.

Likewise in the FSTF method, Souza *et al.* [83] also switched to the time domain, for the same

reason previously presented. Rewriting eq (2.4) in the latter framework one has [83],

$$k_F(\omega) = \frac{2\omega^3 n^2}{3\pi c^3 Z} \sum_{if} \exp\left(-\frac{\epsilon_i}{k_B T}\right) \langle \Theta_i | \vec{\mu} | \Theta_f \rangle \langle \Theta_f | \vec{\mu} | \Theta_i \rangle \int \exp\Big(i(E_i - E_f - \omega t)\Big) \mathrm{dt} \tag{4.37}$$

where $\epsilon_i$ is the total vibrational energy. Contrary to FSTS derivation, Souza *et al.* included DRE [96]. Further simplification can be done to eq (4.37) if one recognises $\epsilon_i$ as the eigenvalue of the vibrational Hamiltonian operator and the completeness relationship $\sum_f |\Theta_f\rangle \langle \Theta_f| = 1$ [97],

$$k_{\mathrm{F}}(\omega) = \frac{2\omega^3 n^2}{3\pi c^3 Z} \int \sum_{if} \langle \Theta_i | \vec{\mu} e^{(-i\hat{H}'\tau')} \vec{\mu} e^{(-i\hat{H}\tau)} | \Theta_i \rangle e^{(i(\Delta E - \omega)t)} \mathrm{dt} \tag{4.38}$$

$$k_{\mathrm{F}}(\omega) = \frac{2\omega^3 n^2}{3\pi c^3 Z} \int Tr\Big(\vec{\mu} e^{(-i\hat{H}\tau')} \vec{\mu} e^{(-i\hat{H}\tau)}\Big) e^{(i\Delta E t)} e^{(-i\omega t)} \mathrm{dt} \tag{4.39}$$

where $\tau' = t$, $\tau = -t - (i/k_{\mathrm{B}}T)$ and $\hat{H}'$ is the Hamiltonian of the final state. With the latter formulation, *Souza et al.*[83] were able to reduce their problem just to the computation of a Fourier transformed correlation function $\chi(t)$.

$$k_{\mathrm{F}}(\omega) = \frac{2\omega^3 n^2}{3\pi c^3 Z} \int \chi(t) e^{-i\omega t} \mathrm{dt} \tag{4.40}$$

$$k_{\mathrm{F}}(\omega) = 2\left(\frac{2\omega^3 n^2}{3\pi c^3 Z}\right) \mathrm{Re}\{e\} \int \chi(t) e^{-i\omega t} \mathrm{dt} \tag{4.41}$$

$$k_{\mathrm{F}}(\omega) = 2\left(\frac{2\omega^3 n^2}{3\pi c^3 Z}\right) \Delta t \, \mathrm{Re}\{e\} \mathcal{F}(\chi(t)) \tag{4.42}$$

Here the $\mathcal{F}(\chi(t))$ is the resolution of the correlation function in its Discrete Fourier Transform, which lessens the issue of calculating $\chi(t)$ [83]. Particularly for phosphorescence, due to its nature, the triplet state wave function must account for spin-orbit coupling effects[73]. To do so, one may use first order perturbation theory and write the following triplet wave function[82],

$$|\psi_{T1}^{\mathrm{SOC}}\rangle = |\psi_{T1}\rangle + \sum_n \frac{\langle \psi_{sn} | \hat{H}_{\mathrm{SOC}} | \psi_{T1} \rangle}{(E(T_1) - E(S_n))} |\psi_n\rangle \tag{4.43}$$

The derivation of $k_{\mathrm{P}}$ is similar to the formalism previously presented for $k_{\mathrm{F}}$.

## 4.2 DFT and TD-DFT

In this thesis all the electronic structure calculations were done at the DFT and TD-DFT level of theory. The following sections will present the fundamental concepts behind DFT and TD-DFT formalisms as well as some computational details.

### 4.2.1 Schrödinger's Equation

The dynamics of an isolated quantum physical system is given by the non-relativistic time dependent Schrödinger equation,

$$\hat{H}\left|\Psi(\vec{r},t)\right\rangle_j = i\hbar\frac{\partial}{\partial t}\left|\Psi(\vec{r},t)\right\rangle_j \tag{4.44}$$

where $t$ is the time, $\hat{H}$ is the Hamiltonian operator and $\left|\Psi(\vec{r},t)\right\rangle_j$ is the $j^{th}$ *eigenstate* of $\hat{H}$, more commonly, the anti-symmetric *wave function*.

Eq (4.44) foretells that wave functions can form stationary states[98] and that these can be obtained by an easier form of eq(2.1), also non-relativistic, which is the time-independent Schrödinger equation,

$$\hat{H}\left|\Psi(\vec{r})_j\right\rangle = E_j\left|\Psi(\vec{r})_j\right\rangle \tag{4.45}$$

where $\hat{H}$ and $\Psi(\vec{r})_j$ represent once again the Hamiltonian operator and its $j^{th}$ eigenstate , respectively. Associated with each one of these eigenstates is an *eigenvalue*, $E_J$[1], which is the energy of the system.

To solve the Schrödinger equation, one must write down the Hamiltonian. This operator is composed by the terms of the kinetic and potential energy of the particles that constitute the system. For a molecular system with $N$ electrons and $M$ atomic nuclei, ignoring both spin [99] and the presence of a magnetic field [100], $\hat{H}$ is defined as,

$$\begin{aligned}\hat{H}(\vec{r}_1,\dots\vec{r}_N,\vec{R}_1,\dots,\vec{R}_M) = \hat{T}_{ee}+\hat{T}_{NN}+\hat{V}_{eN}+\hat{V}_{ee}+\hat{V}_{NN} = \sum_{i=1}^{N}\frac{\hat{p}_i^2}{2m_e}+\sum_{j=1}^{M}\frac{\hat{P}_j^2}{2m_j}+\\ \frac{e^2}{4\pi\epsilon_0}\left(-\sum_{i,j=1}^{N,M}\frac{Z_j}{|\vec{r}_i-\vec{R}_j}|+\sum_{i,I=1;i<I}^{N}\frac{1}{|\vec{r}_i-\vec{r}_I}|+\sum_{J,j=1;j<J}^{M}\frac{Z_jZ_J}{|\vec{R}_j-\vec{R}_J|}\right)\end{aligned} \tag{4.46}$$

where $\vec{r_i}$ and $\vec{R_j}$ are the coordinates of the electrons and atomic nuclei, respectively, $\vec{p_i}$ and $\vec{P_j}$ their linear momentum operators, $Z_j$ is the nuclear charge, $m_e$ is the mass of the electron and $m_j$ the mass of the atomic nuclei. The first two sums in eq (4.46) correspond to the kinetic component of $\hat{H}$, having into account the movement of both electrons and the atomic nuclei. The following terms correspond to the potential component of $\hat{H}$ which considers the electron-atomic nuclei, electron-electron and atomic nuclei-atomic nuclei interactions respectively.

### 4.2.2 Born-Oppenheimer Approximation

Due to the huge difference between the electron and atomic nuclear masses[100] (even the lightest of all atomic nuclei, the proton $H^1$, is 1836 times heavier than the electron[99]), the nuclear movement is much slower than the electronic- central idea of the *Born-Oppenheimer approximation*. As a consequence, the kinetic nuclear term $\hat{T}_{NN}$ is set to zero and the total wave function in eq (4.45), that

[1]Since $\hat{H}$ is hermitic these eigenvalues are real numbers.

initially was a function of two sets of coordinates (both electronic and nuclear), can now be rewritten with these two sets of degrees of freedom decoupled,

$$\hat{H}(r,R)\,|\Psi_j(r,R)\rangle = E_j(R)\,|\Psi_j(r,R)\rangle \tag{4.47}$$

Very so often eq (4.47) is referred as the electronic Schrödinger equation.

Owing to the parametric dependency of $\hat{H}$ with the nuclear coordinates [99], the treatment of the nuclear positions, $R_j$, is done as if the latter are just a particular set of numbers and for each set eq (4.47) is resolved. Simply put, the static electronic Schrödinger equation is resolved for one specific nuclear configuration at a time. Regarding the nuclear dynamics, the most common way to deal with it is classically by resolving the correspondent Hamilton equations.

Eq (4.45) only has analytical solution for a few specific systems, *e.g* harmonic oscillator, hydrogen atom and the particle in the box, therefore, to deal with a general molecular system one must work with approximated solutions.

### 4.2.3 Variational Principle

One way to compute approximated wave-functions, and energies, is with the variational principle. The latter states that any approximated wave function ($\varphi$) has an energy value equal or above the exact energy ($E_0$)[101].

Because $\hat{H}$ is hermitic, the solutions from eq (4.45) constitute a complete basis which allows the expansion of $\varphi$ in terms of $\Psi$,

$$\varphi = \sum_{i=0}^{\infty} a_i \Psi_i \tag{4.48}$$

with the energy of $\varphi$ defined as,

$$E(\varphi) = \frac{\langle\varphi|\hat{H}|\varphi\rangle}{\langle\varphi|\varphi\rangle} \tag{4.49}$$

Combining eq (4.48) and eq (4.49) one has,

$$E(\varphi) = \frac{\sum_{i=0}^{\infty}\sum_{j=0}^{\infty} a_i a_j \langle\Psi_i|\hat{H}|\Psi_j\rangle}{\sum_{i=0}^{\infty}\sum_{j=0}^{\infty} a_i a_j \langle\Psi_i|\Psi_j\rangle} \tag{4.50}$$

If the trial wave functions $\varphi$ are normalized[2] and orthonormal[3] [101],

$$E(\varphi) = \frac{\sum_{i=0}^{\infty} a_i^2 E_i}{\sum_{i=0}^{\infty} a_i^2} \tag{4.51}$$

$$E(\varphi) - E_0 = \frac{\sum_{i=0}^{\infty} a_i^2 E_i}{\sum_{i=0}^{\infty} a_i^2} - E_0 = \frac{\sum_{i=0}^{\infty} a_i^2 (E_i - E_0)}{\sum_{i=0}^{\infty} a_i^2} \tag{4.52}$$

[2] A normalized wave-function has the following property $\int_{-\infty}^{\infty} \Psi(x)^* \Psi(x) dx = 1$

[3] $\langle\varphi_i|\varphi_j\rangle = \delta_{ij}$ with $\delta_{ij} = 1$ if $i = j$ and $\delta_{ij} = 0$ if $i \neq j$

Because $a_i^2$ coefficients are always positive, or zero, and $E(\varphi) - E_0$ is greater than zero, this proves that any trial wave function will always possess a higher energy than the exact ground state wave function. The computationally demanding part of the variational method is the task of finding the set of coefficients $a_i$ that minimize the energy of the trial wave-function. This can be accomplished with,

$$\frac{\partial E_\varphi(a_i)}{\partial a_i} = 0 \tag{4.53}$$

### 4.2.4 Electron density

The electron density ($\rho$) is defined as the square modulus of the wave-function[97, 101, 102],

$$\rho(\vec{r}) = |\Psi(\vec{r}, t)|^2 \tag{4.54}$$

The integration of $\rho(\vec{r})$ in space gives the probability of finding a particle, at a time $t$, in a specific region[97][4],

$$P = \int\int\int |\Psi(\vec{r}, t)|^2 \mathrm{d}x\mathrm{d}y\mathrm{d}z \tag{4.55}$$

where $\vec{r}(x, y, z)$ is a position vector.

### 4.2.5 Thomas Fermi

In the early twentieth century, Thomas and Fermi (TF) tried to narrow down the complexity of solving Schrödinger's equation for a multi-particle system through the use of the electronic density as a fundamental variable instead of the wave-function[103].

One advantage from this variable exchange is the reduction on the number of variables, since the wave function of a $N$ particle system is multi-electronic $\Psi(\vec{r}_1, ...., \vec{r}_N)$ whereas $\rho(\vec{r})$ only depends on three position coordinates [103].

In the Thomas-Fermi model, the total energy ($E_{\mathrm{TF}}$) is defined as a functional[5] of the electron density ($E_{\mathrm{TF}}(\rho(\vec{r}))$) and is given by[103],

$$E_{\mathrm{TF}}(\rho(\vec{r})) = C\int \rho(\vec{r})^{\frac{5}{3}}\mathrm{d}r + \int \vec{v}_{\mathrm{ext}}(\vec{r})\rho(\vec{r})\mathrm{d}r + \frac{1}{2}\int \frac{\rho(\vec{r}_{\mathrm{A}})\rho(\vec{r}_{\mathrm{B}})}{|\vec{r}_{\mathrm{A}} - \vec{r}_{\mathrm{B}}|}\mathrm{d}r_{\mathrm{A}}\mathrm{d}r_{\mathrm{B}} + E_{nn} \tag{4.56}$$

where $C = \left(3(3\pi^2)^{2/3}/10\right)$, $E_{nn}$ is the potential energy of nuclear interactions, the first term of the integral is an approximation of the kinetic energy of a non-homogeneous gas[6], the second term corresponds to the electronic repulsion and the third one is the energy component from the nuclei. The TF model is considered to be semi-classic because the only quantum effects included, in the kinetic

[4] If eq (4.55) is integrated over all space the probability is equal to one and the wave-function is said to be normalized.

[5] Takes a function as input and the output is a number from the function[97].

[6] For an electron independent homogeneous gas, the kinetic energy is given by $C\rho^{\frac{5}{3}}$ [97, 104].

energy, are the ones that arise from the Pauli's exclusion principle[104].

To obtain the ground state one can use an analogous form of the variational principle,

$$\left[\frac{\partial E_{\mathrm{TF}}(\rho(\vec{r})) - \mu_{\mathrm{TF}} \int \rho(\vec{r})dr - N}{\partial \rho(\vec{r})}\right] = 0 \tag{4.57}$$

Although TF model possesses a very intuitive derivation, its accuracy is very restricted due to the errors introduced by the neglection of the electron correlation [105].

### 4.2.6 The Hohenberg-Kohn theorem I

In 1964, based on the work of Thomas and Fermi, Hohenberg and Kohn (HK) presented and proved a theorem that validates the use of $\rho(\vec{r})$ as an underlying variable[106].

In their theorem, HK state that the energy of a ground state is a unique functional of the electron density[106], in other words, that there is a one-to-one mapping between the external potential ($\vec{v}_{\mathrm{ext}}$) and the electron density of the ground state[102].The proof to the latter theorem is quite simple and can be accomplished through *reductio ad absurdum*.

Consider two external potentials ($\vec{v}_{\mathrm{ext}}$) and ($\vec{v}^{'}_{\mathrm{ext}}$) that differ from more than one constant and produce the same electronic density $\rho(\vec{r})$. Associated to each one of these potentials is a specific Hamiltonian ($\hat{H}_{\mathrm{ext}}$) and ($\hat{H}^{'}_{\mathrm{ext}}$) which in turn are related to two different ground state wave-functions $\Psi$ and $\Psi^{'}$ that produce two energies, $E_0$ and $E^{'}_0$ with $E_0 \neq E^{'}_0$[106]. Hence, one may use the variational principle and work with $\Psi^{'}$ as a trial function,

$$E_0 < \langle \Psi^{'} | \hat{H}_{\mathrm{ext}} | \Psi^{'} \rangle = \langle \Psi^{'} | \hat{H}^{'}_{\mathrm{ext}} | \Psi^{'} \rangle + \langle \Psi^{'} | \hat{H}_{\mathrm{ext}} - \hat{H}^{'}_{\mathrm{ext}} | \Psi^{'} \rangle \tag{4.58}$$

Rewriting eq (4.58) in terms of ($\vec{v}_{\mathrm{ext}}$) and ($\vec{v}^{'}_{\mathrm{ext}}$) one has [106],

$$E_0 < E^{'}_0 + \int \rho(\vec{r}) \Big( \vec{v}_{\mathrm{ext}} - \vec{v}^{'}_{\mathrm{ext}} \Big) d\vec{r} \tag{4.59}$$

Doing the same reasoning but with label exchange in eq (4.59) one has,

$$E^{'}_0 < E_0 + \int \rho(\vec{r}) \Big( \vec{v}_{\mathrm{ext}} - \vec{v}^{'}_{\mathrm{ext}} \Big) d\vec{r} \tag{4.60}$$

Combining eq (4.59) and eq (4.60) leads to,

$$E_0 + E^{'}_0 < E^{'}_0 + E_0 \tag{4.61}$$

which concludes that the ground state $\rho(\vec{r})$ is uniquely defined by a $v(\vec{r})_{\mathrm{ext}}$ and that it is not possible that two different $v(\vec{r})_{\mathrm{ext}}$ give rise to the same ground state $\rho(\vec{r})$[106].

### 4.2.7 Hohenberg-Kohn theorem II

Because there are one-to-one[7] mappings between $\vec{v}_{\text{ext}} \longleftrightarrow \Psi(\vec{r}) \longleftrightarrow \rho(\vec{r})$ it is possible to write the energy as a functional of the electron density,

$$E(\rho) = F_{\text{HK}}(\rho) + \int \rho(\vec{r}) v(\vec{r})_{\text{ext}} d\vec{r} + E_{\text{nn}} \tag{4.62}$$

where $F_{\text{HK}}$ is a universal functional without dependency in an external potential, which allows the use of the same functional for every atom or molecule. The energy of the ground state corresponds to the global minimum of $F_{\text{HK}}$ and can be calculated with the variational principle[101].

To work with DFT, there is only one problem left to solve, the "shape" of $F_{\text{HK}}$.

### 4.2.8 Kohn-Sham equations

In 1965 Kohn and Sham (KS) proposed a formula for $F_{\text{HK}}$. In their derivation, KS abandoned the idea of a multi-particle inter-actuating system and worked with a non inter-actuating system where the particles move in a mean local effective external potential ($v_{\text{eff}}(\vec{r})$) [107]. The latter system can be described by the following Hamiltonian operator [8],

$$\hat{H}_{\text{eff}} = \sum_{i=1}^{N} -\frac{1}{2}\nabla_i^2 + \sum_{i=1}^{N} v_{\text{ext}}(\vec{r}_i) + \sum_{i=1}^{N} v_{\text{eff}}(\vec{r}_i) \tag{4.63}$$

which basically is a sum of one-electron operators, a much simpler form of the Hamiltonian in eq (4.46) for a multi-particle inter-actuating system.

For the case of *fermions*[9], such as electrons, the KS wave-functions ($\Psi^{\text{KS}}$) are defined as a single *Slater determinant*[97, 101],

$$\Psi^{\text{KS}} = \frac{1}{\sqrt{N!}} \begin{bmatrix} \chi_1(\zeta_1) & \chi_2(\zeta_1) & \cdots & \chi_N(\zeta_1) \\ \chi_1(\zeta_2) & \chi_2(\zeta_2) & \cdots & \chi_N(\zeta_2) \\ \vdots & \vdots & \ddots & \vdots \\ \chi_1(\zeta_N) & \chi_2(\zeta_N) & \cdots & \chi_N(\zeta_N) \end{bmatrix} \tag{4.64}$$

where $(N!)^{-1/2}$ is a normalization factor that accounts for the interchange of any pair of particles[10] and $\chi(\zeta)$ are wave-functions known as *spin-orbitals* with $\zeta$ denoting the *spin* and *position* of each single electron[97].

Thus, the ground state of a system with $N$ non inter-actuating electrons is defined as a Slater

[7] Degenerated ground states are an exception because there is more than one wave-function associated with the same ground state. This is common in open shell atoms.

[8] Atomic units were used $\hbar = 1, e = 1$ and electron mass $m_e = 1$.

[9] Particles that have half-integer spin and behave in agreement with the Fermi-Dirac statistics.

[10] This permutation mathematically corresponds to an interchange of two columns that leads to a sign change in the determinant[97].

determinant of orbitals $\Psi_i^{\mathrm{KS}}(\vec{r})$ that are the solutions of,

$$\left(-\frac{1}{2}\nabla^2 + v_{\mathrm{eff}}(\vec{r})\right)\Psi_i^{\mathrm{KS}}(\vec{r}) = \epsilon_i \Psi_i^{\mathrm{KS}}(\vec{r}) \tag{4.65}$$

$$v_{\mathrm{eff}}(\vec{r}) = v_{\mathrm{ext}}(\vec{r}) + \int \frac{\rho(\vec{r})}{|\vec{r} - \vec{r'}|} d\vec{r'} + \frac{\partial E_{xc}}{\partial \rho(\vec{r})} \tag{4.66}$$

where the eigenvalue $\epsilon_i$ corresponds to the orbital energy of $\Psi^{\mathrm{KS}}$ and the last term in eq (4.66) is the exchange-correlation potential. Due to the central idea of KS derivation it is possible to write the functional $F_{HK}(\rho[\vec{r}])$ as,

$$F_{HK}[\rho(\vec{r})] = T(\rho(\vec{r})) + \frac{1}{2}\int \frac{\rho(\vec{r})\rho(\vec{r'})}{|\vec{r} - \vec{r'}|} d\vec{r'} d\vec{r} + E_{xc}[\rho(\vec{r})] \tag{4.67}$$

where $E_{\mathrm{xc}}[\rho(\vec{r})]$ is the functional of exchange and correlation that accounts for all electron-electron interactions and $T(\rho(\vec{r}))$ is the kinetic energy given by,

$$T(\rho(\vec{r})) = -\frac{1}{2}\sum_{i=1}^{N} \int \Psi_i^{*\,KS}(\vec{r})\nabla^2 \Psi_i^{\mathrm{KS}}(\vec{r}) d\vec{r} \tag{4.68}$$

Recalling that the energy is written in respect to a universal functional, the total energy ($E_{\mathrm{tot}}$) of the system is defined as,

$$E_{\mathrm{tot}}(\rho(\vec{r})) = T(\rho(\vec{r})) + \int \rho(\vec{r}) v_{\mathrm{ext}}(\vec{r}) d\vec{r} + F_{HK}(\rho(\vec{r})) + E_{nn} \tag{4.69}$$

The difficult part of DFT, and by extension of TD-DFT as it will be presented later, is in the computation of $E_{\mathrm{xc}}[\rho(\vec{r})]$ because its exact form is unknown. Hence, approximations to the functional must be done.

### 4.2.9 Exchange-correlation energy approximations

John Perdew[108, 109] organized the main density functionals for exchange-correlation energy calculations as a Jacob's ladder.

His analogy suggests that the accuracy, computational cost, and complexity for $E_{xc}[\rho(\vec{r})]$ gets higher as one climbs the ladder from the "Earth" level (Hartree world) to "Heaven" level where chemical accuracy is reached with energy errors around 1kcal.mol$^{-1}$[110]. Fig (4.1) shows a schematic representation of the Jacob's ladder.

The Hartree world includes approximations that do not take into account the self-interaction correction by neglecting the exchange-correlation potential from the KS equations.

The first rung is the most basic functional approximation, the *Local Density Approach (LDA)*. In LDA the idea is that $E_{\mathrm{xc}}$ density is equal at every position in space similarly to the uniform electron

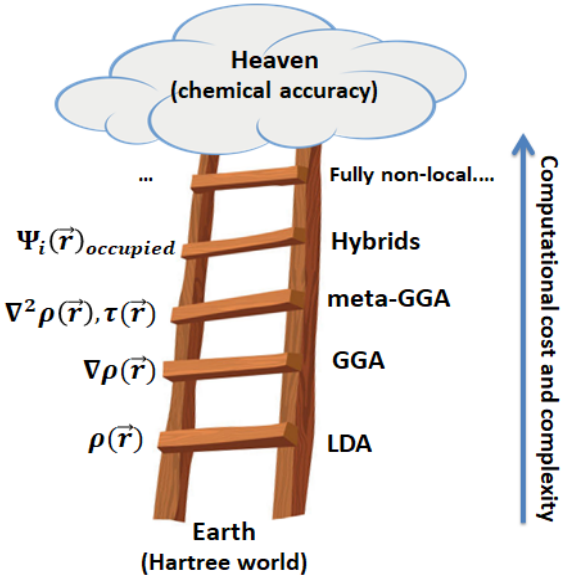


Figure 4.1: Jacob's ladder.

gas, which is basically the TF model previously presented(see subsection 4.2.5 chapter 4). Due to its very local behaviour, LDA tends to overestimate the strengths of chemical bonds near the equilibrium geometry[111]. Associated to LDA is the SPWL functional.

Up in the ladder is the *Generalised Gradient Approximation (GGA)*, this method not only possess a dependency on the electronic density but also in its gradient. The use of the latter quantity allows a better description of the molecule's natural unhomogeneous electron density. GGA results have shown better results than LDA in total and atomization energies[112–114] and structural energy differences[115–117]. Some examples of GGA functionals are BLYP, PBE, BP86,HCTC and BPW91[118].

Next is the *meta-Generalised Gradient Approximation (meta-GGA)*. This method is built on the GGA formalism, and has a higher accuracy than the latter due to the consideration of the local kinetic energy density ($\tau(\vec{r})$). This quantity is defined as the sum over all occupied KS orbitals,

$$\tau(\vec{r}) = \frac{1}{2}\sum_{i}^{\text{occ}} \left(\Psi_i^{\text{KS}}(\vec{r})\right)^2 \tag{4.70}$$

This reformulation has shown to improve the description of different types of chemical bonds, e.g metallic and covalent, when compared to GGA and LDA[109, 119–121]. Some popular meta-GGA functionals are the TPSS, SCAN, and M06-L[109, 119–122].

*Hybrid functionals* are based on the idea of combining a portion (*gamma*) of the exact Hartree-Fock exchange energy ($E_x^{HF}$) with the exchange and correlation energies from other approximations,

$$E_{xc}^{\text{hybrid}} = \gamma E_x^{\text{HF}} + (1-\gamma)E_x^{\text{GGA}} + E_c^{\text{GGA}} \tag{4.71}$$

with the term $E_x^{\mathrm{HF}}$ computed by resorting to the KS molecular orbitals,

$$E_x^{\mathrm{HF}}[\Psi_i^{\mathrm{KS}}] = -\sum_{i=1}^{\frac{N}{2}}\sum_{j=1}^{\frac{N}{2}}\int\int \frac{\Psi_i^{\mathrm{KS}*}(\vec{r})\Psi_i^{\mathrm{KS}}(\vec{r})\Psi_j^{\mathrm{KS}*}(\vec{r})\Psi_j^{\mathrm{KS}}(\vec{r})}{|\vec{r}-\vec{r'}|}d\vec{r}d\vec{r'} \tag{4.72}$$

The determination of the right percentage of $\gamma$ is done empirically through the fitting of experimental data such as ionization energies, total energy, atomic energies and others[123, 124]. To this group belong the functionals B3LYP, PBE0, PBE1PBE, mPW1K[118].

The fifth rung in Jacob's ladder include the most complex and time consuming functionals. One example of these approximations are the double hybrid functionals such as B2LYP, BEGP-PLYP and one with dispersion-corrected B97-D[118].

In this thesis all the electronic structure calculations were carried out at the hybrid level of approximation, due to its fair ratio of accuracy vs computational cost, with PBE0 as a choice of work functional. A functional accuracy test was not carried out on this thesis since Duque *et al.*[125] already tested B3LYP, PBE0 and M06HF for ATZ, CTZ and 3CTZ and concluded, through the study of excitation energies, wave numbers and absorption spectra, that PBE0 was the most suitable functional.

### 4.2.10 TD-DFT

Time-dependent density functional theory (TD-DFT) allows the study of the excited state dynamics of a N body system in the presence of *time-dependent* potentials such as an electric or magnetic fields. The evolution of a wave-function over time is given by the time-dependent Schrödinger equation,

$$\hat{H}(t)\Psi(\vec{r},t) = -i\hbar\frac{\partial\Psi(\vec{r},t)}{\partial t} \tag{4.73}$$

Because the HK theorem is derived based on the assumption of static potentials and static electron density, it is not valid for TD-DFT.

To overcome this problem, in 1984 Runge and Gross (RG) developed, and proved, a theorem that is an extension of HK to the time dependent case which states there is a one-to-one mapping between $v_{\mathrm{ext}}(\vec{r},t) \longleftrightarrow \Psi(\vec{r},t) \longleftrightarrow \rho(\vec{r},t)$[11].

### 4.2.11 Time dependent Kohn-Sham equations

The previous trick of a non-interactuating system, used by KS in the time-independent case can also be applied for TD-DFT[12]. At this moment one can just extend the KS formalism to the current

[11] The mathematical proof of RG theorem will not be reproduced in this thesis for brevity, however full derivation can be consulted in [104]

[12] This is validated by the van Leeuwen theorem. The latter is quite complex and mathematically demanding to allow a brief reproduction, hence further reading on the subject can be done at [104]

time-dependency problem,

$$v_{\text{eff}}(\vec{r},t) = v_{\text{ext}}(\vec{r},t) + \int \frac{\rho(\vec{r},t)}{|\vec{r}-\vec{r'}|} d\vec{r'} + v_{\text{xc}}(\vec{r},t) \tag{4.74}$$

The right side terms in eq (4.74) are similar to the ones from the static case but now written with a time dependency. The only exception is the term $v_{\text{xc}}(\vec{r},t)$ that now is defined as a functional of the quantum mechanical action[13] instead of the energy,

$$v_{\text{xc}}(\vec{r},t) = \frac{\partial A_{xc}}{\partial \rho(\vec{r},t)} \tag{4.75}$$

Finally, as it was done before, $\rho(\vec{r},t)$ can be computed as a sum over all N single particle orbitals,

$$\rho(\vec{r},t) = \sum_{i}^{N} |\Psi_i^{\text{KS}}(\vec{r},t)|^2 \tag{4.76}$$

### 4.2.12 DFT and TD-DFT from a computational point of view

The eigenvalue problem discussed so far can be solved computationally through an iterative mechanism[101]. Fig (4.2) below shows a flow chart of DFT/TD-DFT computation and a schematic representation of its iterative behaviour.

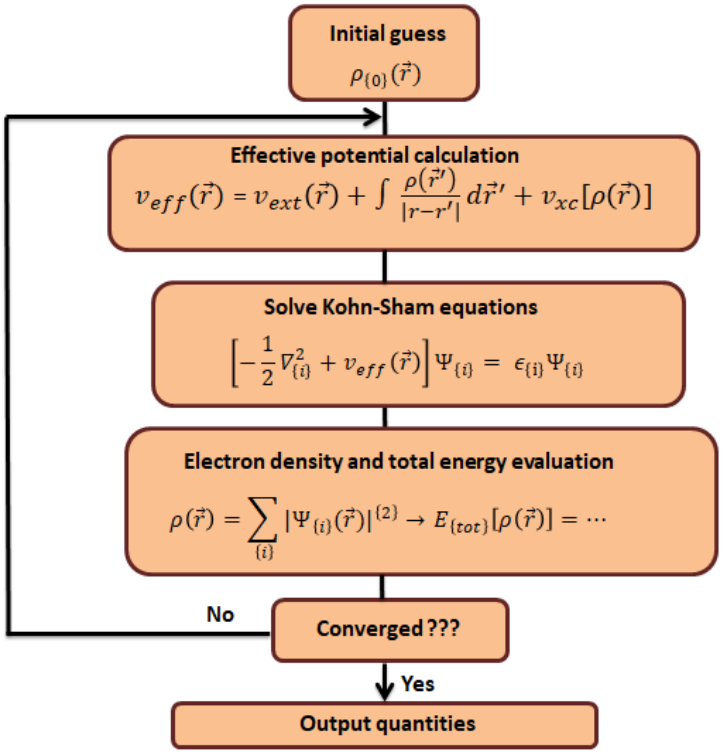


Figure 4.2: Flowchart for DFT/ TD-DFT computation.

[13]The quantum mechanical action is defined as an abstract quantity used to describe the motion of the system[126].

The process begins with a guess on the electronic density, $(\rho_0(\vec{r}))$, in order to allow the computation of $v_{\text{eff}}$ and solve the Kohn-Sham equations. The resolution of the latter generates a new electronic density,$(\rho(\vec{r}))$, from the single-electron orbitals. The value of $\rho(\vec{r})$ is then compared with $\rho_0(\vec{r})$ in respect to a previously defined convergence criteria. If the difference between the densities is smaller than the value of the *convergence criteria*, self-consistency is achieved and the iterative process is finished. Then the ground state electronic density is computed followed by the desired properties. For TD-DFT a similar iterative scheme is also used.

If one chooses a more tight convergence (smaller value for the cut-off), the precision/accuracy will be higher but the time will also escalate. In ORCA software the value of the convergence criteria has the range $10^{-n}, n = 6 - 10 \in \mathbb{N}$. In TD-DFT the iterative behaviour is similar to DFT.

With this, the electronic part of the system is completed, however the nuclear part is still missing. Due to the Born-Oppenheimer approximation (see Chapter 4, subsection 4.2.2) Schrödinger's equation can be replaced by Newton's law of motion, with the necessary forces computed in agreement with the *Hellmann-Feynman theorem*[101, 127]. The latter states that there is a relationship between the derivative of the total energy with respect to a criterion $(\lambda)$ and the expectation value of the Hamiltonian regarding that same parameter,

$$\frac{dE_\lambda}{d\lambda} = \left\langle \Psi_\lambda \middle| \frac{d\hat{H}}{d\lambda} \middle| \Psi_\lambda \right\rangle \tag{4.77}$$

For the particular case of molecular forces the parameter $\lambda$ will be the nuclear coordinates $R$. The force $F$ that acts upon a atomic nucleus is given by,

$$F = \sum_i F_i = -\frac{\partial E}{\partial R_i} = -\left\langle \Psi \middle| \frac{\partial \hat{H}}{\partial R_i} \middle| \Psi \right\rangle = -\int \rho(\vec{r}) \frac{\partial V_{en}(R,r)}{\partial R_i} - \frac{\partial V_{nn}(R)}{\partial R_i} dr \tag{4.78}$$

Unfortunately, the latter theorem is not valid for time-dependent wave-functions since it is fully derived based on the time-independent Schrödinger equation. However, it is possible to work with[128],

$$\left\langle \Psi_\lambda(t) \middle| \frac{\partial \hat{H}}{\partial \lambda} \middle| \Psi_\lambda(t) \right\rangle = i\hbar \frac{\partial}{\partial t} \left\langle \Psi_\lambda(t) \middle| \frac{\partial \Psi_\lambda(t)}{\partial \lambda} \right\rangle \tag{4.79}$$

The computation of the forces is similar to the one previously presented in eq (4.78).

### 4.2.13 Basis sets

In order to carry out the computations with electronic structure methods one needs a *basis set*. The latter consist of a group of known mathematical functions to describe an unknown one, such as a molecular orbital(MO). To study molecular systems, particularly for MO's calculation, the choice of basis functions are the atomic orbitals (AO)[101].

Each MO is expanded within the Linear Combination of Atomic Orbitals (LCAO) approximation

[101],

$$\Phi_i = \sum_r^N c_{ri}\chi_r \tag{4.80}$$

where $\chi_r$ are the AO's, $c_{ri}$ are coefficients associated to the contribution of each AO for the description of the MO[14], $\Phi_i$ is the MO and $N$ is the total number of AO's considered. The latter expansion is done under the assumption that the final number of MO's is equal do the number of initial AO's[101].

There are two key groups of functions used in a basis set: STO (*Slater Type Orbitals*) and GTO(Gaussian Type Orbitals). The main difference between the two is the exponential term that possesses a dependency in the distance of the electron to the atomic nucleus ($r_{nuc}$), for instance in STO this is $e^{-r_{nuc}}$[101] and for GTO is $e^{-r_{nuc}^2}$[101] . Fig (4.3) below shows the comparison of a $1s$ orbital function constructed with GTO and STO.

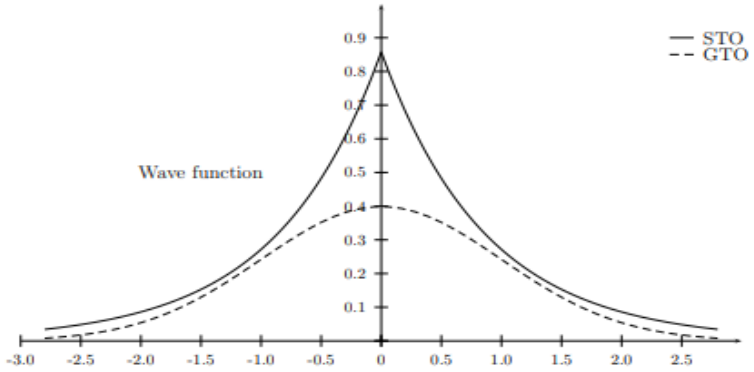


Figure 4.3: Comparison between STO and GTO, adapted from[129].

The quadratic dependence of GTO does not allow a proper description of the electron density near the nucleus[129]. The latter should be a sharp peak instead of a "bell" shape since the electron can not be in the nucleus. Also, the exponential decay (tail) does not depict the correct asymptotic behaviour of the wave-function far from the nucleus[129]. Despite their disadvantages, GTO's integration is easier and one can use a linear combination of them to produce a STO, also called *contracted GTO's*. However, any function that is not a natural solution of the Schrödinger's equation exhibits slow convergence and a need for a higher number of Slater determinants to compute the final result[129]. Even so, combinations of GTO's are preferred because their easy integration surpasses the excessive time needed[101, 129].

It is possible to classify the basis sets regarding the number of functions of the basis. The *minimal* basis set uses the number of functions that only allows the description of the electrons of the neutral atom[101]. One way to improve the basis is to *double* all the functions, which produces a *DoubleZeta*. The doubling of the number of functions itself already produces a higher accuracy, specially describing

[14]These coefficients are calculated and optimized during the iterative cycle of DFT.

systems with $\sigma$ and $\pi$ bonds[101]. It is also possible to *triple*($TZ$),*quadrople*($QZ$) or *quintuple*($5Z$) the number of functions. Although it may seem a very practical solution, it has a tremendous computational cost which is not fairly compensated. This is because the chemical bond only takes place between the valence orbitals. To overcome this issue, one can just do a *split valence basis* and increase only the number of valence orbitals. One can also include polarization effects with *polarization functions (p)* and *diffusion functions(aug)*[15] to describe the electron very far away from the nucleus, essential for calculations with anions, Rydberg states and very electronegative atoms.

Also relevant for this thesis are the *correlated-consistent (cc)* basis. This type of functions allow a better description of the correlation effects by retrieving some of the correlation energy from the valence electrons[101]. The work on this thesis was carried out with the cc-pVDZ basis set[16][17] due to its features that were previously described.

[15]The (p) and (aug) notation is for *Dunning basis set type.* The notation for diffuse/polarization functions is different from basis set to basis set, for instance in Pople's set one has diffuse (+) and polarization(*)[101].

[16]Although there is an enormous number of types of basis sets with different features that could be included, they are not relevant for the work on this thesis.

[17]Similarly to the work functional, no accuracy test was done regarding the basis sets since this task was already completed by Duque *et al.* [125]

# Chapter 5

# Discussion and Results

In this chapter the aim is to present and discuss the results obtained from the computational calculations. The exposition starts with the computational details at which the electronic structure calculations were carried out.

The latter is followed by an analysis composed of two parts: structural and dynamic. The structural analysis of ATZ, CTZ and 3CTZ is done through the study of their electronic parameters and vibrational frequency spectra in methanol.

Regarding the dynamic analysis, it consists of the study of the photophysical behaviour of ATZ, CTZ and 3CTZ with the presentation of the absorption/emission spectra and the computed results for the rate constants with PIA and FSTF.

The chapter finishes with the presentation of the energy analysis of the two possible photochemical pathways for intramolecular proton transfer in CTZ and 3CTZ, and with the study of the molecular polarizability as a marker for selectivity in photochemical paths.

## 5.1 Details

All calculations have been carried out using the ORCA software package version 5.0.3. The geometry optimization and frequency analysis of the electronic ground state was carried out at the DFT PBE0/cc-pVDZ level of theory. For the excited electronic states, $S_1$ and $T_1$ the same type of analysis was performed but at the TD-DFT PBE0/cc-pVDZ level of theory.

Implicit solvent effects of methanol, for both ground and excited states, were taken into account with the conductor-like polarizable continuum model (CPCM) from ORCA (REF ORCA MANUAL DO CPCM). Later, to study the effect of different solvents' polarity (water and ammonia) in the polarizability values CPCM flag was also activated.

For the electronic structure calculations the following physical constants were considered: methanol's dielectric constant $\varepsilon_{\text{methanol}} = 32.63$ and refractive index $n_{\text{methanol}} = 1.329$, water refractive index

$n_{\text{water}} = 1.333$ and dielectric constant $\varepsilon_{\text{water}} = 80.44$, acetonitrile refractive index $n_{\text{ammonia}} = 1.33$ and dielectric constant $\varepsilon_{\text{ammonia}} = 22.4$, pressure= 1.00 atm and temperature $T$=298.15K.

Rate constant calculation was performed with both FSTF and PIA. For path integral approach the results were computed with ORCA's ESD module.

## 5.2 Structural Analysis

The vibrational analysis will consist on the detailed description of the six more intense vibrational modes of ATZ, CTZ and 3CTZ, in their $S_0$, $S_1$ and $T_1$ electronic states, from the IR spectra in methanol predicted theoretically.

### 5.2.1 Vibrational analysis of ATZ

Fig (5.1) below shows the theoretical predicted vibrational spectrum of ATZ in the electronic state $S_0$ in methanol.

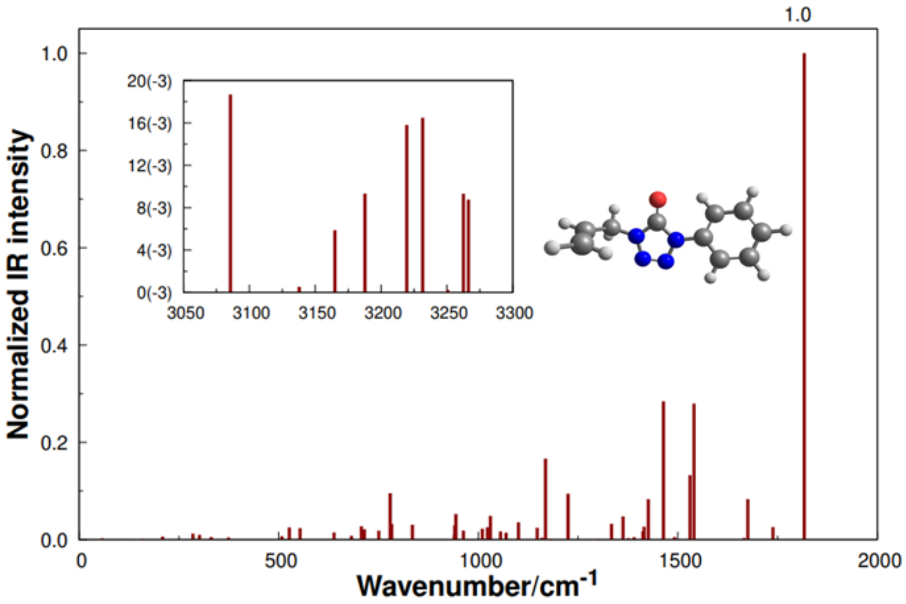


Figure 5.1: Normalized vibrational spectrum of ATZ-$S_0$ in methanol.

Because ATZ is composed by 25 atoms it has 75 active vibrational modes[1]. Reading the spectrum from the right to the left, one has the most intense peak at 1816.89 cm$^{-1}$ which corresponds to the elongation of the C=O bond. Next, the peak at 1540.62 cm$^{-1}$ is associated to the movement of the hydrogen atoms from the phenyl group.

The peak at 1464.09 cm$^{-1}$ is related to the vibration of the nitrogen atoms in the $1^{st}$ and $4^{th}$ position of the tetrazolic ring. As these atoms move, so does the carbon chain from the alyl group

[1]Number of vibrational modes is 3N where N is the number of atoms in the molecule.

and the atoms from the phenyl group.

From the most intense peaks three remain: 1168.76 $cm^{-1}$, 779.53 $cm^{-1}$ and 1530.87 $cm^{-1}$. These are a result of the up and down movement of the nitrogen atoms from the $2^{nd}$ and $3^{rd}$ ring positions, the alyl group vibration that brings it a little bit out of plane, and the N=N vibration, respectively.

Fig (5.2) and fig (5.3) below present a schematic representation of the six more intense vibrational modes of ATZ. The blue arrows in some atoms are the displacement vectors that give the direction in which the bond vibration takes place.

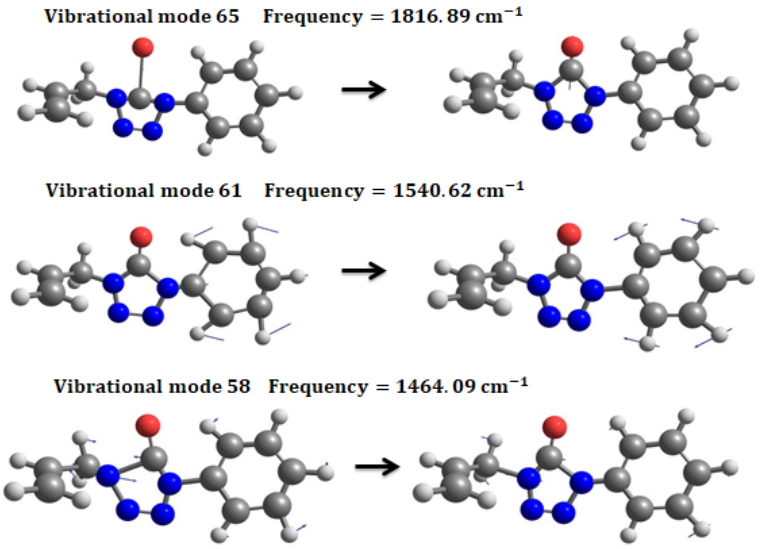


Figure 5.2: Schematic representation of the three more intense vibrational modes of ATZ $-$ $S_0$ in methanol.

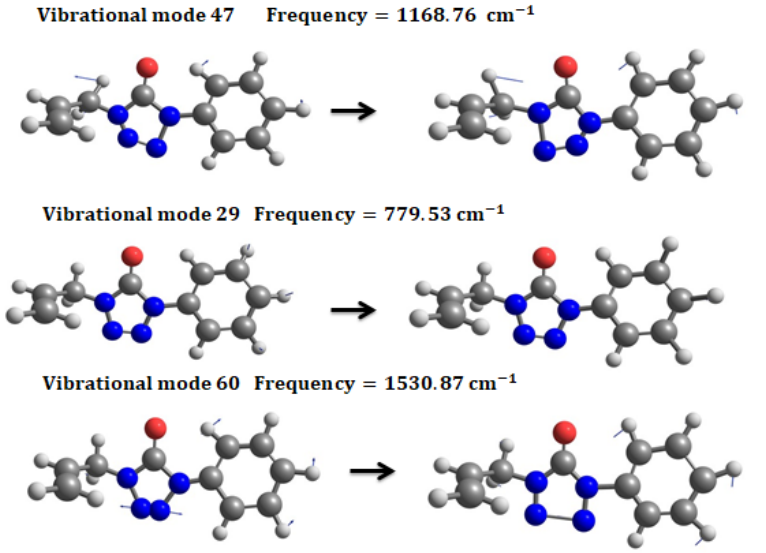


Figure 5.3: Schematic representation of the next three more intense vibrational modes of ATZ $-$ $S_0$ in methanol.

Regarding the vibrational footprint of ATZ-$S_1$, all the signatures are very similar to the ones in the ground state. The predicted vibrational spectrum of ATZ in the electronic state $S_1$ in methanol

can be consulted in the appendix chapter in fig (A.1).

An interesting vibrational behaviour is observed when ATZ is in the $T_1$ electronic state. Fig (5.4) below shows the predicted vibrational spectrum of ATZ in the electronic state $T_1$ in methanol. The

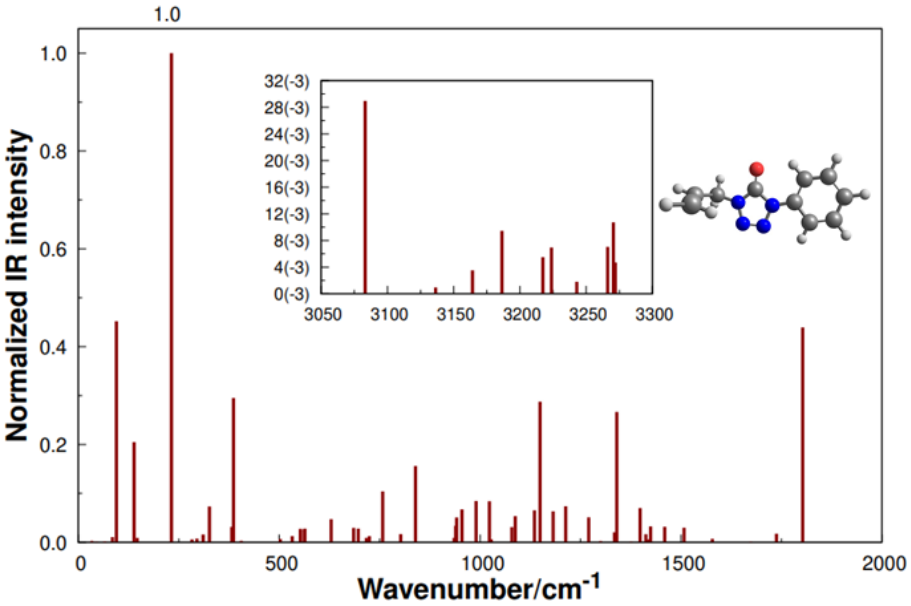


Figure 5.4: Normalized vibrational spectrum of ATZ-$T_1$ in methanol.

most intense vibrational mode, the peak at 231.82 $cm^{-1}$, is due to the vibration of the phenyl group. The latter induces an elongation of the N=N bond in the tetrazole's ring and the N-C bond that connects the phenyl group to the ring itself. The second most intense peak at 1802.95 $cm^{-1}$ is related to the elongation of the C=O bond. Next, the peak at 94.86 $cm^{-1}$ is associated to the vibration of the carbon chain from the alyl group. This movement allows the widening of the tetrazole's ring which also brings the phenyl group up and down.

The peak at 386.16 $cm^{-1}$ is also a result from a up-down like movement but from the carbonyl group which is caused by the elongation of the N-C bond that connects the phenyl group to the tetrazole ring. These vibrations make the tetrazole ring to "close" and "open"resulting in a longitudinal vibration of the alyl group and the stretching of the C-C bonds in the phenyl group. The vibration of the alyl's $CH_2$- group, directly bound to the ring, leads to the up-down movement of the nitrogen atom in the $1^{st}$ ring position. At the same time, the transversal vibration of the hydrogen atoms from phenyl group also causes up-down movement of the nitrogen atom in the $4^{th}$ ring position. These two behaviours give rise to the peak at 1149.16 $cm^{-1}$.

The peak at 1340.31 $cm^{-1}$ is caused by the vibration of the hydrogen atoms from the first carbon of the alyl group, directly bound to the ring, which leads to the up and down movement of the N-C bond that connects the alyl directly to the tetrazole ring. Below, figs (5.5, 5.6) show schematically these six more intense vibrational modes for ATZ-$T_1$.

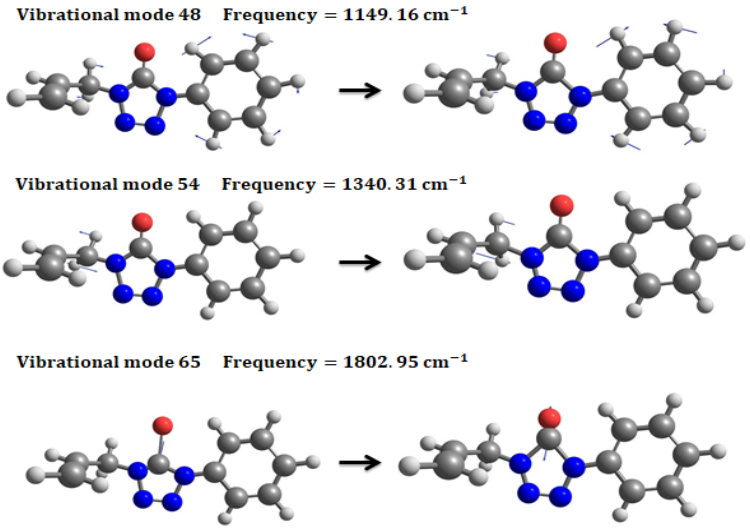


Figure 5.5: Schematic representation of the three more intense vibrational modes of ATZ-$T_1$ in methanol.

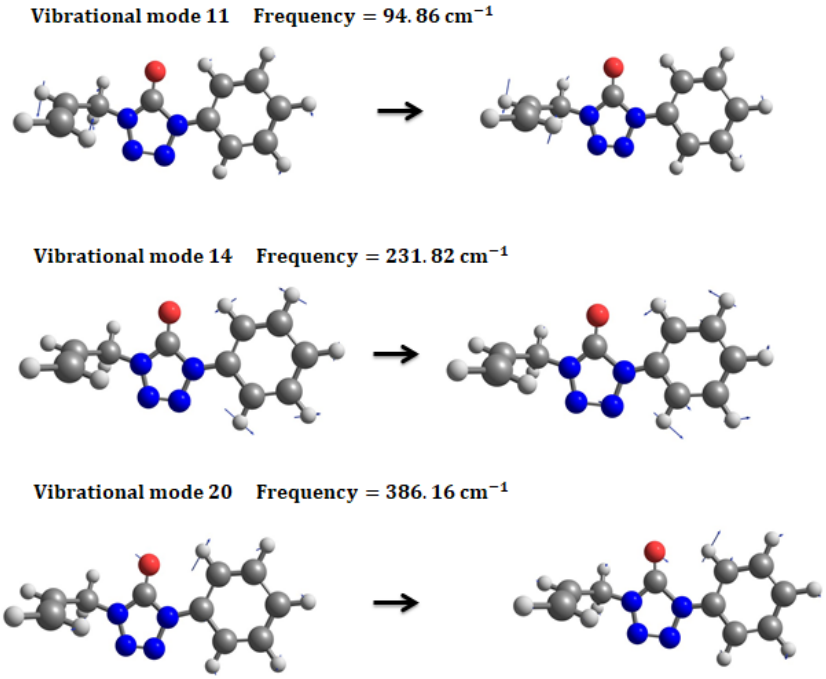


Figure 5.6: Schematic representation of the next three more intense vibrational modes of ATZ-$T_1$ in methanol.

### 5.2.2 Vibrational analysis of CTZ

For CTZ there are 96 vibrational modes since the molecule has 32 atoms. Regarding CTZ-$S_0$ vibrational spectrum, it possesses some similarities with the vibrational spectrum of ATZ-$S_0$. Figure (5.7) below shows the predicted and normalized vibrational spectrum of CTZ-$S_0$ in methanol.

At 1809.87 $cm^{-1}$ is CTZ's most intense vibrational mode which is associated with the elongation of the C=O bond. Next, the second most intense peak, located at 1540.21 $cm^{-1}$, is due to the elongations of the C-C bonds from the phenyl group that also make the N-C and N=N bonds , from

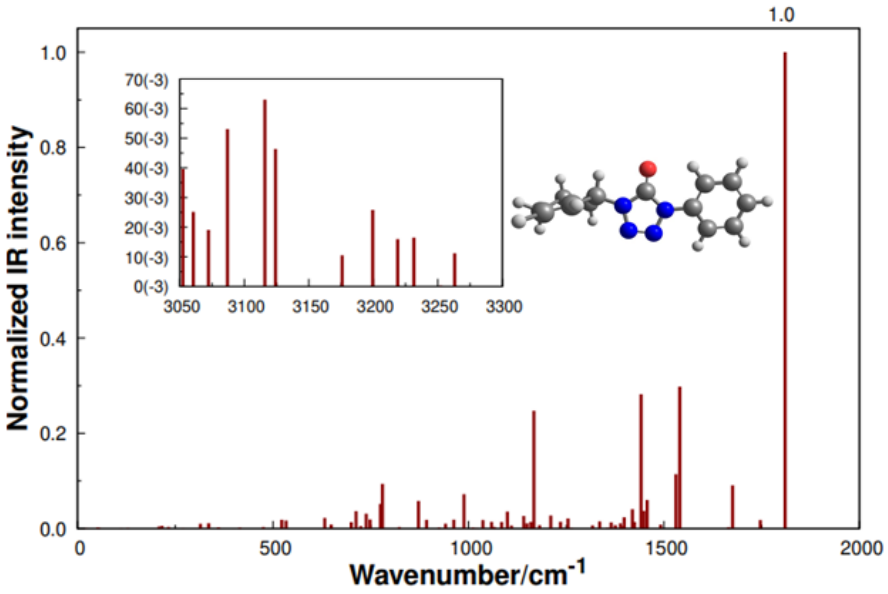


Figure 5.7: Normalized vibrational spectrum of CTZ-$S_0$ in methanol.

the nitrogen atoms at the $1^{st}$,$2^{nd}$ and $3^{rd}$ ring positions, to stretch.

The peak at 1441.62 $cm^{-1}$ comes from the horizontal vibration of the carbon atom from the carbonyl group. This also leads to a horizontal vibration of the nitrogen atoms from the $1^{st}$ and $4^{th}$ positions in the tetrazol ring. As a consequence of the latter, the phenyl and cyclohexanyl groups also vibrate.

The up-down movement of the nitrogen atoms from the $2^{nd}$ and $3^{rd}$ positions in the tetrazole ring, give rise to the peak at 1167.35 $cm^{-1}$. Next, in decreasing intensity are the peaks at 1530.41 $cm^{-1}$ and 779.9 $cm^{-1}$. The first appears from the elongation of the N-N bond from the $2^{nd}$ and $3^{rd}$ positions from the tetrazole ring and the second is due to the vibration of the hydrogen atoms in and out of the plane (twisting).

Lastly, from the seven more intense vibrational modes is the peak at 1676.02 $cm^{-1}$ originated from the elongations of the C-C bonds from the phenyl group.

The most particular vibrational signature of CTZ's is the intensity of the group of peaks between $3000 - 3127$ $cm^{-1}$ which are much more intense than for ATZ. These correspond to the vibrations of the C-H bonds from the cyclohexanyl group.

The seven more intense vibrational modes of CTZ-$S_0$ in methanol, previously discussed, are schematically presented below in figs (5.8, 5.9). The blue arrows in some atoms are the displacement vectors that give the direction in which the bond vibration takes place.

Regarding CTZ-$S_1$, the vibrational signatures are very similar to the ones of CTZ-$S_0$. Hence, the spectrum of CTZ-$S_1$ in methanol can be consulted in the appendix chapter in fig (A.2). To finish the vibrational study of CTZ only CTZ-$T_1$ is missing.

The predicted spectrum for the latter in methanol is presented in fig (5.10). The most intense

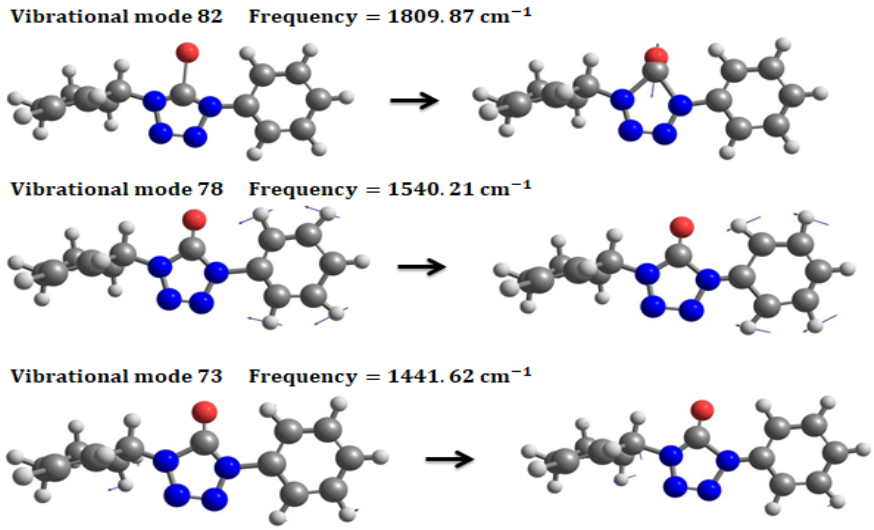


Figure 5.8: Three more intense vibrational modes of CTZ-$S_0$ in methanol.

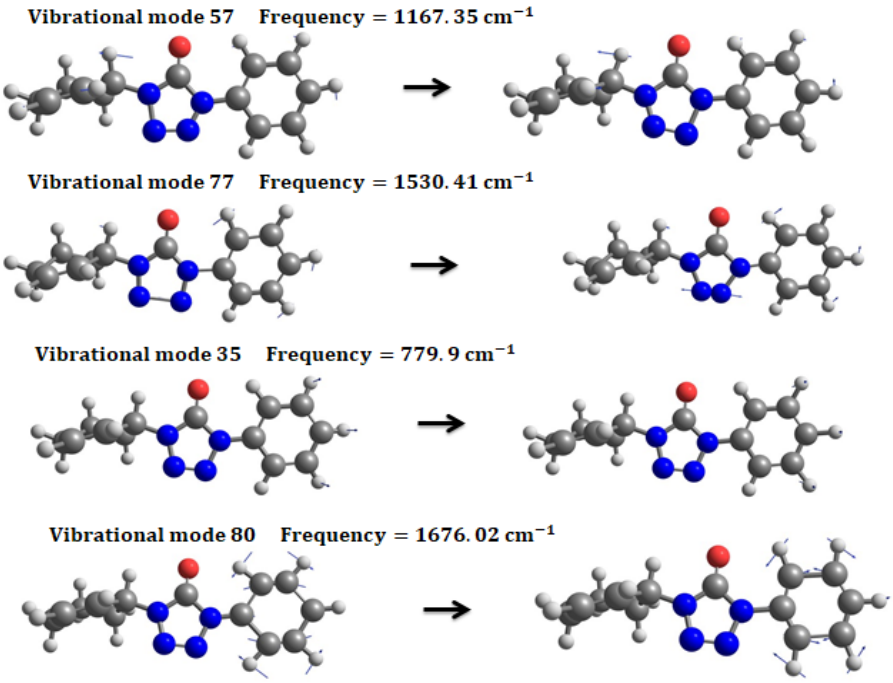


Figure 5.9: Last four more intense vibrational modes of $CTZ - S_0$ in methanol.

peak, at 1338.26 cm$^{-1}$, is a product of the horizontal vibration of the carbonyl group that drags the nitrogen atoms from the $1^{st}$ and $4^{th}$ positions of the tetrazole ring. In turn, because the latter are connected with the phenyl and cyclohexanyl groups, respectively, this also makes them to vibrate horizontally. The second most intense peak is placed at 1826.75 cm$^{-1}$ and it is due to the elongation of the C=O bond from the carbonyl group. The peak at 1525.52 cm$^{-1}$ is associated with the stretching of the C-C bonds from the phenyl group, that also leads to the movement of the hydrogen atoms directly bound to this group. The fourth most intense vibrational mode is placed at 774.4 cm$^{-1}$ and is related to the out-of-plane movement (twisting) of the hydrogen atoms from the phenyl group.

Next, the peak at 1222.99 cm$^{-1}$ is related to the asymmetrical stretching of the carbon atom of the

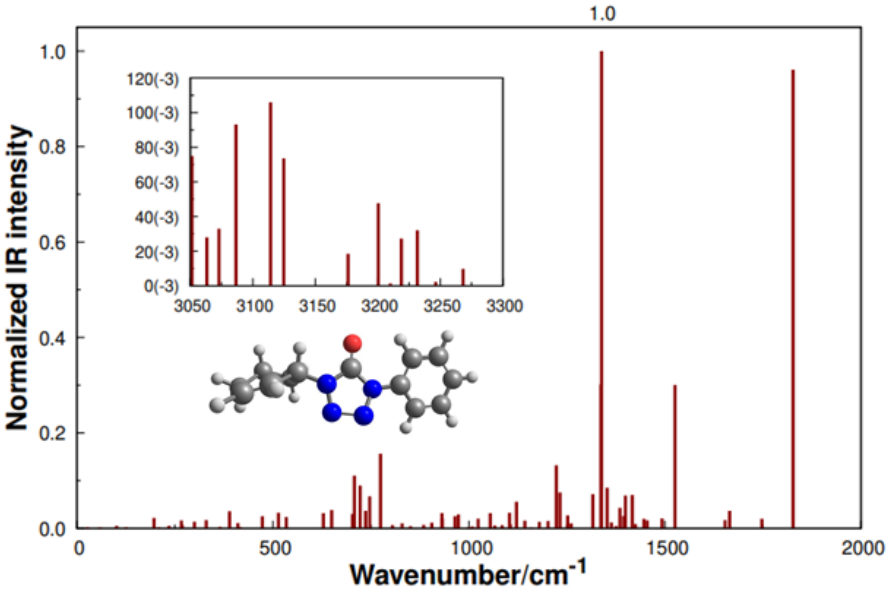


Figure 5.10: Normalized vibrational spectrum CTZ-$T_1$ in methanol.

cyclohexanyl group that is bound to the nitrogen atom at the $4^{th}$ position of the tetrazole ring. From the six more intense vibrational modes, the least intense is placed at 3114cm$^{-1}$ which corresponds to the elongation of the C-H bonds from the carbons C19 and C30 in the 3-methyl-cyclohexanyl group (the atom's numbering can be consulted in chapter 1 section 1.5).

Below, figs (5.11,5.12) show a schematic representation of the six more intense vibrational modes of CTZ-$T_1$.

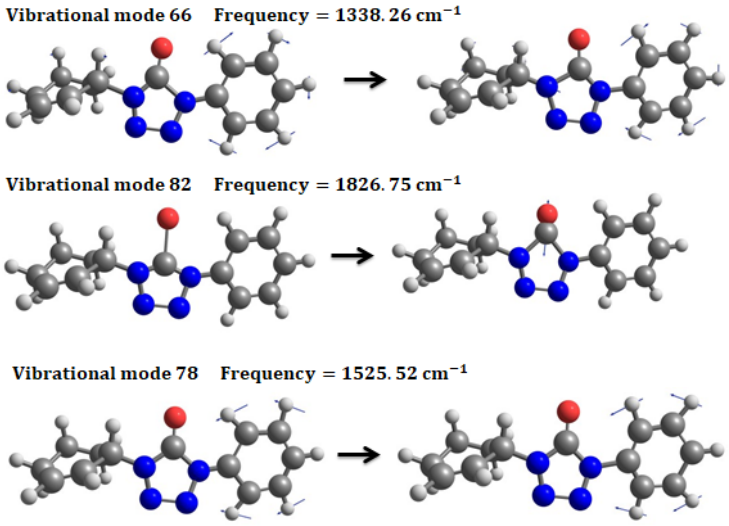


Figure 5.11: Three more intense vibrational modes of CTZ-$T_1$ in methanol.

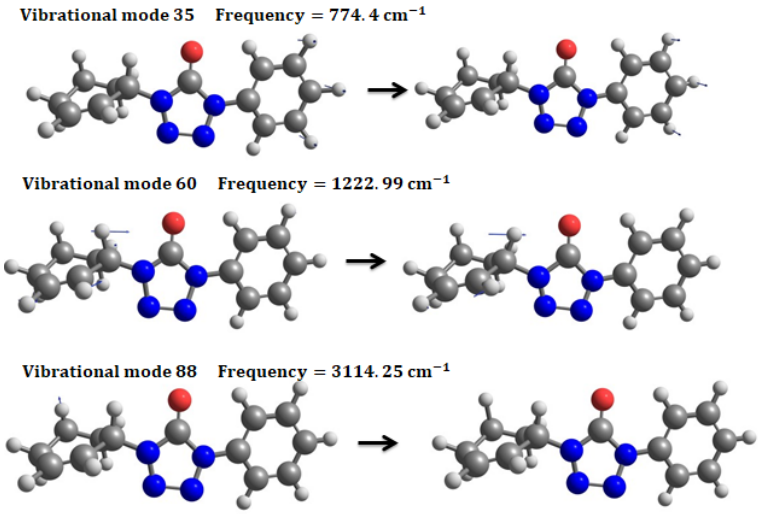


Figure 5.12: Next three more intense vibrational modes of CTZ-$T_1$ in methanol.

### 5.2.3 Vibrational analysis of 3CTZ

Contrasting with the previously presented molecules is 3CTZ because it possesses very distinct vibrational spectra for each electronic spin state. Fig (5.13) shows the predicted vibrational spectrum of 3CTZ-$S0$ in methanol. For 3CTZ, since it has 35 atoms, there are 105 vibrational modes. Overall, the

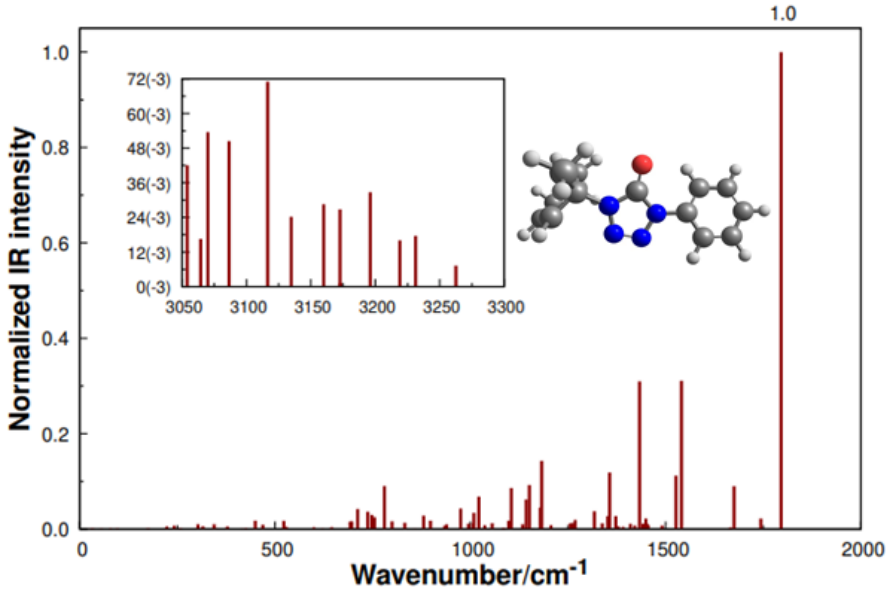


Figure 5.13: Normalized vibrational spectrum of 3CTZ-$S_0$ in methanol.

vibrational spectrum of 3CTZ-$S_0$ is very similar to CTZ-$S_0$. The main differences between the two are the intensity of the peaks and the absence of the peak at 1167.35 cm$^{-1}$ corresponding to CTZ-$S_0$ $57^{th}$ vibrational mode.

For 3CTZ-$S_0$, in general, the peaks are more intense (in absolute value), specially in the region of $3000 - 3127$ cm$^{-1}$.The intensity of the peaks in an IR vibrational spectrum is proportional to the

variation of the dipole moment of the molecule that is induced by the vibrations, more specifically is proportional to the square of the latter variation[130].[2] Because 3CTZ has more "absorbing bonds", due to its higher number of atoms than CTZ, this means that the bond's vibration will induce a bigger change in the molecule's dipole moment than in CTZ[130].

The second difference can be explained by resorting to the molecular structure of 3CTZ-$S_0$. In CTZ-$S_0$ the intense peak at 1167.35 $cm^{-1}$is related to the up-down movement of the nitrogen atoms from the $2^{nd}$ and $3^{rd}$ positions in the tetrazole ring. For 3CTZ-$S_0$, the latter is substituted by three less intense peaks, range $1103 - 1186$ $cm^{-1}$, that correspond to the vibration of the hydrogen atoms from the 3-methyl-cyclohexanyl group. Below, figs (5.14,5.15) show a schematic representation of the six more intense vibrational modes of 3CTZ-$S_0$.

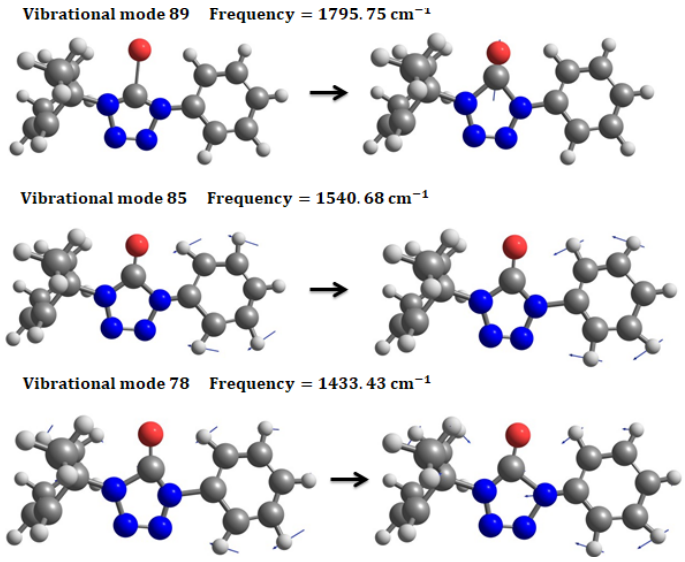


Figure 5.14: Three more intense vibrational modes of 3CTZ-$S_0$.

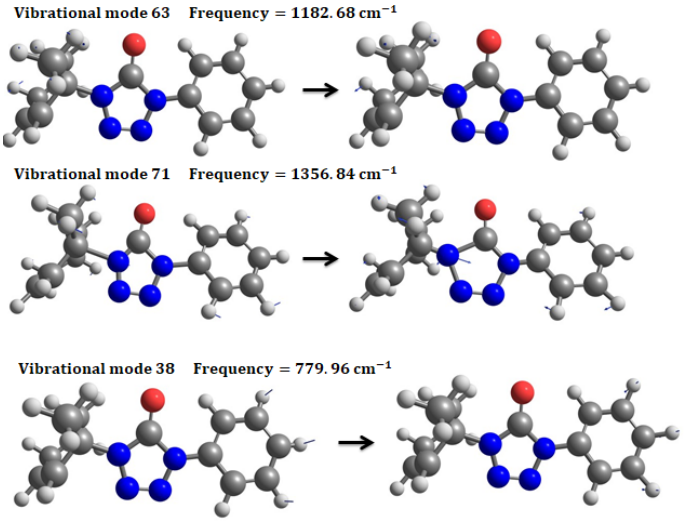


Figure 5.15: Next three more intense vibrational modes of 3CTZ-$S_0$.

[2]The absolute intensity also depends on the concentration of the sample. A higher concentration leads to more intense peaks because one has a bigger number of absorbing molecules.

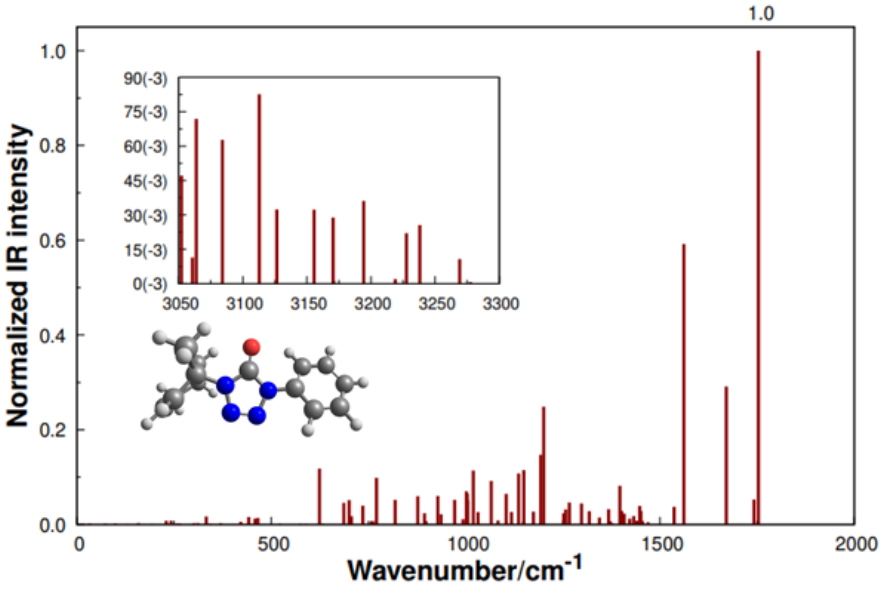


Figure 5.16: Normalized vibrational spectrum of 3CTZ-$S_1$ in methanol.

Fig (5.16) above shows the theoretically predicted vibrational spectrum of 3CTZ-$S_1$ in methanol. Similarly to 3CTZ-$S_0$, the most intense peak corresponds to the C=O elongation, being placed at 1753.23 $cm^{-1}$. The second most intense peak, located at 1561.45 $cm^{-1}$, is related to the symmetric stretching of the N-C bond, nitrogen atom that is bound to the phenyl group, which also leads to the stretching of the C-C bonds in the phenyl group.

The peak at 1670.69 $cm^{-1}$ is a consequence of the elongation of the C-C bonds between the $8^{th}$,$9^{th}$,$11^{11}$ and $12^{th}$ carbon atoms from the phenyl group that also make the tetrazole ring to "open" and the C=O bond to elongate. The horizontal vibration of the hydrogen atoms from the $CH_2$- groups and the elongation of the $C-CH_3$ bond, in the 3-methyl-cyclohexanyl group, are responsible for the fourth most intense peak at 1200.88 $cm^{-1}$.

The peak at 686.78 $cm^{-1}$ is due to the expansion and contraction of the cyclohexanyl group which in turn makes the $CH_3$- group to come out of the rings plane. From the six more intense peaks, the least intense is located at 623.91 $cm^{-1}$ and is related to the out-of-plane movement of the hydrogen atoms from the phenyl group.

A schematic representation of the six more intense vibrational modes of 3CTZ-$S_1$ is done below in figs (5.17,5.18).

Lastly, an in order to conclude the vibrational analysis of the studied tetrazolones, is 3CTZ-$T_1$ vibrational footprint. The vibrational spectrum of 3CTZ-$T_1$,presented below in fig (5.19), is very similar to the one from CTZ-$T_1$.

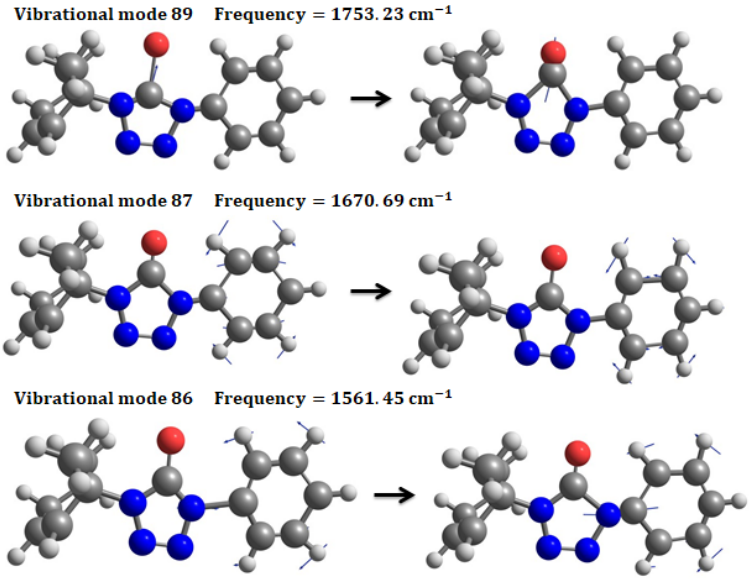


Figure 5.17: Three more intense vibrational modes of 3CTZ-$S_1$.

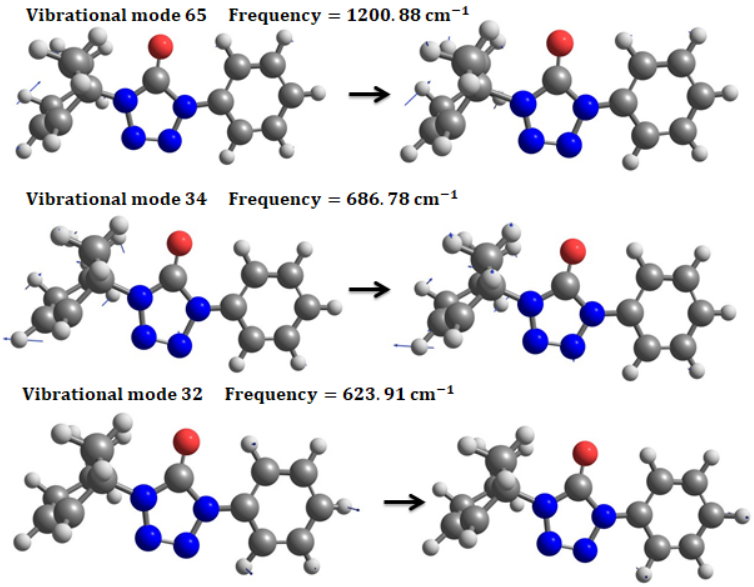


Figure 5.18: Next three more intense vibrational modes of 3CTZ-$S_1$.

The main difference between the two is in the intensity of the peak around 1800 cm$^{-1}$ associated with the C=O elongation. In 3CTZ-$T_1$ the latter is less intense because of the movement of the bond does not cause a strong variation in the dipole moment. Due to the similarity, no detailed analysis will be performed for 3CTZ-$T_1$ vibrational modes. Bellow figs (5.20,5.21) display a schematic representation of the six more intense vibrational modes of 3CTZ-$T_1$.

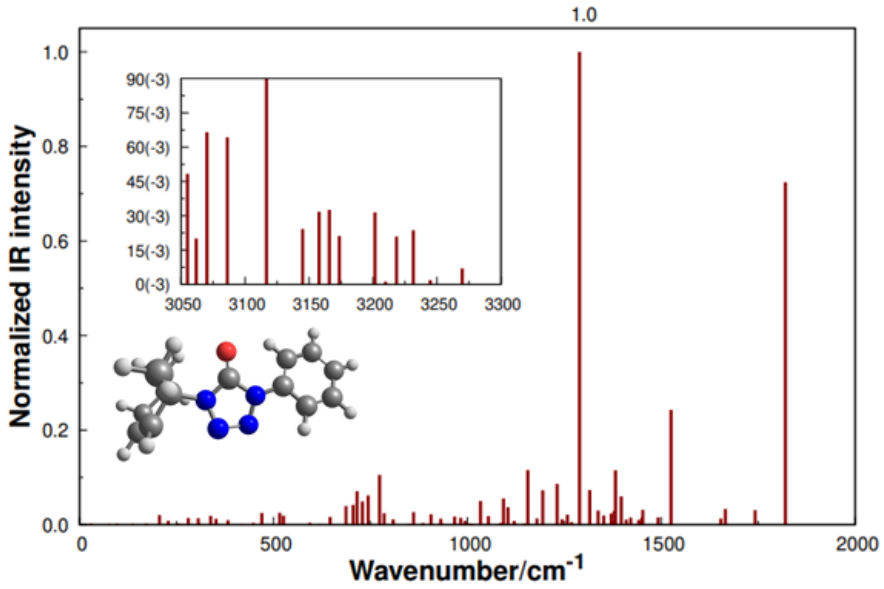


Figure 5.19: Normalized vibrational spectrum of 3CTZ-$T_1$ in methanol.

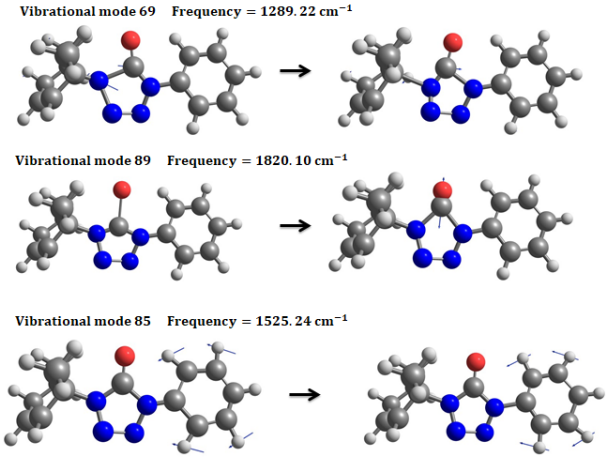


Figure 5.20: Three more intense vibrational modes of 3CTZ-$T_1$.

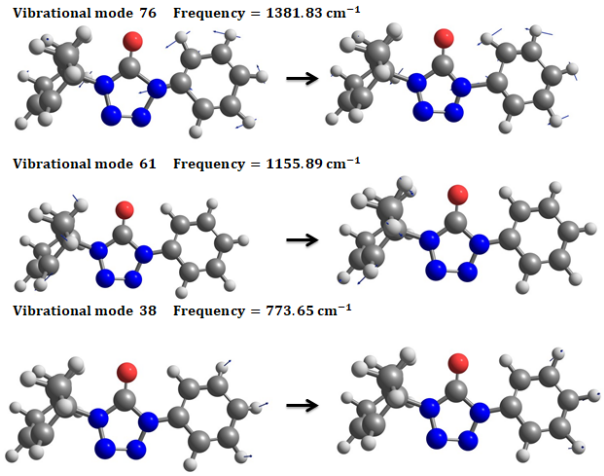


Figure 5.21: Next three more intense vibrational modes of 3CTZ-$T_1$.

### 5.2.4 Energetic analysis of ATZ

To allow a proper description of the electronic states from ATZ, CTZ and 3CTZ one needs to conduct an energetic analysis. Let's start with ATZ, table (5.1) summarizes the energy values for its three electronic spin states.

Table 5.1: Electronic energy and ZPE (in Eh) for ATZ-$S_0$, ATZ-$S_1$ and ATZ-$T_1$ in methanol calculated at the PBE0/cc-pVDZ level of theory.

| Electronic state | Electronic energy | ZPE |
|---|---|---|
| $S_0$ | -680.553834 | 0.195129 |
| $S_1$ | -680.369452 | 0.189562 |
| $T_1$ | -680.429281 | 0.187995 |

The energy values show that, as expected, ATZ-$S_0$ is the most stable species possessing the lowest electronic energy value. Since singlet states involve the pairing of electrons one may think that ATZ-$S_1$ would be more stable then ATZ-$T_1$ because the electrons with opposite spin stabilize one another.

Although that is true, an extra stabilization takes place in the triplet excited state. This is because, in the latter, one has two unpaired electrons with the same spin orientation (parallel) allowing them to exchange their position. The energy term associated with this phenomenon is negative, which lowers the overall energy of the spin system, thus making the ATZ-$T_1$ state more stable then ATZ-$S_1$.

In order to compute the rate constants, particularly with the FSTF method, one needs some energy parameters such as the *adiabatic energy difference* ($E_{kl}$) and the *vertical excitation energy*, also called Franck Condon energy ($\Delta E_{FC}$). Figure (5.22) below shows a schematic representation of the vertical excitation mechanism to help in the understanding of the latter process.

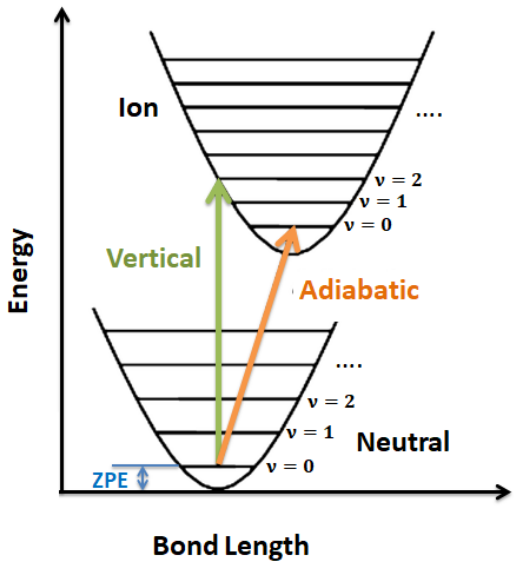


Figure 5.22: Adiabatic (orange arrow), Franck Condon (green arrow) excitations and zero point energy (ZPE) (blue arrow) [131]. The different values of $\nu$ represent the vibrational levels

If an electron is excited from the ground state to an excited state without any nuclear rearrangement, it is said to be a vertical excitation (green arrow). The energy difference between the two states involved in the latter transition is the $\Delta E_{\mathrm{FC}}$ and is computed under the assumption of the Franck Condon principle (FCP) which is a Born-Oppenheimer like approximation.

FCP states that, due to the large difference between the nuclear and electronic masses and their dynamical time-scale, when an electronic transition takes place the nuclear geometry can be considered to be fixed[132]. Opposite to vertical excitation is the adiabatic excitation (orange arrow), also called diagonal excitation, which involves the relaxation of both ground and excited sate structures, meaning that they will be as stable as possible thus allowing the transition to take place between two global energy minima. As a consequence, $\Delta E_{\mathrm{FC}}$ value is higher than the adiabatic excitation energy difference.

It is important to not confuse $E_{\mathrm{kl}}$, which is an adiabatic energy difference with the energy of the adiabatic excitation . The similarity between the two lies in the fact that both allow geometry relaxation. The difference is that $E_{\mathrm{kl}}$ can be computed between any two electronic states in their equilibrium geometry whereas the energy of the adiabatic excitation energy must be amid the ground and an excited electronic state. Table (5.2) below presents $\mathrm{E_{kl}}$, $\Delta E_{\mathrm{FC}}$ and $\mathrm{E_{0-0}}$ values for ATZ in methanol.

Table 5.2: Adiabatic energy difference, FC energy and $\mathrm{E_{0-0}}$ (in kJ.mol$^{-1}$) for ATZ in methanol.

| **Electronic Transition** | $\mathrm{E}_{kl}$ | $\Delta E_{\mathrm{FC}}$ | $\mathbf{E}_{0-0}$ |
|---|---|---|---|
| $S_0 \rightarrow S_1$ | 484.08 | 485.88 | 469.476 |
| $S_1 \rightarrow T_1$ | 154.89 | ... | 160.155 |
| $S_0 \rightarrow T_1$ | 327.01 | .... | 308.283 |

Looking at the results the first thing that one notices is that the values of $\Delta E_{\mathrm{FC}}$ were not computed for the $S_1 \rightarrow T_1$ neither for $S_0 \rightarrow T_1$ transition. But why?

Recalling $\Delta E_{\mathrm{FC}}$ definition, one can see that the latter is done at the expense of an excitation mechanism, the $S_1 \rightarrow T_1$ and $S_0 \rightarrow T_1$ transitions are not included since they are a singlet state deactivation pathway and a double excitation (first one excites to $S_1$ and then it decays to $T_1$), respectively. In fact, as already mentioned, during the excitation process the system goes from a lower energy state to an higher energy state, which would not be the case for $S_1 \rightarrow T_1$ transition since ATZ-$S_1$ electronic energy is higher than ATZ-$T_1$.

Of course one could also think about RISC which, according to the latter statement, is an excitation process. The reason why it was also not considered is related to the nature of $\Delta E_{\mathrm{FC}}$ definition that includes the ground state $S_0$ in the transition.

Analysing the obtained values of $E_{\mathrm{kl}}$ one can see that $S_0 \rightarrow S_1$ possesses the highest energy value, this can be explained by the large energy difference between $S_0$ and $S_1$ electronic states. The $S_1 \rightarrow T_1$

transition has the lowest energy value, which is expected since these electronic states are very close energetically. These results are in agreement with the energetic arrangement of the Jablonsky diagram in fig (2.1).

The computation of $E_{0-0}$ can be accomplished by summing the zero point energy (ZPE) to the electronic energy of each state. The fluctuations of $E_{0-0}$ are similar to $E_{kl}$ since both are dependent on the same variable which is the optimized electronic energy.

### 5.2.5 Energetic analysis of CTZ

Table (5.3) summarizes the energy values for the three studied electronic spin states of CTZ in methanol. Regarding the energetic parameters computed for CTZ, as expected, CTZ-$S_0$ is the most stable species possessing the lowest electronic energy. From the studied excited states, CTZ-$T_1$ also presents a lower electronic energy value being the second most stable electronic spin state. The arguments previously used for ATZ can be employed to also justify CTZ's results.

Table 5.3: Electronic and ZPE energies (in Eh) for CTZ-$S_0$, CTZ-$S_1$ and CTZ-$T_1$ in methanol.

| **Electronic state** | **Electronic energy (Eh)** | **ZPE (Eh)** |
|---|---|---|
| $S_0$ | -797.172091 | 0.260525 |
| $S_1$ | -797.006304 | 0.256140 |
| $T_1$ | -797.061053 | 0.257243 |

The values of $\Delta E_{\mathrm{FC}}$ and $E_{\mathrm{kl}}$ for CTZ in methanol are presented below in table (5.4).

Table 5.4: Adiabatic energy difference, FC energy and $E_{0-0}$ (in kJ.mol$^{-1}$) for CTZ in methanol.

| **Electronic Transition** | $E_{\mathrm{kl}}$ | $\Delta E_{\mathrm{FC}}$ | $E_{0-0}$ |
|---|---|---|---|
| $S_0 \rightarrow S_1$ | 435.27 | 482.53 | 423.76 |
| $S_1 \rightarrow T_1$ | 143.61 | ..... | 142 |
| $S_0 \rightarrow T_1$ | 291.52 | ..... | 282.91 |

Analysing the results it is possible to confirm that similar conclusions to the ATZ results can be drawn for CTZ, the $S_0 \rightarrow S_1$ transition is the most energetically demanding and $S_1 \rightarrow T_1$ is the least. These results are in agreement with the obtained values for the electronic energy values presented in table (5.3) and can be justified with the same arguments used for ATZ's energetic analysis.

### 5.2.6 Energetic analysis of 3CTZ

The same energetic parameters were collected for 3CTZ and are presented below in tables (5.5,5.6).

Looking at 3CTZ's energy values, one can confirm that 3CTZ-$S_0$ is the most stable electronic spin state possessing the lowest electronic energy value. With the reasoning done before, it is possible to

understand once again why 3CTZ-$T_1$ is more stable than 3CTZ-$S_1$.

Table 5.5: Electronic energy and ZPE (in Eh) for 3CTZ-$S_0$, 3CTZ-$S_1$ and 3CTZ-$T_1$ in methanol.

| **Electronic state** | **Electronic energy (Eh)** | **ZPE (Eh)** |
|---|---|---|
| $S_0$ | -836.438116 | 0.287915 |
| $S_1$ | -836.270257 | 0.283204 |
| $T_1$ | -836.326062 | 0.284643 |

Table 5.6: Adiabatic energy difference, FC energy and $E_{0-0}$ (in kJ.mol$^{-1}$) for 3CTZ in methanol.

| **Electronic Transition** | $E_{\mathrm{kl}}$ | $\Delta E_{\mathrm{FC}}$ | $\mathbf{E}_{0-0}$ |
|---|---|---|---|
| $S_0 \rightarrow S_1$ | 440.71 | 488.66 | 428.34 |
| $S_1 \rightarrow T_1$ | 146.51 | ... | 141.77 |
| $S_0 \rightarrow T_1$ | 294.19 | ... | 285.59 |

Similarly to CTZ and ATZ, the $\Delta E_{\mathrm{FC}}$ and $E_{\mathrm{kl}}$ results for 3CTZ confirm once again that the transition between the ground and the first excited singlet state is the most energetic.

The energy values of HOMO-LUMO and HOMO+1-LUMO-1, and their representation for each electronic spin state of the approached tetrazolones, were also computed and can be consulted in the appendix chapter.

## 5.3 Photophysical Analysis

With the structural analysis completed it is now time to enter the dynamic study of the photophysical behaviour of ATZ, CTZ and 3CTZ.

### 5.3.1 Absorption spectra of ATZ, CTZ and 3CTZ

Starting with ATZ, fig (5.23) shows the absorption spectrum theoretically predicted in methanol. Comparing the latter with the experimental results obtained by Duque Prata *et.al* [125], presented in fig (A.6), ATZ's predicted spectrum presents an error of 10.4% corresponding to a 26 nm shift from the experimental obtained maximum value of 250 nm. In this range, the maximum absorbance of ATZ takes place at 224 nm with a molar absorptivity value of $\varepsilon = 938$ cm$^2$.mmol$^{-1}$. The latter can be explained by the presence of the aromatic ring in ATZ's structure. It is also possible to notice two very well defined bands away from the range of the experimental spectrum, one divided into two peaks at 158 nm ($\varepsilon = 3170$ cm$^2$.mmol$^{-1}$) and 178 nm ($\varepsilon = 2652$ cm$^2$.mmol$^1$) and one other at 305 nm ($\varepsilon = 1378$ cm$^2$.mmol$^{-1}$). The latter can possibily arise from vibronic effects[125]. This spectral behaviour is in agreement with the predictions done by Duque Prata *et. al* in their previous work [125].

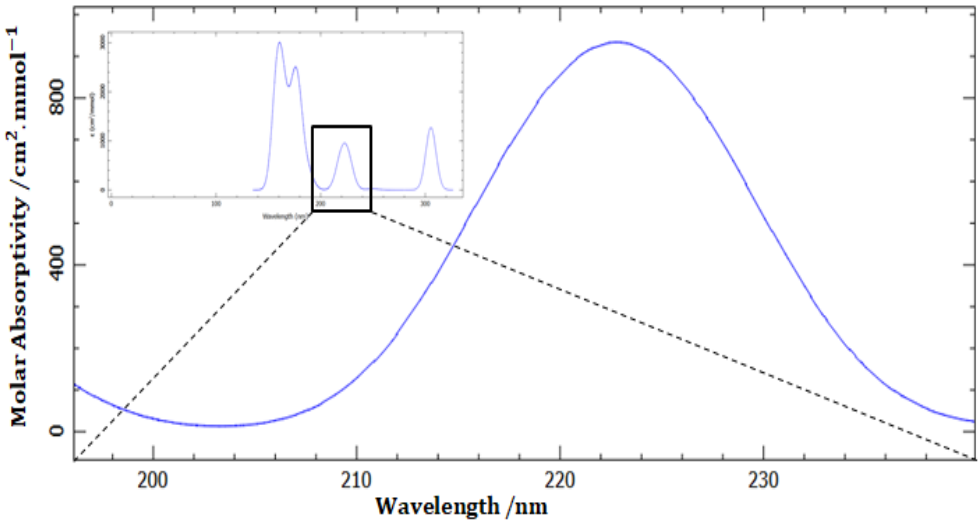


Figure 5.23: Theoretically predicted $UV_{vis}$ absorption absorption spectrum of ATZ in methanol.

Resorting to the oscillator strength and transition dipole moment values it is possible to associate which states are involved in the transition that give rise to each absorption band. Table (5.7) below presents the computed oscillator strength and transition dipole moment values for ATZ in methanol. For brevity, table (5.7) summarizes the values in the range of each band. Nonetheless, the evaluation of the absorption data was done with the computation of first thirty singlet excited states.

Table 5.7: Absorption data via transition electric dipole moment for ATZ in methanol.

| State | Energy/ $cm^{-1}$ | Wavelength/ nm | $f_{oscilator}$ | $M/(a.u)^2$ | $M_x/(a.u)$ | $M_y/(a.u)$ | $M_z/(a.u)$ |
|---|---|---|---|---|---|---|---|
| $S_1$ | 32756.6 | 305.3 | 0.548048 | 5.50802 | -2.33119 | 0.05894 | 0.26478 |
| $S_6$ | 40171.5 | 223.7 | 0.232668 | 1.71339 | 0.78958 | -1.03656 | -0.12445 |
| $S_{15}$ | 56109.4 | 178.2 | 0.420627 | 2.46795 | -1.36463 | 0.77818 | 0.01263 |
| $S_{30}$ | 63233.7 | 158.1 | 0.807404 | 4.20357 | -0.62341 | -0.58569 | 1.86330 |

Looking at the results from table (5.7) it is possible to conclude that the electronic transition responsible for the peak, in the range of the experimental spectrum, is the $S_0 - S_6$. The strongest transition is predicted to take place between $S_0 - S_{30}$ electronic states.

The absorption spectrum of CTZ, presented in fig (5.24), presents a similar spectral behaviour to ATZ. Considering the range of the experimental spectrum, consult fig (A.7), one can once again detect a maximum at 223 nm with a molar absorptivity of $\varepsilon = 938$ $cm^2.mmol^{-1}$, and a deviation of 27 nm from the experimental value. It is possible to identify two more bands one at 304 nm and 178 nm with molar absorptivity values of $\varepsilon = 2289$ $cm^2.mmol^{-1}$ and $\varepsilon = 4323$ $cm^2.mmol^{-1}$ respectively. Close to the latter peak is also a visible shoulder, this type of spectral signature can arise from vibronic effects such as the *Jahn-Teller effect* that arises from geometrical distortions, in a non-linear molecule, that reduce the symmetry and energy of the system.

To clarify which electronic transitions give rise to the bands in CTZ's absorption spectrum the

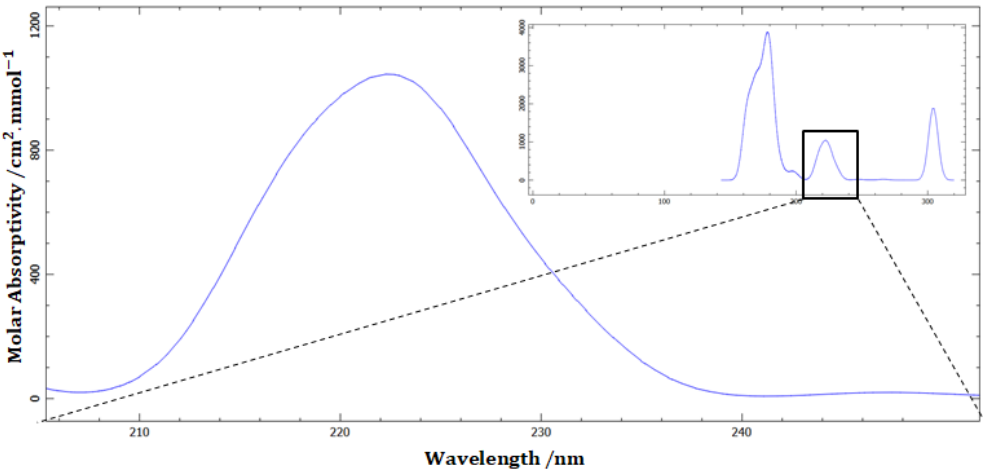


Figure 5.24: Theoretically predicted $UV_{vis}$ absorption absorption spectrum of CTZ in methanol.

oscillator strength and transition dipole moments values were calculated and are presented below in table (5.8).

Table 5.8: Absorption data via transition electric dipole moment for CTZ in methanol.

| State | Energy/ cm$^{-1}$ | Wavelength/ nm | $f_{\text{oscilator}}$ | $M$/(a.u)$^2$ | $M_x$/(a.u) | $M_y$/(a.u) | $M_z$/(a.u) |
|---|---|---|---|---|---|---|---|
| $S_1$ | 32875.8 | 304.2 | 0.60473514 | 6.05570 | -2.46049 | 0.02317 | -0.03405 |
| $S_6$ | 44717.7 | 223.6 | 0.258162226 | 1.90059 | -0.99388 | -0.95024 | 0.09915 |
| $S_{18}$ | 55624.7 | 179.8 | 0.699722656 | 4.14127 | -1.99926 | -0.37952 | 0.01443 |
| $S_{24}$ | 58847.7 | 169.9 | 0.371104132 | 2.07607 | -1.37576 | -0.38353 | 0.19039 |

Analysing the data, it is possible to conclude that the most intense band corresponds to the $S_0 - S_{18}$ transition. Regarding the range of the experimental spectrum, the transition $S_0 - S_6$ is responsible for the band in this region. Close to 300 nm, the $S_0 - S1$ electronic transition gives rise to the maximum at 304.2 nm.

The theoretically predicted absorption spectrum of 3CTZ is presented in fig (5.25). For 3CTZ in the range of the experimental spectrum, consult fig (A.8), one has a maximum at 222 nm with a molar absorptivity of $\varepsilon = 1380$ cm$^2$.mmol$^{-1}$ which corresponds to a deviation of 27 nm and an error of 10.8% in respect to the experimental data. The presence of the shoulders before and other after this maximum are due to less intense electronic transitions. Out of the experimental range, it is possible to identify two intense bands, one at 299 nm with $\varepsilon = 3113$ cm$^2$.mmol$^{-1}$ and another at 177 nm with a molar absorptivity value of $\varepsilon = 5031$ cm$^2$.mmol$-1$. Table (5.9) below, presents the obtained values of oscillator strength and transition dipole moment for 3CTZ in methanol. Looking at the results one can conclude that the most intense band is related to the transition between $S_0 - S_{20}$ states, and that in the experimental region the dominant transition is between $S_0 - S_6$.

Lastly, one can also conclude that the band placed at higher wavelengths is due to the $S_0 - S_1$ transition.

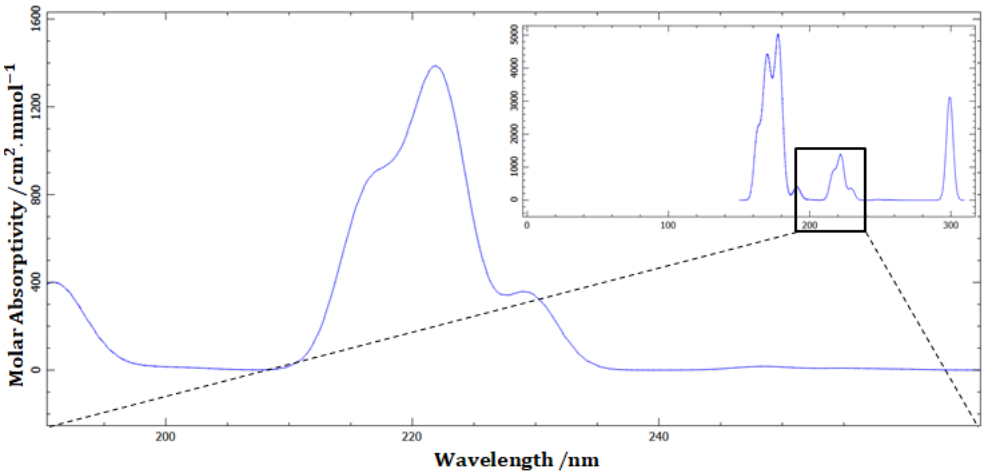


Figure 5.25: Theoretically predicted $UV_{vis}$ absorption spectrum of 3CTZ in methanol.

Table 5.9: Absorption data via transition electric dipole moment for 3CTZ in methanol.

| State | Energy/ $cm^{-1}$ | Wavelength/ nm | $f_{oscilator}$ | $M/(a.u)^2$ | $M_x/(a.u)$ | $M_y/(a.u)$ | $M_z/(a.u)$ |
|---|---|---|---|---|---|---|---|
| $S_1$ | 33347.7 | 299.9 | 0.6538500 | 6.45488 | -2.52732 | 0.12348 | -0.22870 |
| $S_5$ | 43597.6 | 229.4 | 0.070643455 | 0.53344 | 0.56474 | -0.45682 | -0.07627 |
| $S_6$ | 45026.8 | 222.1 | 0.2723798 | 1.99150 | 1.07938 | 0.86380 | 0.28334 |
| $S_7$ | 46184.8 | 216.5 | 0.163938046 | 1.16857 | 0.62754 | -0.87502 | -0.09542 |
| $S_{20}$ | 57678.9 | 173.4 | 0.711993328 | 4.06382 | 1.40830 | -1.20439 | -0.79370 |
| $S_{21}$ | 59101.0 | 169.2 | 0.446124954 | 2.48506 | 0.72936 | 0.90993 | -1.06072 |

### 5.3.2 Rate constants of ATZ, CTZ and 3CTZ

To ease the analysis of the emission spectra, one should first take a look at the rate constants associated with the radiative ($k_F, k_P$) and non-radiative ($k_{ISC}, k_{IC}, k_{RISC}$) phenomena a study the dynamics between them.

Before presenting the rate constant results it is important to recall that, unfortunately, the value of $k_{IC}$ was not computed with PIA due to its to the lack of theoretical derivation/implementation. All the necessary conversion factors and physical parameters used in the FSTF method can be consulted in the appendix chapter tables (A.4, A.5). Table (5.10) below presents the obtained rate constant results for ATZ. Looking at the obtained values, it is possible to see that, overall, PIA and FSTF methods present similar results. For instance, both methods lead to the conclusion that non-radiative processes dominate over the radiative ones which is in agreement with low obtained $k_F$ and $k_P$ values. To allow a more detailed discussion, table (5.11) presents the SOC values computed for ATZ.

Because of its intrinsic nature, ISC is mainly a spin-orbit coupling driven process meaning that low SOC values do not "lift" the spin-forbidden transition hence resulting in small $k_{ISC}$ rate constants. Commonly, this photophysical process possesses lifetimes around $10^{-10} - 10^{-8}$ s which would lead to rate constants in the range of $10^{10} - 10^{8}$ $s^{-1}$. Since phosphorescence is dependent on the $T_1$ state population, which grows with the increase of ISC rate constant, the low SOC also compromises the

Table 5.10: Computed radiative and non-radiative constants for ATZ in methanol at T = 298K resorting to PIA and FSTF methods.

| | **Rate constant** | **PIA** | **FSTF** |
|---|---|---|---|
| $S_1 \rightarrow T_1$ | $k_{\mathrm{ISC_S}}$ | $7.9708 \times 10^6$ s$^{-1}$ | $1.1 \times 10^6$ s$^{-1}$ |
| $T_1 \rightarrow S_1$ | $k_{\mathrm{RISC}}$ | $3.38 \times 10^6$ s$^{-1}$ | $7 \times 10^3$ s$^{-1}$ |
| $S_1 \rightarrow S_0$ | $k_{\mathrm{IC}}$ | $\cdots$ | $8.11 \times 10^3$ s$^{-1}$ |
| $S_1 \rightarrow S_0$ | $k_{\mathrm{F}}$ | 4.503 s$^{-1}$ | $5.5 \times 10^1$ s$^{-1}$ |
| $S_1 \rightarrow T_0$ | $k_{\mathrm{P}}$ | 3.35 s$^{-1}$ | $1.52 \times 10^1$ s$^{-1}$ |
| $T_1 \rightarrow S_0$ | $k_{\mathrm{ISC_T}}$ | $3.65 \times 10^8$ s$^{-1}$ | $2.08 \times 10^4$ s$^{-1}$ |

Table 5.11: Absolute values of ATZ SOCs (cm$^{-1}$) in methanol obtained at the TD-PBE0 cc-pVDZ level of theory.

| | $S_0$ **Geometry** | $S_1$ **Geometry** | $T_1$ **Geometry** |
|---|---|---|---|
| $\langle S_0 \vert H_{\mathrm{SOC}} \vert T_1^0 \rangle$ | 0.11 | 0.17 | 0.10 |
| $\langle S_0 \vert H_{\mathrm{SOC}} \vert T_1^{-1} \rangle$ | -0.33 | -0.05 | -0.02 |
| $\langle S_0 \vert H_{\mathrm{SOC}} \vert T_1^1 \rangle$ | 0.55 | 0.22 | 0.04 |
| $\sqrt{\sum_{\mathrm{MS}=0,\pm1} \vert \langle S_0 \vert H_{\mathrm{SOC}} \vert T_1^{\mathrm{Ms}} \rangle \vert^2}$ | 0.4934 | 0.2824 | 0.1095 |
| $\langle S_1 \vert H_{\mathrm{SOC}} \vert T_1^0 \rangle$ | 0.04 | 0.01 | 0.00 |
| $\langle S_1 \vert H_{\mathrm{SOC}} \vert T_1^{-1} \rangle$ | -0.03 | 0.01 | -0.02 |
| $\langle S_1 \vert H_{\mathrm{SOC}} \vert T_1^1 \rangle$ | -0.59 | -0.25 | 0.06 |
| $\sqrt{\sum_{\mathrm{MS}=0,\pm1} \vert \langle S_1 \vert H_{\mathrm{SOC}} \vert T_1^{\mathrm{Ms}} \rangle \vert^2}$ | 0.5921 | 0.2503 | 0.063 |

molecule's phosphorescent efficiency. Analysing the results from table (5.11), and combining them with table (5.10), it is possible to understand why ATZ's ISC related constants ($k_{\mathrm{ISC_S}}$,$k_{\mathrm{RISC}}$,$k_{\mathrm{ISC_T}}$ and $k_{\mathrm{P}}$) values are quite low. It is also possible to identify a discrepancy between PIA and FSTF $k_{\mathrm{ISC_T}}$ and $k_{\mathrm{RISC}}$ values which may be explained by the absence of vibronic effects in the FSTF method, since this is also a relevant effect in ISC. Nonetheless, particularly for $k_{\mathrm{RISC}}$, FSTF low value of the latter constant is in a better physical agreement with the previously discussed SOC results and the fact that RISC is a very temperature and spin-vibronic sensitive process[133], being a more relevant effect for higher temperatures. Combining both factors, the conclusion is that, at T = 298K, it becomes energetically more favorable the deactivation from $S_1$ to $T_1$ than the $T_1 - S_1$ excitation.

For a more complete photophysical perspective, let's now carry out an analysis of the competi-

tion amid the different processes. Analysing the results one can see that IC process dominates over fluorescence presenting a rate constant with a magnitude 3× bigger than $k_{\mathrm{F}}$. However, one would expect a higher rate constant value since this is a spin-allowed transition. Possibly, the large energy step between these two states (5 eV) and/ or the low vibronic couplings are enough to constrain this transition. For the $T_1 - S_0$ transition, the same type of dominance prevails with a phosphorescence rate constant with a magnitude 3× smaller than $k_{\mathrm{ISC_T}}$. Looking at the $\mathrm{SOC}_{\mathrm{T_1-S_0}}$ values one can easily justify the low magnitude of $k_{\mathrm{ISC_T}}$ obtained by FSTF. In PIA the obtained magnitude for $k_{\mathrm{ISC_T}}$ would require a much stronger $\mathrm{SOC}_{\mathrm{T_1-S_0}}$ value, which is not the case.

Comparing both fluorescence and phosphorescence, one can conclude that for ATZ the fluorescence is the dominant type of radiative deactivation mechanism in both methods. Unfortunately, due to the lack of experimental value for these constants, it is not possible to carry out an accuracy test between the two methods, hence a qualitative analysis will be done latter after the rate constants of the three tetrazolones are discussed.

Tables (5.12,5.13) below present the computed rate constants for CTZ with PIA and FSTF methods and the SOC values for the $S_0$, $S_1$ and $T_1$ geometries, respectively.

Table 5.12: Computed radiative and non-radiative constants for CTZ in methanol at T = 298K resorting to PIA and FSTF methods.

| | **Rate constant** | **PIA** | **FSTF** |
|---|---|---|---|
| $S_1 \rightarrow T_1$ | $k_{\mathrm{ISC_S}}$ | $7.9708 \times 10^7$ s$^{-1}$ | $9.41 \times 10^4$ s$^{-1}$ |
| $T_1 \rightarrow S_1$ | $k_{\mathrm{RISC}}$ | $9.16 \times 10^6$ s$^{-1}$ | $3.54 \times 10^7$ s$^{-1}$ |
| $S_1 \rightarrow S_0$ | $k_{\mathrm{IC}}$ | $\cdots$ | $7.16 \times 10^4$ s$^{-1}$ |
| $S_1 \rightarrow S_0$ | $k_{\mathrm{F}}$ | 2.30 s$^{-1}$ | $3.14 \times 10^1$ s$^{-1}$ |
| $S_1 \rightarrow T_0$ | $k_{\mathrm{P}}$ | $7.11 \times 10^1$ s$^{-1}$ | $1.48 \times 10^{-3}$ s$^{-1}$ |
| $T_1 \rightarrow S_0$ | $k_{\mathrm{ISC_T}}$ | $3.91 \times 10^4$ s$^{-1}$ | $8.16 \times 10^8$ s$^{-1}$ |

Starting with the analysis of the radiative deactivation mechanisms, one can see that PIA and FSTF allow to draw different conclusions. For instances, with PIA, CTZ presents a better phosphorescent behaviour than fluorescent but with FSTF one has the opposite conclusion. This difference may be explained by the low $M_{\mathrm{T_1-S_0}}$ values because, even though the SOC values for this transition are considerably high, within the FSTF method there is no direct dependency on the latter quantity but instead it depends on the the square of $M_{\mathrm{T_1-S_0}}$. With this, one concludes that PIA produced more physically accurate results for $k_{\mathrm{P}}$. Furthermore, this can also explain the dominance of $\mathrm{ISC}_{\mathrm{T_1-S_0}}$ over phosphorescence, since $k_{\mathrm{ISC_T}}$ increases with the squared value of SOC.

Still on the radiative processes, as expected, IC rules over fluorescence with a rate constant 4× bigger in magnitude than $k_{\mathrm{F}}$. Due to the nature of this electronic transition one would expect a higher IC rate constant, however a low vibronic couplings justifies the obtained magnitude. For PIA, it is not possible to do such analysis on $k_{\mathrm{ISC_T}}$ value since no theoretical derivation has been published

Table 5.13: Absolute values of CTZ SOCs ($cm^{-1}$) in methanol obtained at the TD-PBE0 cc-pVDZ level of theory.

| | $S_0$ **Geometry** | $S_1$ **Geometry** | $T_1$ **Geometry** |
|---|---|---|---|
| $\langle S_0 \vert H_{\mathrm{SOC}} \vert T_1^0 \rangle$ | 0.18 | -0.17 | -1.58 |
| $\langle S_0 \vert H_{\mathrm{SOC}} \vert T_1^{-1} \rangle$ | 0.12 | 0.05 | -13.15 |
| $\langle S_0 \vert H_{\mathrm{SOC}} \vert T_1^1 \rangle$ | 0.26 | 0.09 | -1.68 |
| $\sqrt{\sum_{\mathrm{MS}=0,\pm1} \vert \langle S_0 \vert H_{\mathrm{SOC}} \vert T_1^{\mathrm{Ms}} \rangle \vert^2}$ | 0.3382 | 0.1987 | 13.35 |
| $\langle S_1 \vert H_{\mathrm{SOC}} \vert T_1^0 \rangle$ | -0.02 | 0.01 | -0.05 |
| $\langle S_1 \vert H_{\mathrm{SOC}} \vert T_1^{-1} \rangle$ | -0.05 | -0.08 | 0.17 |
| $\langle S_1 \vert H_{\mathrm{SOC}} \vert T_1^1 \rangle$ | -0.47 | -0.11 | 2.64 |
| $\sqrt{\sum_{\mathrm{MS}=0,\pm1} \vert \langle S_1 \vert H_{\mathrm{SOC}} \vert T_1^{\mathrm{Ms}} \rangle \vert^2}$ | 0.4730 | 0.1363 | 2.6457 |

until this moment. Taking this into account, and considering the obtained SOC values for $T_1 - S_0$ transition, one concludes that the FSTF presents $k_{\mathrm{ISC_T}}$ results that are in more physical agreement with the computed SOC values.

Lastly, between ISC and RISC the results show that at T= 298 K for CTZ this competition may not be negligible. This comes as a surprise because, as previously mentioned, RISC is a very temperature sensitive mechanism and T = 298 K is not exactly a high temperature value. This competition can be explained by the considerable computed value of $\mathrm{SOC}_{\mathrm{T_1-S_1}}$ in the $T1$ geometry. Because, although the energy difference between $S_1$ and $T_1$ states is large (4 eV), the SOC seems to be strong enough to allow the competition between ISC and RISC at the studied temperature. Similarly to ATZ, in CTZ both PIA and FSTF allow to conclude that the non-radiative mechanisms dominate over the radiative ones.

Tables (5.14,5.15) below present the computed rate constants for 3CTZ with PIA and FSTF methods and the SOC values for the $S_0$, $S_1$ and $T_1$ geometries, respectively.

Overall, the results justifications and conclusions for 3CTZ are very similar to CTZ. Once again, both methods show a dominance of the non-radiative methods over the radiative ones. Regarding $\mathrm{ISC_S}$ and RISC competition, through PIA there is a clear dominance of $k_{\mathrm{ISC_S}}$ with a rate constant of magnitude 2× bigger than $k_{\mathrm{RISC}}$. On the other and, the high $\mathrm{k_{RISC}}$ value obtained with FSTF is in a better physical agreement with the strong $\mathrm{SOC}_{\mathrm{T_1-S_1}}$ obtained value in the $\mathrm{T_1}$ geometry.

Table 5.14: Computed radiative and non-radiative constants for 3CTZ in methanol at T = 298K resorting to PIA and FSTF methods.

| | **Rate constant** | **PIA** | **FSTF** |
|---|---|---|---|
| $S_1 \rightarrow T_1$ | $k_{\mathrm{ISC_S}}$ | $4.202 \times 10^6$ s$^{-1}$ | $1.52 \times 10^5$ s$^{-1}$ |
| $T_1 \rightarrow S_1$ | $k_{\mathrm{RISC}}$ | $4.44 \times 10^4$ s$^{-1}$ | $1.38 \times 10^8$ s$^{-1}$ |
| $S_1 \rightarrow S_0$ | $k_{\mathrm{IC}}$ | $\cdots$ | $1.42 \times 10^5$ s$^{-1}$ |
| $S_1 \rightarrow S_0$ | $k_{\mathrm{F}}$ | 5.742 s$^{-1}$ | $5.57 \times 10^1$ s$^{-1}$ |
| $S_1 \rightarrow T_0$ | $k_{\mathrm{P}}$ | 3.05 s$^{-1}$ | $4.7 \times 10^1$ s$^{-1}$ |
| $T_1 \rightarrow S_0$ | $k_{\mathrm{ISC_T}}$ | $1.1 \times 10^7$ s$^{-1}$ | $1.38 \times 10^8$ s$^{-1}$ |

Table 5.15: Absolute values of 3CTZ SOCs (cm$^{-1}$) in methanol obtained at the TD-PBE0 cc-pVDZ level of theory.

| | **$S_0$ Geometry** | **$S_1$ Geometry** | **$T_1$ Geometry** |
|---|---|---|---|
| $\langle S_0 \vert H_{\mathrm{SOC}} \vert T_1^0 \rangle$ | -0.15 | -0.07 | -0.46 |
| $\langle S_0 \vert H_{\mathrm{SOC}} \vert T_1^{-1} \rangle$ | 0.41 | 0.29 | -14.53 |
| $\langle S_0 \vert H_{\mathrm{SOC}} \vert T_1^1 \rangle$ | 0.67 | -0.10 | -1.78 |
| $\sqrt{\sum_{\mathrm{MS}=0,\pm1} \vert \langle S_0 \vert H_{\mathrm{SOC}} \vert T_1^{\mathrm{Ms}} \rangle \vert^2}$ | 0.7996 | 0.3146 | 13.65 |
| $\langle S_1 \vert H_{\mathrm{SOC}} \vert T_1^0 \rangle$ | 0.19 | -0.02 | -1.01 |
| $\langle S_1 \vert H_{\mathrm{SOC}} \vert T_1^{-1} \rangle$ | 0.10 | 0.04 | -0.08 |
| $\langle S_1 \vert H_{\mathrm{SOC}} \vert T_1^1 \rangle$ | -1.03 | 0.09 | 2.85 |
| $\sqrt{\sum_{\mathrm{MS}=0,\pm1} \vert \langle S_1 \vert H_{\mathrm{SOC}} \vert T_1^{\mathrm{Ms}} \rangle \vert^2}$ | 1.052 | 0.1004 | 3.024 |

Despite the strong coupling between $T_1$ and $S_0$ states, $\mathrm{ISC_T}$ process dominates the deactivation path between the latter electronic states. The same happens with fluorescence and IC. Nonetheless, regarding radiative processes, both methods allow the conclusion that fluorescence is the predominant one.

### 5.3.3 Emission behaviour of ATZ, CTZ and 3CTZ

Next in the photophysical analysis of tetrazolones is their emission behaviour. Figure (5.26) presents the theoretically predicted emission fluorescence spectrum of ATZ in methanol. The maximum is placed at 406 nm which corresponds to a displacement from the absorbance maximum of 182 nm. This difference between the maximums of absorption and emission is referred as *Stokes shift* and is

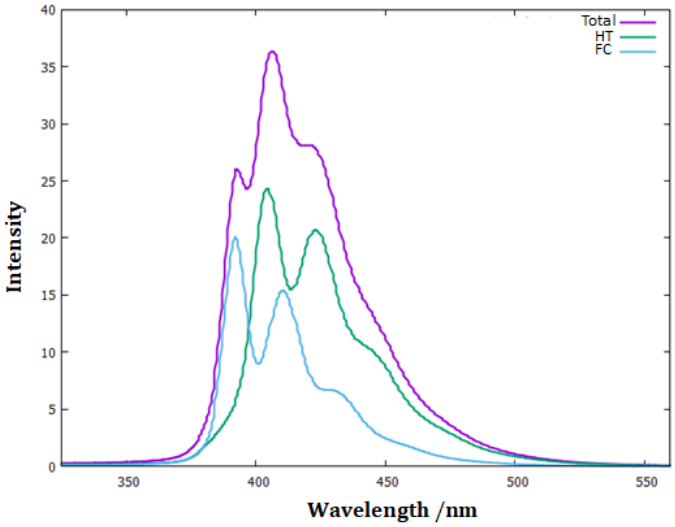


Figure 5.26: Theoretically predicted fluorescence spectrum of ATZ in methanol, purple line is the total intensity of emission, green line (HT) is the Herzberg-Teller contribution and blue line (FC) is the Franck-Condon contribution.

mainly caused by vibrational relaxation (conformational changes) and solvent reorganization. Since the calculations are done considering the solvent implicit (no reorganization takes place), the latter Stokes' dependency is negligible for this study. For ATZ, the Stokes shift is large meaning that possibly exists a considerable change in the molecule's conformation which consequently induces a change in the dipole moment after reaching the excited state. To corroborate this, the calculation of the dipole moment variation between states $S_0$ and $S_1$, was carried out resulting in a value of $\Delta\vec{\mu}_{\mathrm{ATZ,S_0-S_1}} = 0.140$ a.u. The latter is not a considerably high variation but can be enough to explain ATZ's red shift deviation. In fig (5.26), it is also possible to see that the Herzeberg-Teller coupling (green line) has the highest contribution to the total emission intensity. More precisely, the calculations show a HT contribution of 61% and 49% FC contribution. This behaviour demonstrates that the FC approximation is not enough, and that a nuclear dependency must be considered. This correction is expressed as an expansion of the transition dipole in terms of the nuclear coordinates[70],

$$\vec{M}_{if} = \vec{M}_0 + \sum_i \left(\frac{\partial \vec{M}}{\partial Q_i}\right)_{Q=0} Q_i + \cdots \tag{5.1}$$

the term with no nuclear dependency, $\vec{M}_0$, is the FC approximation, and the second one is the HT approximation corresponding to the lowest correction.

The low fluorescent rate constant of ATZ is related to the dominance of the IC process in this deactivation mechanism and also with the subsequent dominance of ISC. If ATZ was a more fluorescent molecule, its big Stokes shift would be useful for practical purposes since it would diminish self-quenching (processes that reduce fluorescence efficiency) that arises from possible molecular self-absorption [134].

The phosphorescence behaviour was also analysed, fig (5.27) presents the theoretically predicted

phosphorescence spectrum of ATZ in methanol. Similarly to the case of fluorescence, phosphorescence

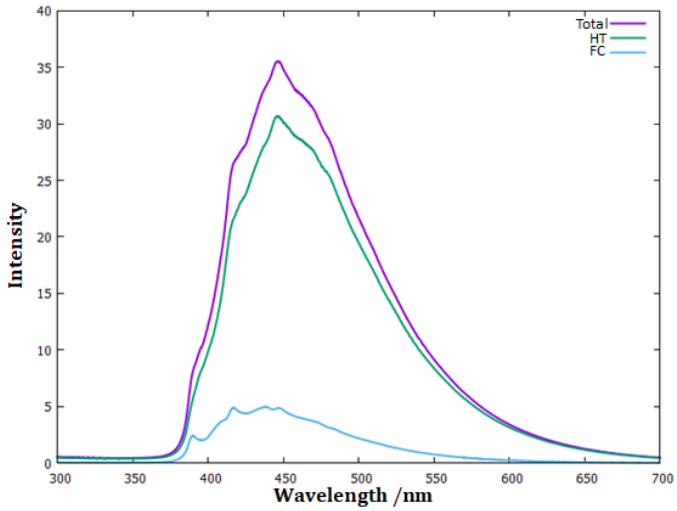


Figure 5.27: Theoretically predicted phosphorescence spectrum of ATZ in methanol, purple line is the total intensity of emission, green line (HT) is the Herzberg-Teller contribution and the blue line is the (FC) Franck-Condon contribution.

of ATZ is also primarily dominated by the HT contribution with a value of 84%. This behaviour is somehow expected since $T_1 - S_0$ transition is spin-forbidden thus being a very weakly dipole-allowed transition. Once again, HT approximation must be considered. The maximum of ATZ's phosphorescence is placed at 460 nm which corresponds to a Stokes shift of 236 nm.

The low phosphorescent rate constant of ATZ is explained by the dominance of $ISC_{T1} - S_0$ over the $T_1 \rightarrow S_0$ deactivation path.

Regarding CTZ fluorescent behaviour, fig (5.28) presents the theoretically predicted in methanol. Analysing the obtained results for CTZ's fluorescent emission, it is possible to conclude that, as it was for ATZ, this type of emission is ruled by he HT contribution with a value of 70%. Furthermore,

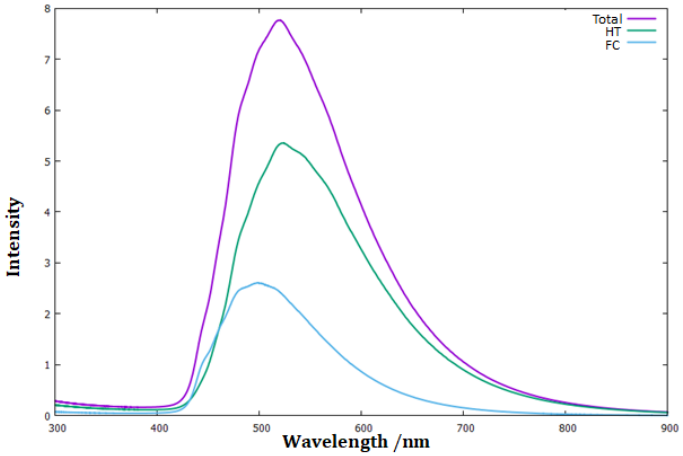


Figure 5.28: Theoretically predicted fluorescence spectrum of CTZ in methanol, purple line is the total intensity of emission, green line (HT) is the Herzberg-Teller contribution and the blue line is the (FC) Franck-Condon contribution.

for CTZ the maximum of emission is placed at 509 nm which corresponds to a Stokes shift of 286

nm a higher value than ATZ's. This red shift's increase is related to the dipole moment variation of CTZ,$\Delta\vec{\mu}_{\mathrm{CTZ,S_0-S_1}} = 0.3035$ a.u, which is bigger than ATZ's. If one compares ATZ and CTZ regarding their fluorescent behaviour, the previous rate constant results/conclusions show that, due to the low IC competition in ATZ, the latter is more fluorescent than CTZ. Regarding CTZ's phosphorescence, fig (5.29) shows the theoretically predicted spectrum in methanol.

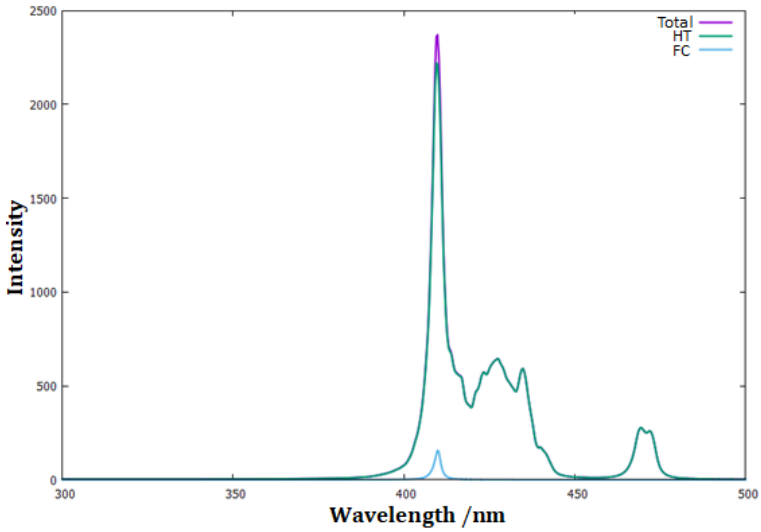


Figure 5.29: Theoretically predicted phosphorescence spectrum of CTZ in methanol, purple line is the total intensity of emission, green line (HT) is the Herzberg-Teller contribution and blue line (FC) is the Franck-Condon contribution.

Looking at the spectrum it is possible to see that once again HT is the main contribution to the total phosphorescence emission and that the maximum is located at 410 nm. The Stokes shift for CTZ's phosphorescence is 187 nm, which is less than ATZ's shift for the same type of emission, the reason for this being that there is a higher dipole moment change for ATZ in its triplet excited state, $\Delta\vec{\mu}_{\mathrm{ATZ,S_0-T_1}} = 0.528$ a.u, than for CTZ which is $\Delta\vec{\mu}_{\mathrm{CTZ,S_0-T_1}} = 0.2335$ a.u. With the previously drawn conclusions from the rate constants, and comparing both ATZ and CTZ phosphorescence, one can conclude that CTZ is a more phosphorescent tetrazolone.

Finally, and in order to finish the emission analysis, only the study of 3CTZ is needed. Figure (5.30) presents the theoretically predicted fluorescence spectrum for 3CTZ in methanol. Looking at the results it is possible to identify that the maximum is placed at 452 nm, which corresponds to a Stokes shift of 230 nm with a $\Delta\vec{\mu}_{\mathrm{3CTZ,S_0-S_1}}$ of 0.335 a.u.

Comparing with the other two tetrazolones, one understands why its Stokes shift is bigger than ATZ but, for CTZ, one would expect that 3CTZ presented the highest value due to the obtained $\Delta\vec{\mu}_{\mathrm{3CTZ,S_0-S_1}}$. Although that is true, it is possible that this discrepancy can be related to calculation errors since it is still in the uncertainty range of the 0.2 eV. Similarly to the other tetrazolones, HT contribution to the total emission is higher than FC, presenting a value of 79%. In comparison with the other tetrazolones, 3CTZ is the most fluorescent one due to its high $k_{\mathrm{F}}$ and $M_{\mathrm{S_1-S_0}}$ values.

Figure (5.31) shows the theoretically predicted phosphorescence spectrum of 3TCZ in methanol.

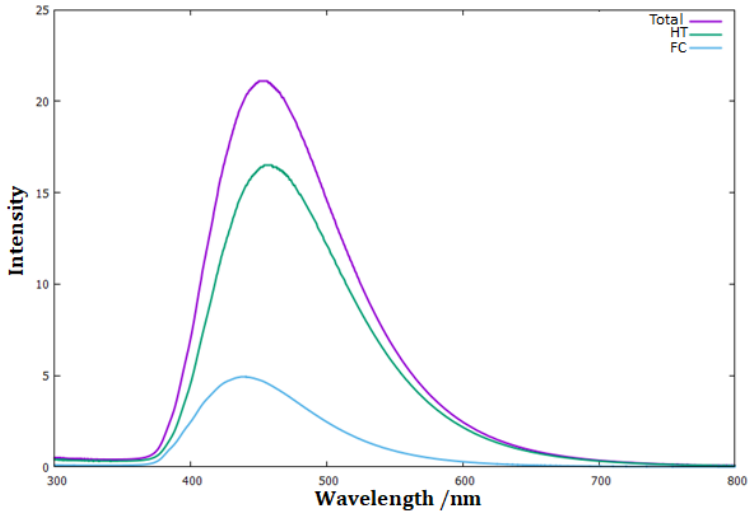


Figure 5.30: Theoretically predicted fluorescence spectrum of 3CTZ in methanol, purple line is the total intensity of emission, green line (HT) is the Herzberg-Teller contribution and blue line (FC) is the Franck-Condon contribution.

Regarding 3CTZ phosphorescence once again HT contribution dominates over FC, with a correspon-

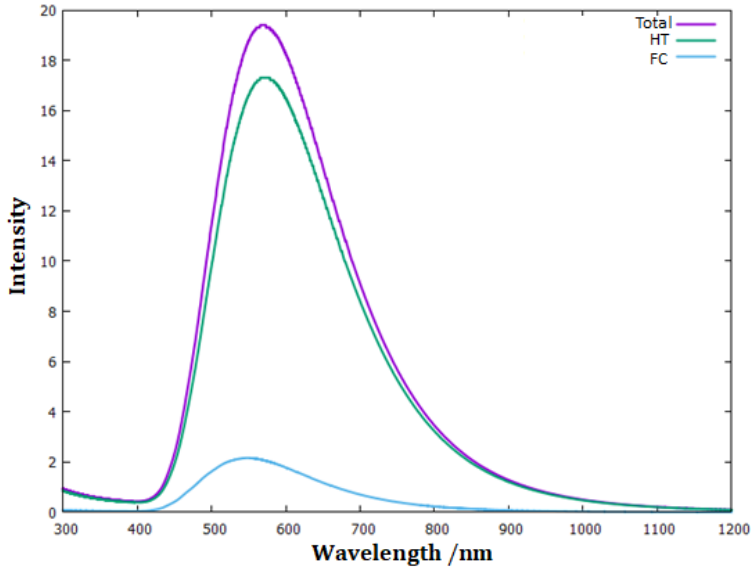


Figure 5.31: Theoretically predicted phosphorescence spectrum of 3CTZ in methanol, purple line is the total intensity of emission, green line (HT) is the Herzberg-Teller contribution and blue line (FC) is the Franck-Condon contribution.

dent percentage of 92 %. Its emission maximum is placed at 569 nm leading to a Stokes shift of 338 nm which is an extremely high value. Once again, one would expect that this would be the tetrazolone with the biggest $\Delta\vec{\mu}_{S_0-T_1}$ since it presents the biggest Stokes shift. The variation in the dipole moment for 3CTZ is $\Delta\vec{\mu}_{3CTZ,S_0-T_1} = 0.3015$ a.u while for ATZ is $\Delta\vec{\mu}_{ATZ,S_0-T_1} = 0.508$ a.u, this discrepancy can also be related to calculation errors since it is still in the uncertainty range of the 0.2 eV as it was also the case of 3CTZ's fluorescence.

Comparing with the results for the other two tetrazolones, 3CTZ is the second most phosphorescent

one. Overall the approached tetrazolones do not exhibit strong fluorescent and/or phosphorescent behaviour. The large Stokes shift values that were obtained are typical of molecules with small light emission efficiency.

### 5.3.4 PIA or FSTF?

As previously mentioned, an accuracy analysis of PIA and FSTF can not be carried out since there are no experimental values to compare with, although it is possible to compare them qualitatively. For the studied tetrazolones both methods allowed to conclude that the non-radiative deactivation mechanism are dominant over the radiative ones.

For ATZ, PIA and FSTF presented similar results for $k_{\mathrm{F}}, k_{\mathrm{P}}, k_{\mathrm{ISC}}$ but for $k_{\mathrm{RISC}}$ the latter method produced a rate constant value in more physical agreement with the obtained $\mathrm{SOC}_{\mathrm{S_1-T_1}}$ values. Regarding CTZ, both methods have similar results for $k_{\mathrm{RISC}}, k_{\mathrm{F}}$ but for $k_{\mathrm{P}}$ and $k_{\mathrm{ISC}}$ PIA yields results that physically represent well the computed $\mathrm{SOC}_{\mathrm{T_1-S_0}}$ values. For 3CTZ the main discrepancy was in the computation of $k_{RISC}$ where FSTF produced a rate constant value that is in more physical agreement with the $\mathrm{SOC}_{\mathrm{T_1-S_1}}$ .

One relevant aspect is that PIA considers the Duschinsky rotation effect, which helps to reproduce more reliable results for molecules with harsh geometry changes in the excited state. For the studied tetrazolones, this effect might be relevant if one takes into consideration the computed values of dipole moment $\mu_{\mathrm{S_1-S_0}}$ and $\mu_{\mathrm{T_1-S_0}}$ in the $\mathrm{UV_{vis}}$ absorption study. Besides, because PIA is coupled with ORCA it is very easy to carry on more detailed analysis as it was for the temperature dependence.

Also, for the computation of radiative rate constants in FSTF, particularly for phosphorescence, it would be interesting to introduce a $\mathrm{SOC}_{\mathrm{T_1-S_0}}$ dependency, since it is the main physical reason why this deactivation mechanism happens.

Although PIA is a more complex, computationally and time demanding method it easily allows the inclusion of vibronic effects (Herzberg-Teller, Jan-Teller) which one can not take into account for whit FSFT. The main advantage of FSTF really is in its light computation effort and low time consuming behaviour.

Considering the overall results, one concludes that the choice of method really depends on the extension of the analysis that is meant to carry on and the time and computational capacity available.

## 5.4 Photochemical pathway analysis of CTZ and 3CTZ

The primary goal of this thesis was to characterize the photophysical processes of ATZ, 3CTZ and CTZ through the computation of the rate constants and emission spectra. However, as described and presented in Chapter 1 with figs (1.7, 1.8), CTZ and 3CTZ possess two viable photochemical pathways after excitation. In order to proceed with the analysis let's take a step back and briefly recall CTZ

and 3CTZ possible photochemical pathways.

After photon absorption the latter undergoes $N_2$ photoextrusion a triplet birradical intermediate is formed. From here it is possible to follow one of two paths: intramolecular proton-transfer by the first unsaturated carbon of the cyclohexanyl or in the phenyl group.

To study the two possible ways of CTZ photochemical mechanism the Nudged Elastic Band (NEB) method was used. The latter is a computational tool to find the minimum energy track and the transition state (saddlepoint) between two minima[94]. NEB works similarly to a geometry optimization in the sense that in each cycle it optimizes the path in order to converge to the minimum energy path (MEP). Figure(5.32) below demonstrates the convergence behaviour of NEB for the first step of CTZ's photochemical pathway.

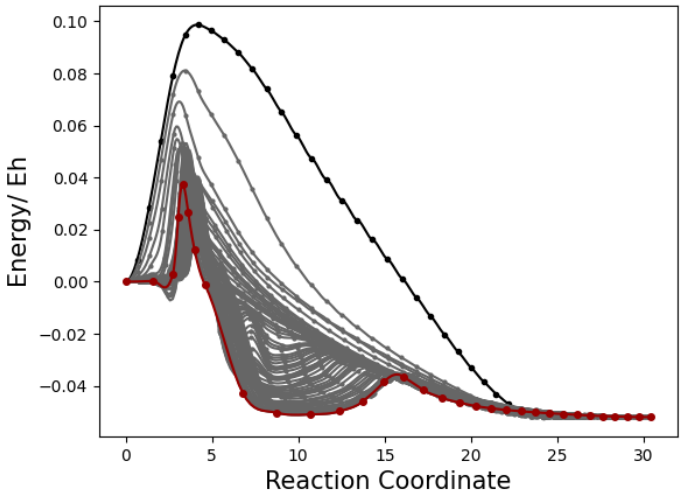


Figure 5.32: Example of NEB's convergence behaviour for the first step of CTZ's photochemical pathway (tetrazole's ring cleavage).

The black line was NEB's first guess to the path, then successively it started to minimize the energy of his guess (grey lines) until it reached the MEP which is represented by the red line. For the following energetical analysis only PIA method was considered since NEB was computed with the ORCA modules which has PIA implemented.

Figures (5.33, 5.35) present the main steps of the photochemical pathway of CTZ from the cyclohexanyl and the phenyl side and figs (5.34,5.36) represent the obtained MEP with NEB. The construction of the total MEP is done by gathering all the computed paths amid all the geometries presented in figs (5.33, 5.35). Furthermore, figs (5.37, 5.39) present the main steps of the photochemical pathway of 3CTZ from the cyclohexanyl and the phenyl side and figs (5.38,5.40) represent the obtained MEP with NEB.

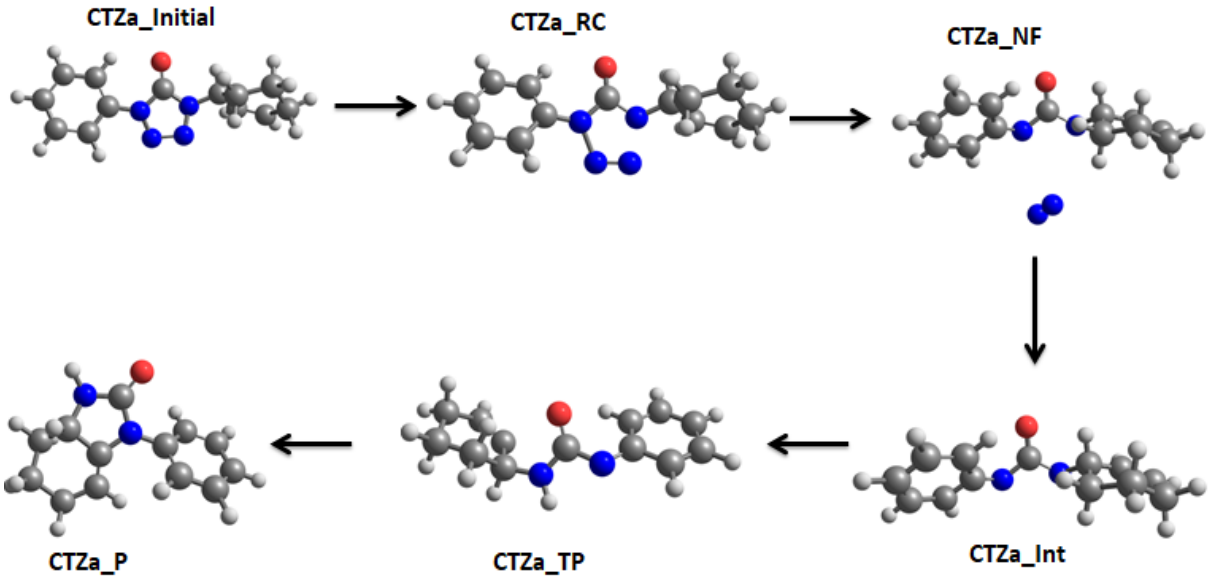


Figure 5.33: Schematic representation of CTZ's photochemical pathway for the cyclohexanyl group. CTZa-Initial corresponds to the initial triplet geometry, CTZa-RC is the geometry amid tetrazole's ring cleavage, CTZa-NF is related to the geometry when $N_2$ photoextrusion, CTZa-Int is the birradical triplet state and CTZa-TP and CTZa-P are the geometry of when proton-transfer takes place and the product in the triplet state, respectively.

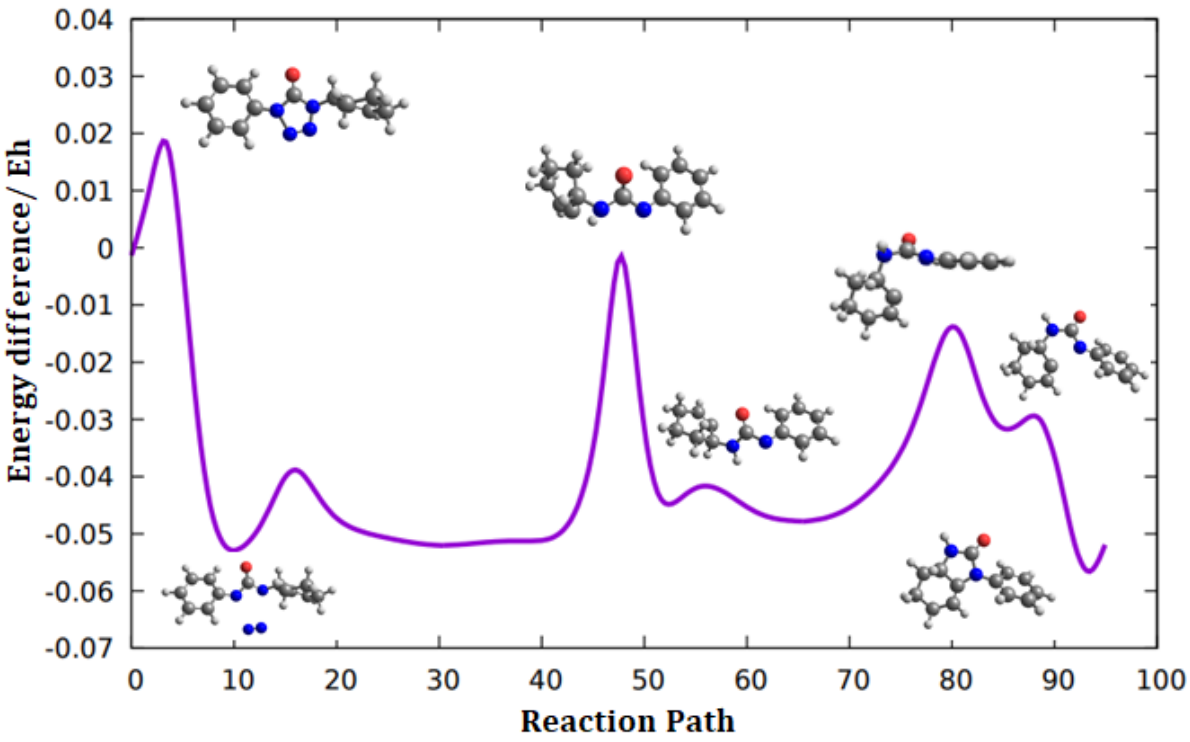


Figure 5.34: MEP obtained with NEB in methanol for CTZ by the cyclohexanyl path.

Looking at the obtained results one can see that, for CTZ, the intramolecular proton transfer by the phenyl path requires harsher geometry changes, specially from the triplet birradical intermediate to the proton transfer geometry. Regarding 3CTZ, the path from the proton transfer by the cylcohexanyl

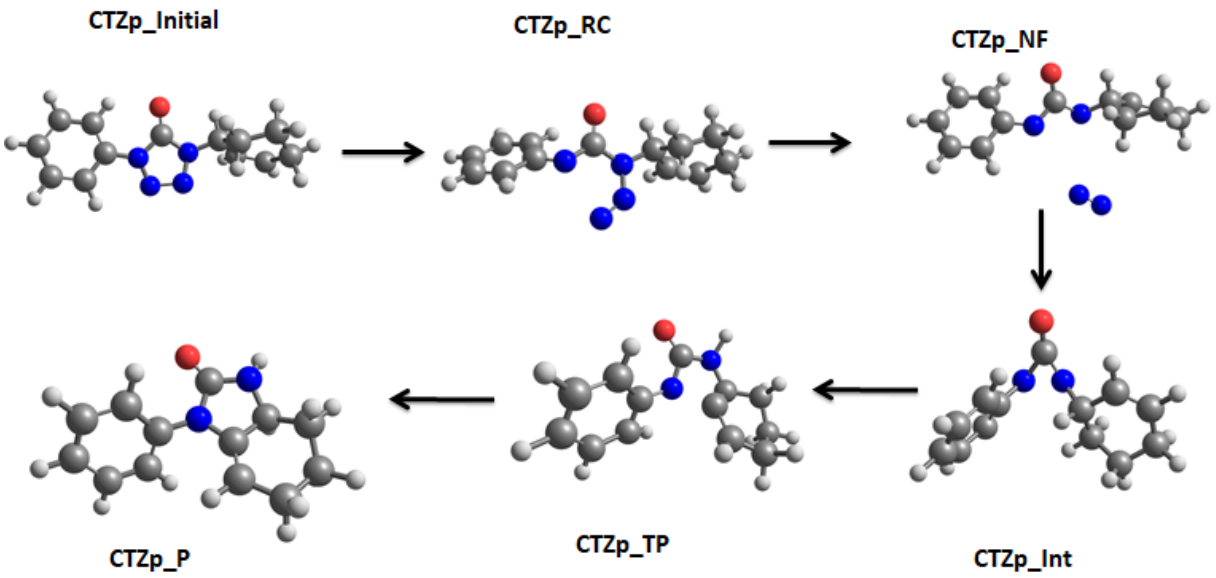


Figure 5.35: Schematic representation of CTZ's photochemical pathway for the phenyl group. CTZp-Initial corresponds to the initial triplet geometry, CTZp-RC is the geometry amid tetrazole's ring cleavage, CTZp-NF is related to the geometry when $N_2$ photoextrusion, CTZp-Int is the birradical triplet state and CTZp-TP and CTZp-P are the geometry of when proton-transfer takes place and the product in the triplet state, respectively.

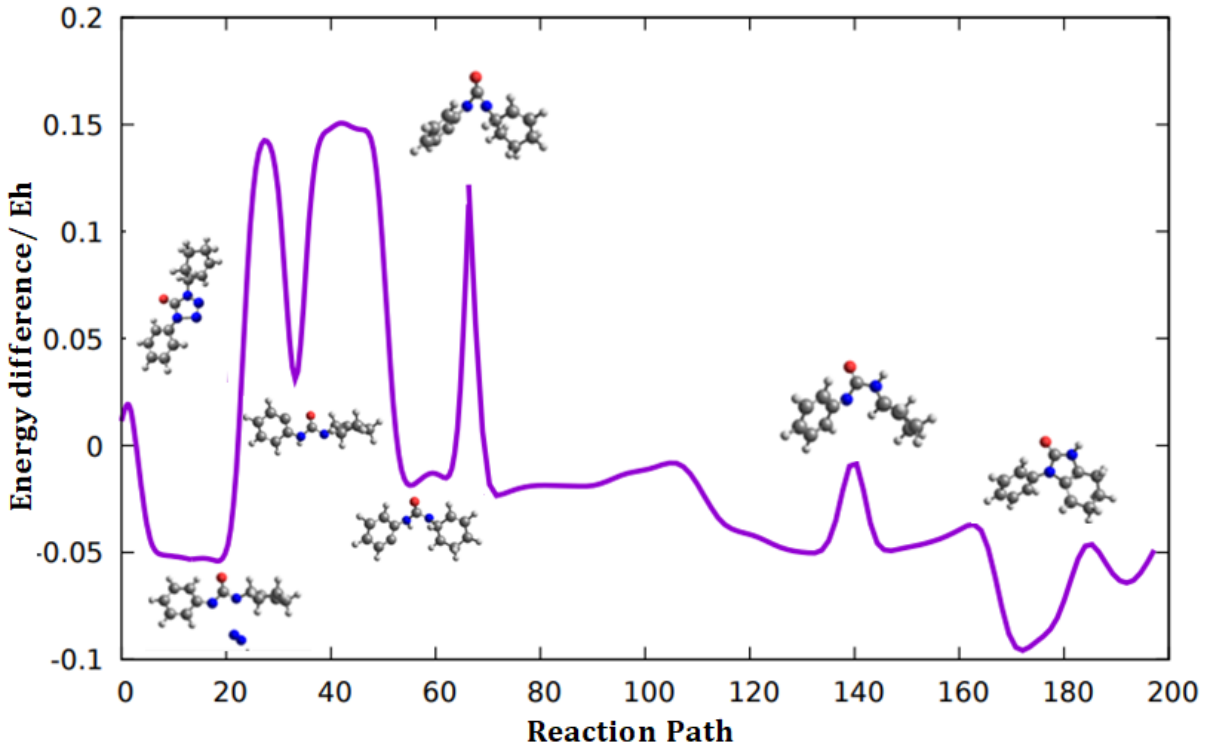


Figure 5.36: MEP obtained with NEB in methanol for CTZ by the phenyl path.

seems to need more conformational effort, specially in the transfer step. An energetic analysis is needed to confirm the latter arguments. Table (5.16) present the energy values for each geometry presented in figs (5.33, 5.35, 5.37, 5.39). Starting with CTZ, the computed energy values are in agreement

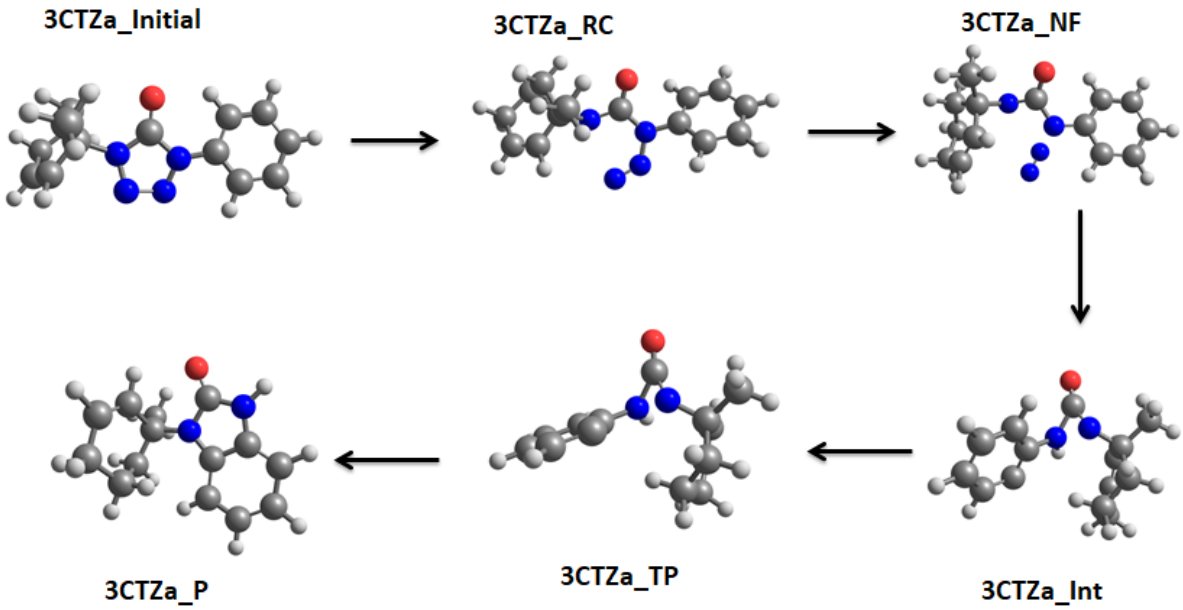


Figure 5.37: Schematic representation of 3CTZ's photochemical pathway by the cyclohexanyl group. 3CTZa-Initial corresponds to the initial triplet geometry, 3CTZa-RC is the geometry amid tetrazole's ring cleavage, 3CTZa-NF is related to the geometry when $N_2$ photoextrusion, 3CTZa-Int is the birradical triplet state and 3CTZa-TP and 3CTZa-P are the geometry of when proton-transfer takes place and the product in the triplet state, respectively.

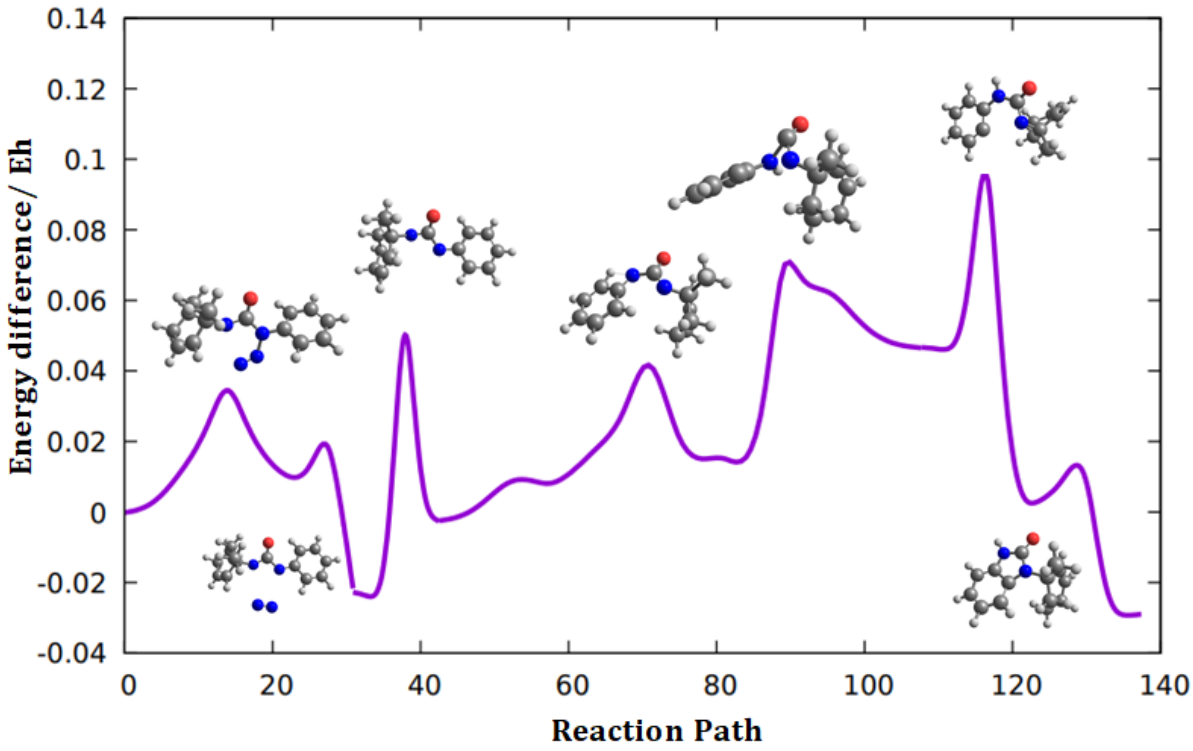


Figure 5.38: MEP obtained with NEB in methanol for 3CTZ by the cyclohexanyl path.

with the latter description, with CTZp-TP geometry possessing the highest energy value being the most unstable species in the path. Regarding the alternative pathway, although the energy difference

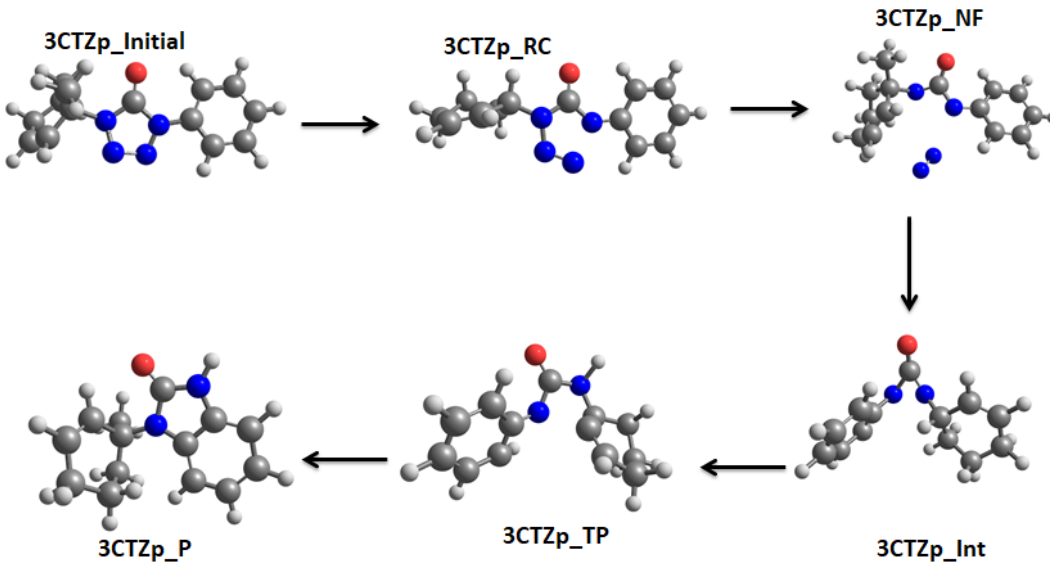


Figure 5.39: Schematic representation of 3CTZ's photochemical pathway by the phenyl group. 3CTZp-Initial corresponds to the initial triplet geometry, 3CTZp-RC is the geometry amid tetrazole's ring cleavage, 3CTZp-NF is related to the geometry when $N_2$ photoextrusion, 3CTZp-Int is the birradical triplet state and 3CTZp-TP and 3CTZp-P are the geometry of when proton-transfer takes place and the product in the triplet state, respectively.

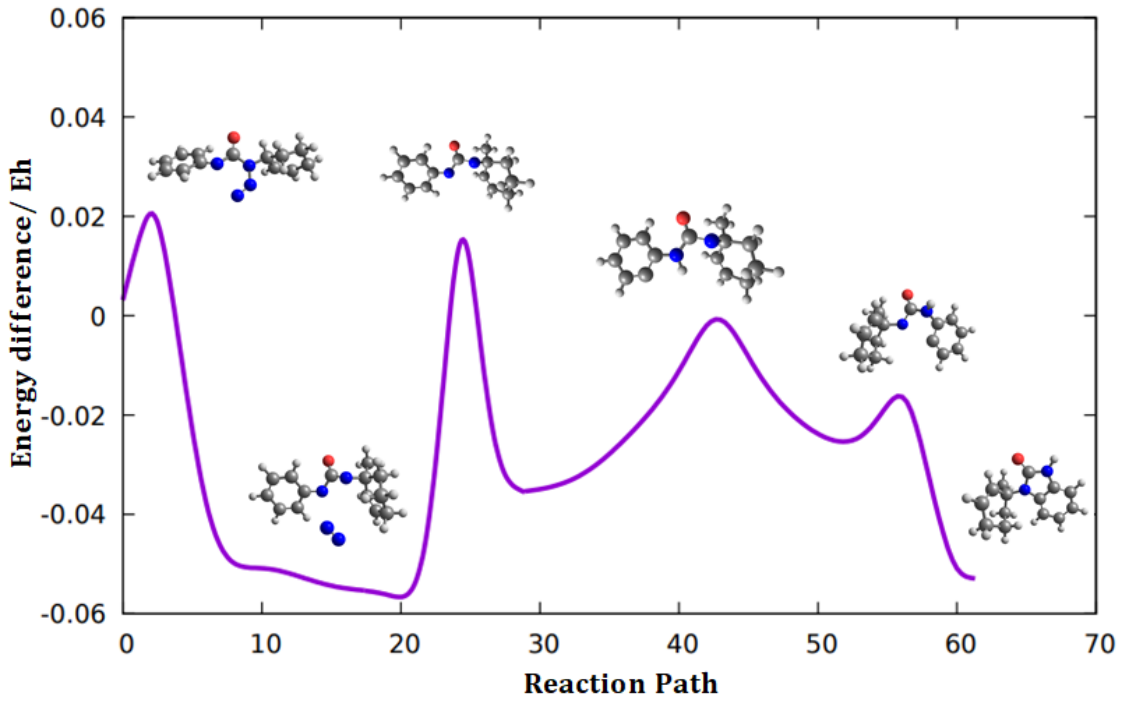


Figure 5.40: MEP obtained with NEB in methanol for 3CTZ by the phenyl path.

is small, in fact it is the least energetically demanding path, possessing more stable species along the way and producing the most energetically stable product. Regarding 3CTZ, the geometry after proton transfer in both paths is the least stable species, presenting the highest electronic energy value. Although both paths possess similar energy values, the proton transfer by the phenyl group produces

Table 5.16: Energy (Eh) values for CTZ and 3CTZ main steps by the cyclohexanyl and phenyl groups photochemical pathways.

| | **Energy/ Eh** | | **Energy/ Eh** |
|---|---|---|---|
| CTZa – Initial | -797.061 | 3CTZa – Initial | -836.314 |
| CTZa – RC | -797.049 | 3CTZa – RC | -836.260 |
| CTZa – NF | -797.11 | 3CTZa – NF | -836.38 |
| CTZa – Int | -682.62 | 3CTZa – Int | -726.968 |
| CTZa – TP | -687.603 | 3CTZa – TP | -726.945 |
| CTZa – P | -687.779 | 3CTZa – P | -726.973 |
| CTZp – Initial | -797.061 | 3CTZp – Initial | -836.326 |
| CTZp – RC | -796.979 | 3CTZp – RC | -836.26 |
| CTZp – NF | -797.077 | 3CTZp – NF | -836.381 |
| CTZp – Int | -687.520 | 3CTZp – Int | -726.968 |
| CTZp – TP | -687.347 | 3CTZp – TP | -726.945 |
| CTZp – P | -687.696 | 3CTZp – P | -727.10 |

the most energetically stable product.

## 5.5 Polarizability in photochemical path selectivity

Based on the conclusions from the work of Pearson[79], Fuentealba and Reyes[77, 80] and Ghanty and Ghosh[81], the polarizability values of the products from both pathways were studied in order to try to understand which path would produce the more stable product and, if possible, corroborate the previous arguments from the energy analysis. Table (5.17) presents the computed polarizability values in methanol for CTZa-P and CTZp-P.

Table 5.17: Polarizability and energy values in methanol at T = 298K for CTZ and 3CTZ produtcs by the cyclohexanyl and phenyl groups photochemical pathways.

| | $\alpha$/ **(a.u)** | **Energy/ Eh** |
|---|---|---|
| CTZa – P | 283 | -687.779 |
| CTZp – P | 284 | -687.696 |
| 3CTZa – P | 251 | -726.972 |
| 3CTZp – P | 250 | -727.103 |

Because the $\eta$ is inversely proportional to $\left(\sqrt[3]{1/\alpha}\right)$[77, 80], and considering that the higher the hardness the less reactive the species is, one can conclude that CTZa-P is harder than CTZp-P, thus possessing lower reactivity being more stable. Putting together the energetic and polarizability analysis one can conclude that the intramolecular proton transfer pathway via cyclohexanyl group is the most probable to take place since its product is the most stable.

Regarding 3CTZ, the same analysis was carried out for both pathways and looking at the results

in table (5.17) indeed the most energetically stable product is also the hardest one possessing the lowest polarizability from the two. With this, one can conclude that for 3CTZ the most probable path would be the proton transfer by the phenyl group.

### 5.5.1 Excited triplet state product stability

Considering the latter conclusions regarding the choice of the photochemical path based on energetic and polarizability analysis a last photophysical process was analysed, the deactivation of the product from the triplet state. This calculation was only carried out with PIA since all the above analysis was carried out with ORCA, the results are presented below in table (5.18).

Table 5.18: Computed $k_{\mathrm{ISC_T}}$ rate constants with PIA for CTZ and 3CTZ in methanol at $T = 298$ K.

| | $k_{\mathrm{ISC_T}}$ | $k_{\mathrm{P}}$ |
|---|---|---|
| $\mathrm{CTZp} - \mathrm{P}$ | $1.82 \times 10^{7}\ \mathrm{s}^{-1}$ | $9.45\ \mathrm{s}^{-1}$ |
| $\mathrm{3CTZ_a} - \mathrm{P}$ | $1.99 \times 10^{13}\ \mathrm{s}^{-1}$ | $6.75\ \mathrm{s}^{-1}$ |

Looking at the results, one can conclude that both products will eventually decay to the ground state by means of a non-radiative mechanism.

## 5.6 Solvent effect on polarizability and CTZ and 3CTZ selectivity

Research has shown that there is an increase of the reactivity of a molecular system with the increase of solvent's polarity, i.e higher dielectric constant [135]. The latter can be seen as the ability that the solvent has to enclose charges from each other. A solvent that possesses a high dielectric constant can better stabilize the charges[135]. Regarding polarizability, because there is an increase in the molecule's reactivity, its polarizability is also expected to increase.

With this in mind, a brief study on the effect of solvent polarity in polarizability was carried out to try to understand if in other protic solvents the chosen photochemical pathway would still be the same as in methanol. This evaluation was done only for other protic solvents because that is the type of solvent where the mechanisms from figs (1.6, 1.7,1.8) are proposed. For this test, water was the chosen solvent with higher dielectric constant and ammonia with the lower dielectric constant than methanol. A new optimization of the product's geometry from CTZ and 3CTZ photochemical pathways was carried out in water and ammonia.

Looking at the results, shown in table(5.19), it is possible to conclude that with the increase of the solvent's polarity, in fact, there is an increase in the product's polarizability.

Table 5.19: Polarizability values for CTZ and 3CTZ products by the cyclohexanyl and phenyl paths in water, ammonia and methanol at T = 298K.

| | **Solvent** | $\alpha$/ **(a.u)** | $\varepsilon/(\mathrm{F.m^{-1}})$ |
|---|---|---|---|
| CTZa − P | Water | 286.56 | 80.4 |
| CTZa − P | Methanol | 283 | 32.63 |
| CTZa − P | Ammonia | 280.11 | 22.4 |
| CTZp − P | Water | 287.16 | 80.4 |
| CTZp − P | Methanol | 284 | 32.63 |
| CTZp − P | Ammonia | 280.31 | 22.4 |
| 3CTZa − P | Water | 253.1 | 80.4 |
| 3CTZa − P | Methanol | 251 | 32.63 |
| 3CTZa − P | Ammonia | 250.07 | 22.4 |
| 3CTZp − P | Water | 253 | 80.4 |
| 3CTZp − P | Methanol | 250 | 32.63 |
| 3CTZp − P | Ammonia | 248.77 | 22.4 |

For water one concludes that in the 3CTZ photochemical pathway the intramolecular proton transfer by the phenyl group still produces the most stable product. The same conclusion can be drawn for ammonia. Regarding CTZ, in the three studied solvents CTZa-P is the product with the lowest reactivity, which leads to the conclusion that for CTZ the intramolecular proton transfer mechanism is more probable to take place by the cyclohexanyl group.

# Chapter 6

# Conclusions and Future Perspectives

The vibrational analysis of ATZ, CTZ and 3CTZ in methanol allowed the identification of three characteristic peaks among the different addressed tetrazolones: 1800 $cm^{-1}$ elongation of the C=O bond from the carbonyl group; 1500 $cm^{-1}$ corresponding to the phenyl group and 1530 $cm^{-1}$ for the elongation of the N=N bond from the tetrazole ring.

Regarding the $UV_{vis}$ absorption, overall, a good replication of the experimental results was achieved with an average error of 10 %. It was also possible to conclude that, in the range of the experimental data, the transition $S_0 - S_6$ is responsible for the detected maximum around $\approx$ 224 nm, in the experimental region, across the three studied tetrazolones.

The photophysical characterization of ATZ, CTZ and 3CTZ processes, with PIA and FSTF methods, showed that 3CTZ is the most fluorescent tetrazolone with a value of $k_F = 5.742\ s^{-1}$ (PIA) and $k_F = 5.57 \times 10^1\ s^{-1}$ (FSTF) and that CTZ possesses the highest phosphorescent capacity with a value of $k_P = 7.11 \times 10^1\ s^{-1}$. It was interesting to see that in CTZ and 3CTZ, at the studied temperature of $T = 298$ K, the ISC-RISC competition might not be negligible. Hence, a further temperature dependence study could also become relevant to test the range of temperatures where this competition is indisputably relevant.

The emission spectral results also allowed the conclusion that the FC approximation is not enough to describe these three particular systems due to the average HT contribution of 84% to the total emission intensity. In a general way, the calculated Stokes shift were considerably large which is in agreement with the approached tetrazolones' low fluorescent and phosphorescent rate constants. Overall, PIA and FSTF methods yielded similar results being the choice of using one or another dependent on the extent of the analysis that is meant to carry out and computational/time availability. PIA, although more complex, allows a better inclusion of a vast variety of effects such as vibronic (Jan-Teller, Herzberg-Teller) and different solvent characteristics. Possibly in the future with experimental results it will be possible to carry out an accuracy analysis on both methods, to produce a more precise comparison.

Due to the possibility of existence of two photochemical pathways in 3CTZ and CTZ after $N_2$ photo-extrusion, an energetic analysis of both paths was carried out using NEB to study the possibility of occurrence of each path. The results show that for CTZ the path by the cyclohexanyl group possesses the more energetically stable species, but more importantly the most stable product with an electronic energy of $E_{CTZa-P} = -687.78$ Eh. Regarding 3CTZ, although the energy values of the evaluated geometries were similar, the path with intramolecular proton transfer by the phenyl group produced the most stable product with an energy value of $E_{3CTZp-P} = 727.10$ Eh. One of the goals of this thesis was also to test if the molecular polarizability could be used as a "marker" for selectivity in photochemical pathways based on the knowledge that molecular systems with higher hardness, i.e lower polarizability, are less reactive and hence more stable. The polarizability of each product from CTZ and 3CTZ possible pathways after $N_2$ photo-extrusion were calculated and, in the end, one can conclude that the polarizability analysis is in agreement with the results from the energetical analysis with CTZa-P and 3CTZp-P being the products with lower polarizability thus more stable and probable to be formed. In the future, it would be interesting to carry out molecular dynamics simulations to understand if the presence of the methyl group in 3CTZ can contribute to the chosen path. Because the latter study allows the inclusion of the solvent explicitly it could also provide more detailed information of the effect of the solvent in the conformational changes of 3CTZ during the photochemical pathway.

The effect of solvent polarity showed that with an increase of the solvent's dielectric constant there is an increase in the molecules polarizability leading to a higher molecular reactivity. Ammonia was chosen as the solvent with lower dielectric constant than methanol and water as possessing a higher dielectric constant. With this study it was possible to conclude that even for solvents with harsh differences in their polarity, the most probable product to be formed still is the 3CTZp-P by the intramolecular proton transfer by the phenyl group in 3CTZ photochemical pathway, and CTZa-P from the intramolecular proton transfer by the cyclohexanyl group.

# Contributions

I Tânia Patrícia Almeida Sousa, here declare that I have fully written and perform the research behind this thesis.

In addition, I also declare that this work has not yet been previously submitted, as a whole or in part, to obtain another graduation level. This work was funded by the Portuguese Science Foundation ("Fundação para a Ciência e a Tecnologia" - FCT)– Projects UIDB/00313/2020 and UIDP/00313/2020 (National Funds).

# Outcomes

During my master's thesis I published an article in the Redox Biology Jornal: Tânia Sousa, Marcos Gouveia, Rui D.M. Travasso, Armindo Salvador, "*How abundant are superoxide and hydrogen peroxide in the vasculature lumen, how far can they reach?*",Volume 58, 2022 , 102527, ISSN 2213-2317, https://doi.org/10.1016/j.redox.2022.102527.

Moreover, based and during the work on this thesis, an article was written (to be submitted) entitled "*Characterization of the photophysical processes of 1-phenyl-4-allyl-tetrazol-5-one.*"

Furthermore, it is also intended to write another article regarding the selectivity of the two possible photochemical paths for the intramolecular proton transfer in 1-phenyl-4-ciclohexanyl- tetrazol-5-one (CTZ) and 1-phenyl-4-(3-methyl–cylohexanyl)-tetrazol-5-one (3CTZ).

# Bibliography


[1] Rostislav Trifonov and V. Ostrovskii. "Protolytic Equilibria in Tetrazoles". In: *ChemInform* 42 (Nov. 2006), pp. 1585–1605. DOI: 10.1134/S1070428006110017.

[2] Vitaly G. Kiselev, Pavel B. Cheblakov, and Nina P. Gritsan. "Tautomerism and Thermal Decomposition of Tetrazole: High-Level Ab Initio Study". In: *The Journal of Physical Chemistry A* 115.9 (Mar. 2011), pp. 1743–1753. ISSN: 1089-5639. DOI: 10.1021/jp112374t. (Visited on 07/07/2023).

[3] Joseph S. Mihina and Robert M. Herbest. "The reaction of nitriles with hydrazoic acid: synthesis of monosubstituted tetrazoles". In: *The Journal of Organic Chemistry* 15.5 (Sept. 1950), pp. 1082–1092. ISSN: 0022-3263. DOI: 10.1021/jo01151a027. (Visited on 07/07/2023).

[4] Anna Rażyńska et al. "Application of Mass Spectrometry to the Study of Prototropic Equilibria in 5-Substituted Tetrazoles in the Gas Phase; Experimental Evidence and Theoretical Considerations". In: *Journal of the Chemical Society, Perkin Transactions 2* 3 (Jan. 1983), pp. 379–383. ISSN: 1364-5471. DOI: 10.1039/P29830000379. (Visited on 07/07/2023).

[5] R. E. Trifonov and V. A. Ostrovskii. "Basicity of Phenyl-Substituted 1,3-Oxazoles". In: *Russian Journal of Organic Chemistry* 37.3 (Mar. 2001), pp. 416–420. ISSN: 1608-3393. DOI: 10.1023/A:1012496827820. (Visited on 07/07/2023).

[6] G. I. Koldobskii, V. A. Ostrovskii, and B. V. Gidaspov. "Tautomerism and Acid-Base Properties of Tetrazoles (Review)". In: *Chemistry of Heterocyclic Compounds* 16.7 (July 1980), pp. 665–674. ISSN: 1573-8353. DOI: 10.1007/BF00557732. (Visited on 07/07/2023).

[7] Kiyokazu Fuke and Koji Kaya. "Dynamics of Double-Proton-Transfer Reaction in the Excited-State Model Hydrogen-Bonded Base Pairs". In: *The Journal of Physical Chem-*

*istry* 93.2 (Jan. 1989), pp. 614–621. ISSN: 0022-3654. DOI: 10.1021/j100339a023. (Visited on 07/07/2023).

[8] Otilia Mó. "Protonation Energies and Tautomerism of Azoles. Basis Set Effects". In: *The Journal of Physical Chemistry* (Jan. 1986). (Visited on 07/07/2023).

[9] V Michon et al. "Preparation, Structural Analysis and Anticonvulsant Activity of 3- and 5-Aminopyrazole N-benzoyl Derivatives". In: *European Journal of Medicinal Chemistry* 30.2 (Jan. 1995), pp. 147–155. ISSN: 0223-5234. DOI: 10.1016/0223-5234(96)88220-1. (Visited on 07/07/2023).

[10] Curt Wentrup. "Tautomeric Equilibrium and Hydrogen Shifts of Tetrazole in the Gas Phase and in Solution". In: *Journal of The American Chemical Society* (Jan. 1993). (Visited on 07/07/2023).

[11] Rui Montenegro Val-do-Rio Pinto. "Photoelectron Spectroscopy of Nitrogen Containing Molecules of Biological and Industrial Interest". PhD thesis. Faculdade de Ciências e Tecnologia da Universidade Nova de Lisboa, 2011.

[12] Susana C. S. Bugalho et al. "Low Temperature Matrix-Isolation and Solid State Vibrational Spectra of Tetrazole". In: *Physical Chemistry Chemical Physics* 3.17 (Jan. 2001), pp. 3541–3547. ISSN: 1463-9084. DOI: 10.1039/B103344C. (Visited on 07/07/2023).

[13] A. P Mazurek and N Sadlej-Sosnowska. "Studies on Tautomerism in Tetrazole: Comparison of Hartree–Fock and Density Functional Theory Quantum Chemical Methods". In: *Chemical Physics Letters* 330.1 (Nov. 2000), pp. 212–218. ISSN: 0009-2614. DOI: 10.1016/S0009-2614(00)01060-5. (Visited on 07/07/2023).

[14] Halina Szatylowicz, Anna Jezuita, and Tadeusz M. Krygowski. "On the Relations between Aromaticity and Substituent Effect". In: *Structural Chemistry* 30.5 (Oct. 2019), pp. 1529–1548. ISSN: 1572-9001. DOI: 10.1007/s11224-019-01360-7. (Visited on 07/07/2023).

[15] *Tautomeric Equilibrium and Hydrogen Shifts of Tetrazole in the Gas Phase and in Solution | Journal of the American Chemical Society*. DOI: 10.1021/ja00059a048. (Visited on 07/07/2023).

[16] R. Jason Herr. "5-Substituted-1H-tetrazoles as Carboxylic Acid Isosteres: Medicinal Chemistry and Synthetic Methods". In: *Bioorganic & Medicinal Chemistry* 10.11 (Nov. 2002), pp. 3379–3393. ISSN: 0968-0896. DOI: 10.1016/s0968-0896(02)00239-0.

[17] Maqsood Malik et al. "ChemInform Abstract: Tetrazoles as Carboxylic Acid Isosteres: Chemistry and Biology". In: *Journal of inclusion phenomena and macrocyclic chemistry* 78 (May 2013). DOI: 10.1007/s10847-013-0334-x.

[18] US EPA National Center for Environmental Assessment. *New Energetic Materials: Functionalized 1-Ethyl-5-Aminotetrazoles and 1-Ethyl-5-Nitriminotetrazoles*. WEB SITE. Mar. 2009. (Visited on 07/07/2023).

[19] Thomas M. Klapötke et al. "1,5-Diamino-4-methyltetrazolium Dinitramide". In: *Journal of the American Chemical Society* 127.7 (Feb. 2005), pp. 2032–2033. ISSN: 0002-7863. DOI: 10.1021/ja042596m. (Visited on 07/07/2023).

[20] Rajendra P. Singh et al. "Nitrogen-Rich Heterocycles". In: *High Energy Density Materials*. Ed. by T. M. Klapötke. Structure and Bonding. Berlin, Heidelberg: Springer, 2007, pp. 35–83. ISBN: 978-3-540-72202-1. DOI: 10.1007/430_2006_055. (Visited on 07/07/2023).

[21] Elena Aleksandrovna Popova, Rostislav E. Trifonov, and Vladimir A. Ostrovskii. "Advances in Synthesis of Tetrazoles Coordinated to Metal Ions". In: *Arkivoc* 2012.1 (Nov. 2011). Ed. by Viktor V. Zhdankin, pp. 45–65. ISSN: 1551-7012. DOI: 10.3998/ark.5550190.0013.102.

[22] Guillem Aromí et al. "Triazoles and Tetrazoles: Prime Ligands to Generate Remarkable Coordination Materials". In: *Coordination Chemistry Reviews* 255.5 (Mar. 2011), pp. 485–546. ISSN: 0010-8545. DOI: 10.1016/j.ccr.2010.10.038. (Visited on 07/07/2023).

[23] *3D Framework Containing Cu4Br4 Cubane as Connecting Node with Strong Ferroelectricity | Journal of the American Chemical Society*. DOI: 10.1021/ja803021v. (Visited on 07/07/2023).

[24] Kandasamy Ponnuvel, Vediappen Padmini, and sri balan Rajendran. "A New Tetrazole Based Turn-on Fluorescence Chemosensor for Zn2+ Ions and Its Application in Bioimaging". In: *Sensors and Actuators, B: Chemical* 222 (Jan. 2016), pp. 605–611. DOI: 10.1016/j.snb.2015.08.096.

[25] Zhengqiu Li et al. "Tetrazole Photoclick Chemistry: Reinvestigating Its Suitability as a Bioorthogonal Reaction and Potential Applications". In: *Angewandte Chemie (In-*

*ternational Ed. in English)* 55.6 (Feb. 2016), pp. 2002–2006. ISSN: 1521-3773. DOI: 10.1002/anie.201508104.

[26] Yi Li and Ming-Hua Xu. "Rhodium-Catalyzed Asymmetric Tandem Cyclization for Efficient and Rapid Access to Underexplored Heterocyclic Tertiary Allylic Alcohols Containing a Tetrasubstituted Olefin". In: *Organic Letters* 16.10 (May 2014), pp. 2712–2715. ISSN: 1523-7060. DOI: 10.1021/ol500993h. (Visited on 07/07/2023).

[27] Mariyam Mariyam and Siska Oktapianti. "Synthesis, Characterization and Antimicrobial Evaluation of Novel 1-[(1-Phenyl-1h-Tetrazol-5-yl-imino)-Methyl]-Naphthalen-2-ol and Its Cu(II), Co(II) Complexes". In: *Oriental Journal of Chemistry* 34 (June 2018), pp. 1541–1550. DOI: 10.13005/ojc/340346.

[28] Martin Backor and D. Fahselt. "Tetrazolium Reduction as an Indicator of Environmental Stress in Lichens and Isolated Bionts". In: *Environmental and Experimental Botany* 53 (Apr. 2005), pp. 125–133. DOI: 10.1016/j.envexpbot.2004.03.007.

[29] Amin Lopes Ismael. *"Structure and reactivity of novel tetrazolesaccharinates useful as multidentate nitrogen ligands"*. 2017.

[30] A Rajasekaran and PP Thampi. "Synthesis and antinociceptive activity of some substituted-{5-[2-(1,2,3,4-tetrahydrocarbazol-9-yl)ethyl]tetrazol-1-yl}alkanones." In: *European journal of medicinal chemistry* 40.12 (Dec. 2005), pp. 1359–1364. ISSN: 0223-5234. DOI: 10.1016/j.ejmech.2005.07.013.

[31] Adnan A. Bekhit et al. "Tetrazolo[1,5-a]Quinoline as a Potential Promising New Scaffold for the Synthesis of Novel Anti-Inflammatory and Antibacterial Agents". In: *European Journal of Medicinal Chemistry* 39.3 (Mar. 2004), pp. 249–255. ISSN: 0223-5234. DOI: 10.1016/j.ejmech.2003.12.005.

[32] *Diversity and Proliferation of Metallo-β-Lactamases: A Clarion Call for Clinically Effective Metallo-β-Lactamase Inhibitors - PMC*. https://www.ncbi.nlm.nih.gov/pmc/articles. (Visited on 07/07/2023).

[33] *New Nonpeptide Angiotensin II Receptor Antagonists. 2. Synthesis, Biological Properties, and Structure-Activity Relationships of 2-Alkyl-4-(Biphenylylmethoxy)Quinoline Derivatives | Journal of Medicinal Chemistry*. https://pubs.acs.org/doi/10.1021/jm00100a007. (Visited on 07/07/2023).

[34] Junko Hotchi et al. “Plaque-Stabilizing Effect of Angiotensin-Converting Enzyme Inhibitor and/or Angiotensin Receptor Blocker in a Rabbit Plaque Model”. In: *Journal of Atherosclerosis and Thrombosis* advpub (2012), p. 14266. DOI: 10.5551/jat.14266.

[35] Jessica L Lee et al. “Serum Concentrations of Losartan Metabolites Correlate With Improved Physical Function in a Pilot Study of Prefrail Older Adults”. In: *The journals of gerontology Series A, Biological sciences and medical sciences* 77.12 (Dec. 2022), pp. 2356–2366. ISSN: 1758-535X. DOI: 10.1093/gerona/glac102. (Visited on 07/07/2023).

[36] Weifa Yu et al. “Synthesis and Crystal Structure of 2-Trifluoromethyl-1-[(2′-1H-tetrazole-5-yl-biphenyl-4-yl) Methyl]Benzimidazole”. In: *Journal of Chemical Crystallography* 34.9 (Sept. 2004), pp. 597–601. ISSN: 1572-8854. DOI: 10.1023/B:JOCC.0000044086.71468.e9. (Visited on 07/07/2023).

[37] Alan R. Katritzky, Charles W. Rees, and Eric F. V. Scriven, eds. *Comprehensive Heterocyclic Chemistry II: A Review of the Literature 1982-1995: The Structure, Reactions, Synthesis, and Uses of Heterocyclic Compounds*. 1st ed. Oxford ; New York: Pergamon, 1996. ISBN: 978-0-08-042072-1 978-0-08-042724-9 978-0-08-042725-6 978-0-08-042726-3 978-0-08-042727-0 978-0-08-042728-7 978-0-08-042729-4 978-0-08-042730-0 978-0-08-042731-7 978-0-08-042732-4 978-0-08-042965-6 978-0-08-042987-8.

[38] C. W. Thornber. “Isosterism and Molecular Modification in Drug Design”. In: *Chemical Society Reviews* 8.4 (Jan. 1979), pp. 563–580. ISSN: 1460-4744. DOI: 10.1039/CS9790800563. (Visited on 07/07/2023).

[39] Aleksei B. Sheremetev et al. “New Ring-Transformation Reaction: The Conversion of a Tetrazole Ring into a 1-Oxa-3,4-Diazine Ring”. In: *Mendeleev Communications* 19.2 (Mar. 2009), pp. 89–91. ISSN: 0959-9436. DOI: 10.1016/j.mencom.2009.03.012. (Visited on 07/07/2023).

[40] Ajay L. Chandgude and Alexander Dömling. “An Efficient Passerini Tetrazole Reaction (PT-3CR)”. In: *Green Chemistry* 18.13 (2016), pp. 3718–3721. DOI: 10.1039/C6GC00910G. (Visited on 07/07/2023).

[41] Christopher A. Lipinski. “Chapter 27. Bioisosterism in Drug Design”. In: *Annual Reports in Medicinal Chemistry*. Ed. by Denis M. Bailey. Vol. 21. Academic Press, Jan. 1986, pp. 283–291. DOI: 10.1016/S0065-7743(08)61137-9. (Visited on 07/07/2023).

[42] Ting Zhao et al. "$\alpha$-Amino Acid-Isosteric $\alpha$-Amino Tetrazoles". In: *Chemistry (Weinheim an Der Bergstrasse, Germany)* 22.9 (Feb. 2016), pp. 3009–3018. ISSN: 1521-3765. DOI: 10.1002/chem.201504520.

[43] *Heterocyclic Tetrazoles, a New Class of Lipolysis Inhibitors | Journal of Medicinal Chemistry*. https://pubs.acs.org/doi/10.1021/jm00314a004. (Visited on 07/07/2023).

[44] *Nonpeptide Angiotensin II Receptor Antagonists. Synthesis and Biological Activity of Potential Prodrugs of Benzimidazole-7-Carboxylic Acids | Journal of Medicinal Chemistry*. https://pubs.acs.org/doi/10.1021/jm00068a011. (Visited on 07/07/2023).

[45] M. T. Obermeier et al. "Prodrugs of BMS-183920: Metabolism and Permeability Considerations". In: *Journal of Pharmaceutical Sciences* 85.8 (Aug. 1996), pp. 828–833. ISSN: 0022-3549. DOI: 10.1021/js9600282.

[46] Piao He et al. "Alkali and Alkaline Earth Metal Salts of Tetrazolone: Structurally Interesting and Excellently Thermostable". In: *Dalton Transactions* 46.26 (July 2017), pp. 8422–8430. ISSN: 1477-9234. DOI: 10.1039/C7DT01179B. (Visited on 07/07/2023).

[47] Amin Ismael, Carlos Serpa, and M. Lurdes S. Cristiano. "Photochemistry of 1-Allyl-4-Aryltetrazolones in Solution; Structural Effects on Photoproduct Selectivity". In: *Photochemical & Photobiological Sciences* 12.2 (Jan. 2013), pp. 272–283. ISSN: 1474-9092. DOI: 10.1039/C2PP25210D. (Visited on 07/07/2023).

[48] A. Gómez-Zavaglia et al. "Molecular Structure, Vibrational Spectra and Photochemistry of 2-Methyl-2H-tetrazol-5-amine in Solid Argon". In: *The Journal of Physical Chemistry. A* 109.35 (Sept. 2005), pp. 7967–7976. ISSN: 1089-5639. DOI: 10.1021/jp0517706.

[49] A. Ismael et al. "Tautomer Selective Photochemistry in 1-(Tetrazol-5-Yl)Ethanol". In: *The Journal of Physical Chemistry. A* 114.50 (Dec. 2010), pp. 13076–13085. ISSN: 1520-5215. DOI: 10.1021/jp109215q.

[50] *Mechanistic Investigations into the Photochemistry of 4-Allyl-tetrazolones in Solution: A New Approach to the Synthesis of 3,4-Dihydro-pyrimidinones | The Journal of Organic Chemistry*. https://pubs.acs.org/doi/abs/10.1021/jo060164j. (Visited on 07/07/2023).

[51] M. J. Schocken et al. "Microbial Transformation of the Tetrazolinone Herbicide F5231". In: *Applied and Environmental Microbiology* 55.5 (May 1989), pp. 1220–1222. ISSN: 0099-2240. DOI: 10.1128/aem.55.5.1220-1222.1989.

[52] L. M. T. Frija et al. "UV-induced Photochemistry of Matrix-Isolated 1-Phenyl-4-Allyl-Tetrazolone". In: *Photochemical & Photobiological Sciences* 6.11 (Oct. 2007), pp. 1170–1176. ISSN: 1474-9092. DOI: 10.1039/B703961A. (Visited on 07/07/2023).

[53] Ian R. Dunkin, Charles J. Shields, and Helmut Quast. "The Photochemistry of 1,4-Dihtdro-5h-Tetrazole Derivatives Isolated in Low-Temperature Matrices". In: *Tetrahedron* 45.1 (Jan. 1989), pp. 259–268. ISSN: 0040-4020. DOI: 10.1016/0040-4020(89)80053-5. (Visited on 07/07/2023).

[54] *Clean Photodecomposition of 1-Methyl-4-phenyl-1H-tetrazole-5(4H)-Thiones to Carbodiimides Proceeds via a Biradical | The Journal of Organic Chemistry*. DOI: 10.1021/jo1019859. (Visited on 07/07/2023).

[55] Helmut Quast and Lothar Bieber. "Synthese und Photolyse von 1,4-Dialkyl-1,4-dihydro-5H-tetrazol-5-onen und -thionen: Neue Wege zu Diaziridinonen und Carbodiimiden1)". In: *Chemische Berichte* 114.10 (1981), pp. 3253–3272. ISSN: 1099-0682. DOI: 10.1002/cber.19811141007. (Visited on 07/07/2023).

[56] John A. Hyatt and John S. Swenton. "Facile Synthesis of 9H-pyrimido[4,5-b]Indoles from Photolysis of 8-Phenyltetrazolo[1,5-c]Pyrimidines in Acidic Media". In: *The Journal of Organic Chemistry* 37.21 (Oct. 1972), pp. 3216–3220. ISSN: 0022-3263. DOI: 10.1021/jo00986a005. (Visited on 07/07/2023).

[57] Helmut Quast, Andreas Fuss, and Wolfgang Nüdling. "Photoextrusion of Molecular Nitrogen from Annulated 5-Alkylidene-4,5-Dihydro-1H-tetrazoles: Annulated Iminoaziridines and the First Triplet Diazatrimethylenemethane". In: *European Journal of Organic Chemistry* 1998.2 (1998), pp. 317–327. ISSN: 1099-0690. DOI: 10.1002/(SICI)1099-0690(199802)1998:2{$<$}317::AID-EJOC317{$>$}3.0.CO;2-A. (Visited on 07/07/2023).

[58] Kyril M. Solntsev et al. "Photochemistry of "Super" Photoacids. 2. Excited-State Proton Transfer in Methanol/Water Mixtures". In: *The Journal of Physical Chemistry A* 104.19 (2000), p. 4658. ISSN: 1089-5639. (Visited on 07/07/2023).

[59] Luís Frija, I.V. Kmelinskii, and Maria Cristiano. "Novel Efficient Synthesis of 3,4-Dihydro-6-Substituted-3-Phenylpyrimidin-2-(1H)-Ones". In: *Tetrahedron Letters* 46 (Sept. 2005), pp. 6757–6760.

[60] Luís Miguel Teodoro Frija, Amin Ismael, and Maria Lurdes Santos Cristiano. "Photochemical Transformations of Tetrazole Derivatives: Applications in Organic Synthesis". In: *Molecules (Basel, Switzerland)* 15.5 (2010), p. 3757. ISSN: 14203049. DOI: 10.3390/MOLECULES15053757.

[61] Max Planck. "Ueber Das Gesetz Der Energieverteilung Im Normalspectrum". In: *Annalen der Physik* 309.3 (1901), pp. 553–563. ISSN: 1521-3889. DOI: 10.1002/andp.19013090310. (Visited on 07/08/2023).

[62] Ludwig Boltzmann. "Studien Über Das Gleichgewicht Der Lebendigen Kraft Zwischen Bewegten Materiellen Punkten". In: *Wissenschaftliche Abhandlungen*. Ed. by Friedrich Hasenöhrl. Cambridge University Press, Aug. 2012, pp. 49–96. ISBN: 978-1-108-05279-5 978-1-139-38142-0. DOI: 10.1017/CBO9781139381420.006. (Visited on 07/08/2023).

[63] Kelley Anne Myers. *Condensed-Phase Molecular Spectroscopy and Photophysics*. John Wiley  Sons 2013, 2013. ISBN: 9781118493052. DOI: DOI:10.1002/9781118493052.

[64] George C. Schatz and Mark A. Ratner. *Quantum Mechanics in Chemistry*. Courier Corporation, Jan. 2002. ISBN: 978-0-486-42003-5.

[65] *The Quantum Theory of the Emission and Absorption of Radiation | Proceedings of the Royal Society of London. Series A, Containing Papers of a Mathematical and Physical Character*. https://royalsocietypublishing.org/doi/10.1098/rspa.1927.0039. (Visited on 07/08/2023).

[66] S. J. Strickler and Robert A. Berg. "Relationship between Absorption Intensity and Fluorescence Lifetime of Molecules". In: *The Journal of Chemical Physics* 37.4 (July 2004), pp. 814–822. ISSN: 0021-9606. DOI: 10.1063/1.1733166. (Visited on 07/08/2023).

[67] David L. Andrews. *Molecular Photophysics and Spectroscopy*. Morgan & Claypool Publishers, Sept. 2014. ISBN: 978-1-62705-288-7. (Visited on 07/08/2023).

[68] *Radiative Lifetime of a BODIPY Dye as Calculated by TDDFT and EOM-CCSD Methods: Solvent and Vibronic Effects - Physical Chemistry Chemical Physics (RSC Publishing) DOI:10.1039/D1CP03775G*. (Visited on 07/08/2023).

[69] Shriver Atkins P.W. *Shriver Atkins' Inorganic Chemistry*. 5th ed. Oxford University Press, 2010. ISBN: 9780199236176.

[70] Yingli Niu et al. "Theory of excited state decays and optical spectra: Application to polyatomic molecules". In: *Journal of Physical Chemistry A* 114 (30 Aug. 2010), pp. 7817–7831. ISSN: 10895639. DOI: 10.1021/JP101568F/ASSET/IMAGES/MEDIUM/JP-2010-01568F_0022.GIF. URL: https://pubs.acs.org/doi/abs/10.1021/jp101568f.

[71] Katsuyuki Shizu and Hironori Kaji. "Theoretical Determination of Rate Constants from Excited-States: Application to Benzophenone". In: (May 2021). DOI: 10.26434/CHEMRXIV.14635569.V1. URL: https://chemrxiv.org/engage/chemrxiv/article-details/60c75906bb8c1ac4b33dcb45.

[72] Alyssa Chinen et al. "Nanoparticle Probes for the Detection of Cancer Biomarkers, Cells, and Tissues by Fluorescence". In: *Chemical reviews* 115 (Aug. 2015). DOI: 10.1021/acs.chemrev.5b00321.

[73] Shiro Koseki, Michael W. Schmidt, and Mark S. Gordon. "MCSCF/6-31G(d,p) calculations of one-electron spin-orbit coupling constants in diatomic molecules". In: *Journal of Physical Chemistry* 96 (26 1992), pp. 10768–10772. ISSN: 00223654. DOI: 10.1021/J100205A033/ASSET/J100205A033.FP.PNG_V03. URL: https://pubs.acs.org/doi/abs/10.1021/j100205a033.

[74] David J Griffiths. *Introduction to Electrodynamics*. 4th ed. Cambridge University Press, 2017. ISBN: 9781108420419. DOI: DOI:10.1017/9781108333511.

[75] J. D. Jackson. "Electrodynamics, Classical". In: *digital Encyclopedia of Applied Physics*. John Wiley Sons, Ltd, 2003. ISBN: 9783527600434. DOI: https://doi.org/10.1002/3527600434.eap109.

[76] André D. Bandrauk, El Wallid S. Sedik, and Chérif F. Matta. "Effect of absolute laser phase on reaction paths in laser-induced chemical reactions". In: *The Journal of Chemical Physics* 121 (16 Oct. 2004), p. 7764. ISSN: 0021-9606. DOI: 10.1063/1.1793931. URL: https://aip.scitation.org/doi/abs/10.1063/1.1793931.

[77] P. Fuentealba, Y. Simón-Manso, and Pratim K. Chattaraj. "Molecular electronic excitations and the minimum polarizability principle". In: *Journal of Physical Chemistry A* 104 (14 Apr. 2000), pp. 3185–3187. ISSN: 10895639. DOI: 10.1021/JP992973V/ASSET/

IMAGES/MEDIUM/JP992973VE00004.GIF. URL: https://pubs.acs.org/doi/full/10.1021/jp992973v.

[78] Sourav Pal and Sophy K B. "Density functional response approach for electric properties of molecules". In: Oct. 2005.

[79] Robert G. Parr and Pratim K. Chattaraj. "Principle of maximum hardness". In: *Journal of the American Chemical Society* 113.5 (Feb. 1991), pp. 1854–1855. ISSN: 0002-7863. DOI: 10.1021/ja00005a072. URL: https://doi.org/10.1021/ja00005a072.

[80] P. Fuentealba and O. Reyes. "Atomic softness and the electric dipole polarizability". In: *Journal of Molecular Structure: THEOCHEM* 282.1 (1993), pp. 65–70. ISSN: 0166-1280. DOI: https://doi.org/10.1016/0166-1280(93)85035-W. URL: https://www.sciencedirect.com/science/article/pii/016612809385035W.

[81] Tapan K. Ghanty and Swapan K. Ghosh. "Correlation between hardness, polarizability, and size of atoms, molecules, and clusters". In: *The Journal of Physical Chemistry* 97.19 (May 1993), pp. 4951–4953. ISSN: 0022-3654. DOI: 10.1021/j100121a015. URL: https://doi.org/10.1021/j100121a015.

[82] Bernardo De Souza et al. "Predicting Phosphorescence Rates of Light Organic Molecules Using Time-Dependent Density Functional Theory and the Path Integral Approach to Dynamics". In: *Journal of Chemical Theory and Computation* 15 (3 Mar. 2019), pp. 1896–1904. ISSN: 15499626. DOI: 10.1021/ACS.JCTC.8B00841/SUPPL_FILE/CT8B00841_SI_001.PDF. URL: https://pubs.acs.org/doi/full/10.1021/acs.jctc.8b00841.

[83] Bernardo De Souza, Frank Neese, and Róbert Izsák. "On the theoretical prediction of fluorescence rates from first principles using the path integral approach". In: *The Journal of Chemical Physics* 148 (3 Jan. 2018), p. 034104. ISSN: 0021-9606. DOI: 10.1063/1.5010895. URL: https://aip.scitation.org/doi/abs/10.1063/1.5010895.

[84] Alberto Baiardi, Julien Bloino, and Vincenzo Barone. "General Time Dependent Approach to Vibronic Spectroscopy Including Franck–Condon, Herzberg–Teller, and Duschinsky Effects". In: *Journal of Chemical Theory and Computation* 9.9 (Sept. 2013), pp. 4097–4115. ISSN: 1549-9618. DOI: 10.1021/ct400450k. (Visited on 02/17/2023).

[85] Baldassare Di Bartolo and Velda Goldberg. *Radiationless Processes*. Springer Science & Business Media, Dec. 2012. ISBN: 978-1-4613-3174-2.

[86] Ming-Chung Li, Michitoshi Hayashi, and Sheng-Hsien Lin. "Quantum Chemistry Study on Internal Conversion of Diphenyldibenzofulvene in Solid Phase". In: *The Journal of Physical Chemistry A* 115.50 (Dec. 2011), pp. 14531–14538. ISSN: 1089-5639. DOI: 10.1021/jp208199t. (Visited on 02/22/2023).

[87] R. A. Marcus. "On the Theory of Oxidation-Reduction Reactions Involving Electron Transfer. I". In: *The Journal of Chemical Physics* 24.5 (May 1956), pp. 966–978. ISSN: 0021-9606. DOI: 10.1063/1.1742723. (Visited on 02/22/2023).

[88] R. A. Marcus. "On the Theory of Oxidation-Reduction Reactions Involving Electron Transfer. II. Applications to Data on the Rates of Isotopic Exchange Reactions". In: *The Journal of Chemical Physics* 26.4 (Apr. 1957), pp. 867–871. ISSN: 0021-9606. DOI: 10.1063/1.1743423. (Visited on 02/22/2023).

[89] *AppliedMath | Free Full-Text | Signatures of Duschinsky Rotation in Femtosecond Coherence Spectra*. https://www.mdpi.com/2673-9909/2/4/39. (Visited on 07/08/2023).

[90] Qian Peng et al. "Toward Quantitative Prediction of Molecular Fluorescence Quantum Efficiency: Role of Duschinsky Rotation". In: *Journal of the American Chemical Society* 129.30 (Aug. 2007), pp. 9333–9339. ISSN: 0002-7863. DOI: 10.1021/ja067946e. (Visited on 02/22/2023).

[91] "FRONT MATTER". In: *Advanced Series in Physical Chemistry*. Vol. 15. WORLD SCIENTIFIC, July 2004, pp. i–xvii. ISBN: 978-981-238-672-4 978-981-256-546-4. DOI: 10.1142/9789812565464_fmatter. (Visited on 07/08/2023).

[92] Fabrizio Santoro et al. "Effective Method for the Computation of Optical Spectra of Large Molecules at Finite Temperature Including the Duschinsky and Herzberg-Teller Effect: The Qx Band of Porphyrin as a Case Study". In: *The Journal of Chemical Physics* 128.22 (June 2008), p. 224311. ISSN: 1089-7690. DOI: 10.1063/1.2929846.

[93] Katsuyuki Shizu, Chihaya Adachi, and Hironori Kaji. "Effect of Vibronic Coupling on Correlated Triplet Pair Formation in the Singlet Fission Process of Linked Tetracene Dimers". In: *Journal of Physical Chemistry A* 124 (18 May 2020), pp. 3641–3651. ISSN: 15205215. DOI: 10.1021/ACS.JPCA.0C03041/ASSET/IMAGES/LARGE/JP0C03041_0007.JPEG. URL: https://pubs.acs.org/doi/full/10.1021/acs.jpca.0c03041.

[94] F. Neese. *Software update: the ORCA program system, version 4.0,* 5th ed. Wiley Interdiscip., 2017.

[95] J. Hubbard and Rudolf Ernst Peierls. "The Description of Collective Motions in Terms of Many-Body Perturbation Theory". In: *Proceedings of the Royal Society of London. Series A. Mathematical and Physical Sciences* 240.1223 (Jan. 1997), pp. 539–560. DOI: 10.1098/rspa.1957.0106. (Visited on 07/08/2023).

[96] Fabrizio Santoro, Chiara Cappelli, and Vincenzo Barone. "Effective Time-Independent Calculations of Vibrational Resonance Raman Spectra of Isolated and Solvated Molecules Including Duschinsky and Herzberg–Teller Effects". In: *Journal of Chemical Theory and Computation* 7.6 (2011), p. 1824. ISSN: 1549-9618. (Visited on 07/08/2023).

[97] N. Zettili. *Quantum Mechanics, Concepts and Applications*. Wiley, Chichester, 2001.

[98] Barton Zwiebach. "Mastering quantum mechanics essentials, theory and applications". In: Cambridge: MIT Press, 2022. ISBN: 9780262046138.

[99] Anna I. Krylov. "Time-Dependent Density Functional Theory. From the series: Lecture Notes in Physics, Volume 706 Edited by Miguel A. L. Marques (Universidade de Coimbra, Portugal), Carsten A. Ullrich (University of Missouri-Columbia, MO), Fernando Nogueira (Universidade de Coimbra), Angel Rubio (Universidad del País Vasco, San Sebastián, Spain), Kieron Burke (Rutgers University, Piscataway, NJ), and Eberhard K. U. Gross (Freie Universität, Berlin, Germany). Springer: Berlin, Heidelberg, New York. 2006 ISBN 3-540-35422-0." In: *Journal of the American Chemical Society* 129.21 (May 2007), pp. 6962–6962. ISSN: 0002-7863. DOI: 10.1021/ja069829p. URL: https://doi.org/10.1021/ja069829p.

[100] Wolfram Koch and Max C. Holthausen. "A Chemist's Guide to Density Functional Theory, 2nd Edition". In: WILEY-VCH, 2001. ISBN: 9783527303724.

[101] Frank Jensen. *Introduction to Computational Chemistry*. Third edition. Chichester West Sussex, UK: John Wiley & Sons, Ltd., 2017. ISBN: 978-1-118-82599-0.

[102] John F. Stanton. "A Chemist's Guide to Density Functional Theory By Wolfram Koch (German Chemical Society, Frankfurt Am Main) and Max C. Holthausen (Humbolt University Berlin). Wiley-VCH: Weinheim. 2000 ISBN 3-527-29918-1". In: *Journal of the American Chemical Society* 123.11 (Mar. 2001), pp. 2701–2701. ISSN: 0002-7863. DOI: 10.1021/ja004799q. (Visited on 07/08/2023).

[103] Nandor L. Balazs. "Thomas-Fermi Theory of the Atom as a Solution of the Density-Matrix Hierarchy". In: *Physical Review* 134.4A (May 1964), A841–A852. DOI: 10.1103/PhysRev.134.A841. (Visited on 07/08/2023).

[104] Miguel Marques et al. "Time-Dependent Density Functional Theory". In: *Lecture Notes in Physics* 706 (Jan. 2006). ISSN: 978-3-540-35422-2. DOI: 10.1007/b11767107.

[105] *Studies in surface science and catalysis*. Elsevier Scientific Pub. (Visited on 07/08/2023).

[106] P. Hohenberg and W. Kohn. "Inhomogeneous Electron Gas". In: *Physical Review* 136.3B (Nov. 1964), B864–B871. DOI: 10.1103/PhysRev.136.B864. (Visited on 07/08/2023).

[107] W. Kohn and L. J. Sham. "Self-Consistent Equations Including Exchange and Correlation Effects". In: *Physical Review* 140.4A (Nov. 1965), A1133–A1138. DOI: 10.1103/PhysRev.140.A1133. (Visited on 07/08/2023).

[108] Miguel A. L. Marques, Micael J. T. Oliveira, and Tobias Burnus. "Libxc: A Library of Exchange and Correlation Functionals for Density Functional Theory". In: *Computer Physics Communications* 183.10 (Oct. 2012), pp. 2272–2281. ISSN: 00104655. DOI: 10.1016/j.cpc.2012.05.007. arXiv: 1203.1739 [cond-mat, physics:physics]. (Visited on 07/08/2023).

[109] John P. Perdew and Karla Schmidt. "Jacob's Ladder of Density Functional Approximations for the Exchange-Correlation Energy". In: 577 (July 2001), pp. 1–20. DOI: 10.1063/1.1390175. (Visited on 07/08/2023).

[110] *Effective Molecular Descriptors for Chemical Accuracy at DFT Cost: Fragmentation, Error-Cancellation, and Machine Learning | Journal of Chemical Theory and Computation*. https://pubs.acs.org/doi/10.1021/acs.jctc.0c00236. (Visited on 07/08/2023).

[111] J. Tao et al. "Meta-Generalized Gradient Approximation: Non-empirical Construction and Performance of a Density Functional". In: *Philosophical Magazine* 87 (Mar. 2007), pp. 1071–1084. DOI: 10.1080/14786430601021660.

[112] J. P. Perdew, K. Burke, and M. Ernzerhof. "Generalized Gradient Approximation Made Simple". In: *Physical Review Letters* 77.18 (Oct. 1996), pp. 3865–3868. ISSN: 1079-7114. DOI: 10.1103/PhysRevLett.77.3865.

[113] John P. Perdew et al. "Atoms, Molecules, Solids, and Surfaces: Applications of the Generalized Gradient Approximation for Exchange and Correlation". In: *Physical Review B* 46.11 (Sept. 1992), pp. 6671–6687. DOI: 10.1103/PhysRevB.46.6671. (Visited on 07/08/2023).

[114] Axel D. Becke. "Density-functional Thermochemistry. I. The Effect of the Exchange-only Gradient Correction". In: *The Journal of Chemical Physics* 96.3 (Feb. 1992), pp. 2155–2160. ISSN: 0021-9606. DOI: 10.1063/1.462066. (Visited on 07/08/2023).

[115] B. Hammer, K. W. Jacobsen, and J. K. Nørskov. "Role of Nonlocal Exchange Correlation in Activated Adsorption". In: *Physical Review Letters* 70.25 (June 1993), pp. 3971–3974. DOI: 10.1103/PhysRevLett.70.3971. (Visited on 07/08/2023).

[116] D. R. Hamann. "Generalized Gradient Theory for Silica Phase Transitions". In: *Physical Review Letters* 76.4 (Jan. 1996), pp. 660–663. DOI: 10.1103/PhysRevLett.76.660. (Visited on 07/08/2023).

[117] *Distributions and Averages of Electron Density Parameters: Explaining the Effects of Gradient Corrections | The Journal of Chemical Physics*. https://pubs.aip.org/aip/jcp/article. (Visited on 07/08/2023).

[118] Mauricio Palafox. "DFT Computations on Vibrational Spectra: Scaling Procedures to Improve the Wavenumbers". In: *Physical Sciences Reviews* 3 (May 2018). DOI: 10.1515/psr-2017-0184.

[119] F. Zahariev, S. S. Leang, and Mark S. Gordon. "Functional Derivatives of Meta-Generalized Gradient Approximation (Meta-GGA) Type Exchange-Correlation Density Functionals". In: *The Journal of Chemical Physics* 138.24 (2013), p. 244108. ISSN: 0021-9606. (Visited on 07/08/2023).

[120] Jianwei Sun et al. "SCAN: An Efficient Density Functional Yielding Accurate Structures and Energies of Diversely-Bonded Materials". In: (Nov. 2015).

[121] Carlo Adamo, Matthias Ernzerhof, and Gustavo E. Scuseria. "The Meta-GGA Functional: Thermochemistry with a Kinetic Energy Density Dependent Exchange-Correlation Functional". In: *The Journal of Chemical Physics* 112.6 (Feb. 2000), pp. 2643–2649. ISSN: 0021-9606. DOI: 10.1063/1.480838. (Visited on 07/08/2023).

[122] *Exchange-Correlation Functionals: GGA vs. Meta-GGA - Maple Application Center*. https://www.maplesoft.com/Applications/Detail.aspx?id=154757. (Visited on 07/08/2023).

[123] Sérgio Filipe Sousa, Pedro Alexandrino Fernandes, and Maria João Ramos. "General Performance of Density Functionals". In: *The Journal of Physical Chemistry A* 111.42 (Oct. 2007), pp. 10439–10452. ISSN: 1089-5639. DOI: 10.1021/jp0734474. (Visited on 07/08/2023).

[124] *A New Mixing of Hartree–Fock and Local Density-functional Theories | The Journal of Chemical Physics | AIP Publishing.* https://pubs.aip.org/aip/jcp/article. (Visited on 07/08/2023).

[125] Amilcar Duque-Prata, Carlos Serpa, and Pedro J.S.B. Caridade. "Photochemistry of 1-Phenyl-4-Allyl-Tetrazol-5-One: A Theoretical Study Contribution towards Mechanism Elucidation". In: *Applied Sciences 2021, Vol. 11, Page 4045* 11 (9 Apr. 2021), p. 4045. ISSN: 2076-3417. DOI: 10.3390/APP11094045. URL: https://www.mdpi.com/2076-3417/11/9/4045/htm%20https://www.mdpi.com/2076-3417/11/9/4045.

[126] Robert van Leeuwen. "Causality and Symmetry in Time-Dependent Density-Functional Theory". In: *Physical Review Letters* 80.6 (Feb. 1998), pp. 1280–1283. DOI: 10.1103/PhysRevLett.80.1280. (Visited on 07/08/2023).

[127] Richard M. Martin. *Electronic Structure: Basic Theory and Practical Methods.* Cambridge: Cambridge University Press, 2004. ISBN: 978-0-521-78285-2. DOI: 10.1017/CBO9780511805769. (Visited on 07/08/2023).

[128] Saul T. Epstein. "Time-Dependent Hellmann—Feynman Theorems for Variational Wavefunctions". In: *The Journal of Chemical Physics* 45.1 (May 2004), p. 384. ISSN: 0021-9606. DOI: 10.1063/1.1727339. (Visited on 07/08/2023).

[129] Philip Hoggan, Maria Belen Ruiz Ruiz, and T. Özdoğan. "Molecular Integrals over Slater-Type Orbitals. From Pioneers to Recent Developments". In: *Quantum Frontiers of Atoms and Molecules* (Jan. 2011), pp. 61–89.

[130] Yves Maréchal. "Methods to Observe and Describe H-Bonds". In: Dec. 2007, pp. 49–75. ISBN: 978-0-444-51957-3. DOI: 10.1016/B978-044451957-3.50004-4.

[131] *Estimated Adiabatic Ionization Energies for Organic Compounds Using the Gaussian-4 (G4) and W1BD Theoretical Methods | Journal of Chemical & Engineering Data.* https://pubs.acs.org/doi/10.1021/je100913f. (Visited on 07/08/2023).

[132] *Principles and Applications of Quantum Chemistry - 1st Edition.* (Visited on 07/08/2023).

[133] *Spin–Vibronic Model for Quantitative Prediction of Reverse Intersystem Crossing Rate in Thermally Activated Delayed Fluorescence Systems | Journal of Chemical Theory and Computation*. https://pubs.acs.org/doi/10.1021/acs.jctc.9b01014. (Visited on 07/08/2023).

[134] Zheng Gao et al. "A Fluorescent Dye with Large Stokes Shift and High Stability: Synthesis and Application to Live Cell Imaging". In: *RSC Advances* 7.13 (2017), pp. 7604–7609. DOI: 10.1039/C6RA27547H. (Visited on 07/08/2023).

[135] Rebaz Omer et al. "Impact of Solvent Polarity on the Molecular Properties of Dimetridazole". In: *El-Cezeri* 9.2 (May 2022), pp. 740–747. ISSN: 2148-3736, 2148-3736. DOI: 10.31202/ecjse.1000757. (Visited on 07/08/2023).

[136] Amílcar Duque Prata. *Fotoquímica de tetrazolonas Um Estudo Teórico*. 2020.

# Appendix A

# Supplementary Information

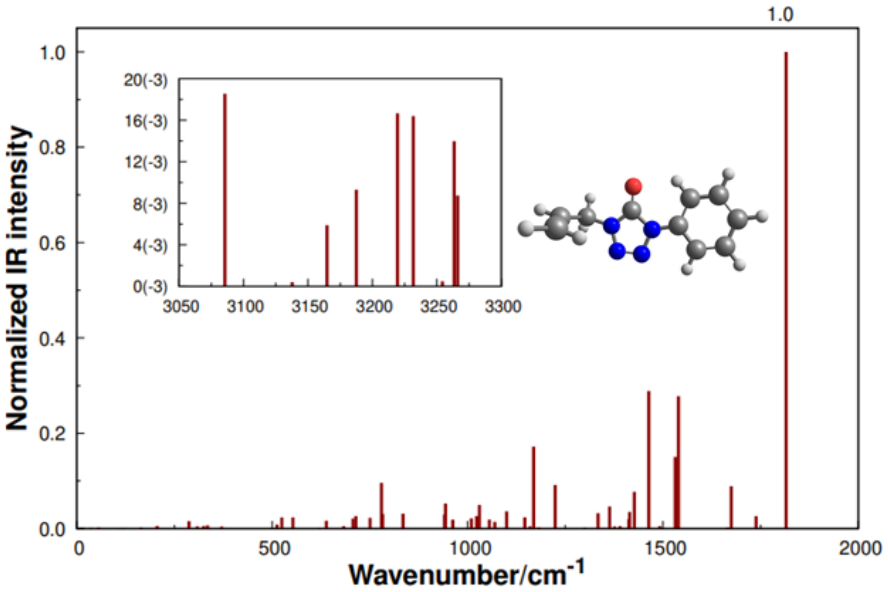


Figure A.1: Normalized vibrational spectrum of ATZ-$S_1$ in methanol.

Table A.1: Energy of the molecular orbitals of ATZ-$S_0$, ATZ-$S_1$ and ATZ-$T_1$ (in eV).

| **Electronic state** | **Molecular Orbitals** | **Excitation energy (eV)** |
|---|---|---|
| $S_0$ | HOMO-LUMO | 5.7138 |
| $S_0$ | HOMO-1 - LUMO+1 | 7.1608 |
| $S_1$ | HOMO-LUMO | 5.3255 |
| $S_1$ | HOMO-1 - LUMO+1 | 6.83 |
| $T_1$ | HOMO-LUMO | 2.693 |
| $T_1$ | HOMO-1 - LUMO+1 | 6.6928 |

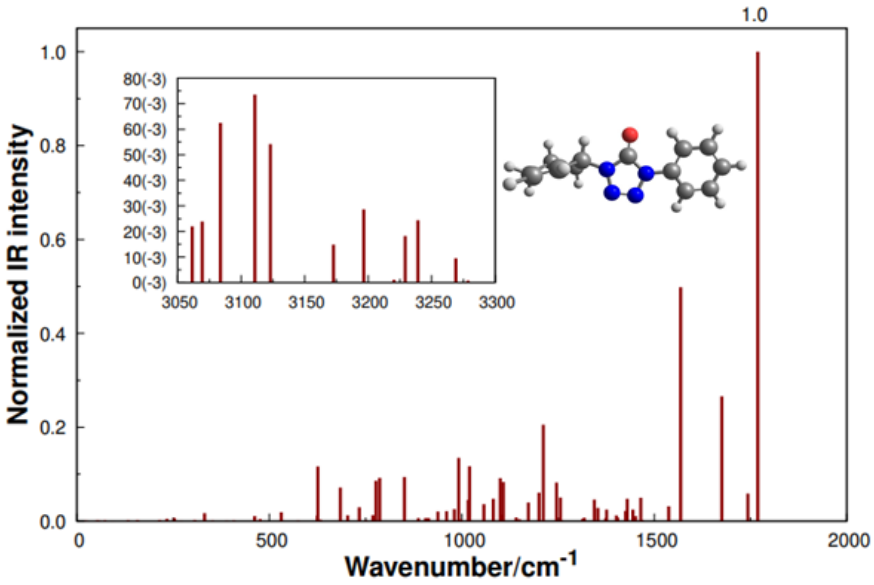


Figure A.2: Normalized vibrational spectrum of ATZ-$S_1$ in methanol.

Table A.2: Energy of the molecular orbitals of CTZ-$S_0$, CTZ-$S_1$ and CTZ-$T_1$ (in eV).

| **Electronic state** | **Molecular Orbitals** | **Excitation energy (eV)** |
|---|---|---|
| $S_0$ | HOMO-LUMO | 5.682 |
| $S_0$ | HOMO-1 - LUMO+1 | 6.787 |
| $S_1$ | HOMO-LUMO | 5.671 |
| $S_1$ | HOMO-1 - LUMO+1 | 6.791 |
| $T_1$ | HOMO-LUMO | 2.181 |
| $T_1$ | HOMO-1 - LUMO+1 | 6.597 |

Table A.3: Energy of the molecular orbitals of 3CTZ-$S_0$, 3CTZ-$S_1$ and 3CTZ-$T_1$ (in eV).

| **Electronic state** | **Molecular Orbitals** | **Excitation energy (eV)** |
|---|---|---|
| $S_0$ | HOMO-LUMO | 5.752 |
| $S_0$ | HOMO-1 - LUMO+1 | 6.922 |
| $S_1$ | HOMO-LUMO | 4.845 |
| $S_1$ | HOMO-1 - LUMO+1 | 7.045 |
| $T_1$ | HOMO-LUMO | 2.138 |
| $T_1$ | HOMO-1 - LUMO+1 | 6.691 |

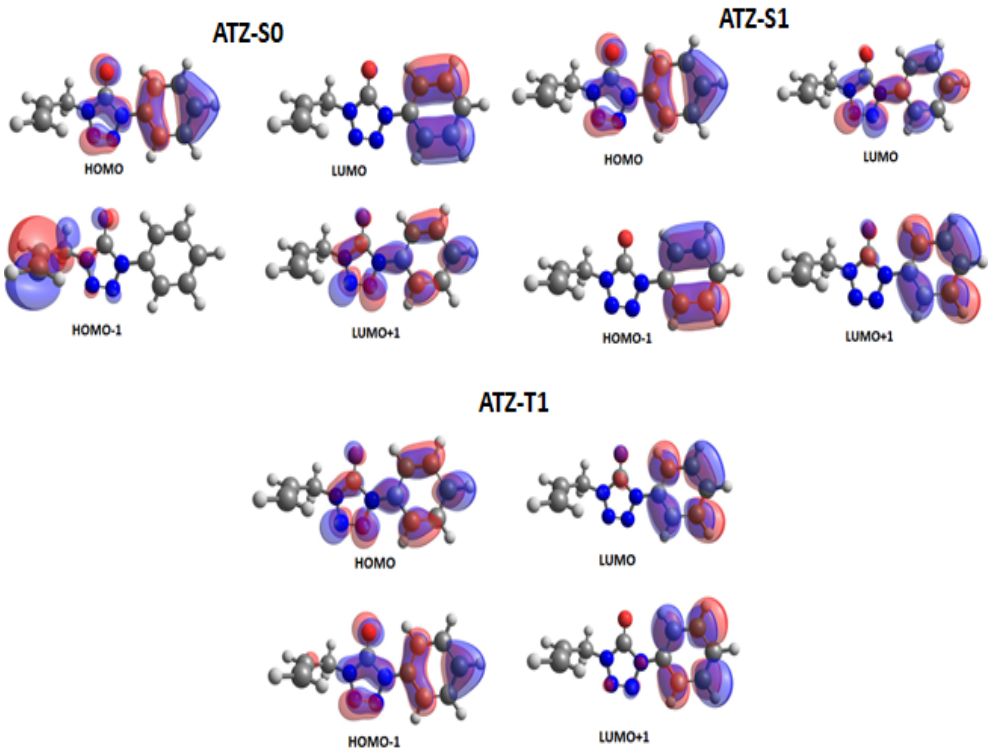


Figure A.3: Schematic representation of the HOMO-LUMO and HOMO-1-LUMO+1 molecular orbitals of ATZ.

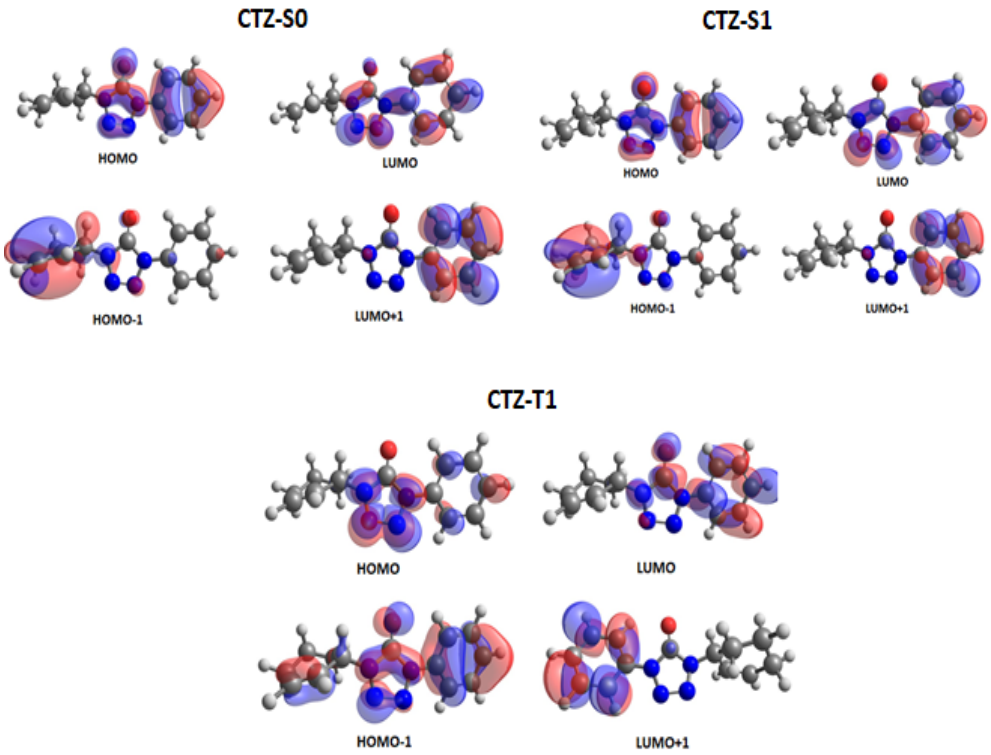


Figure A.4: Schematic representation of the HOMO-LUMO and HOMO-1-LUMO+1 molecular orbitals of CTZ.

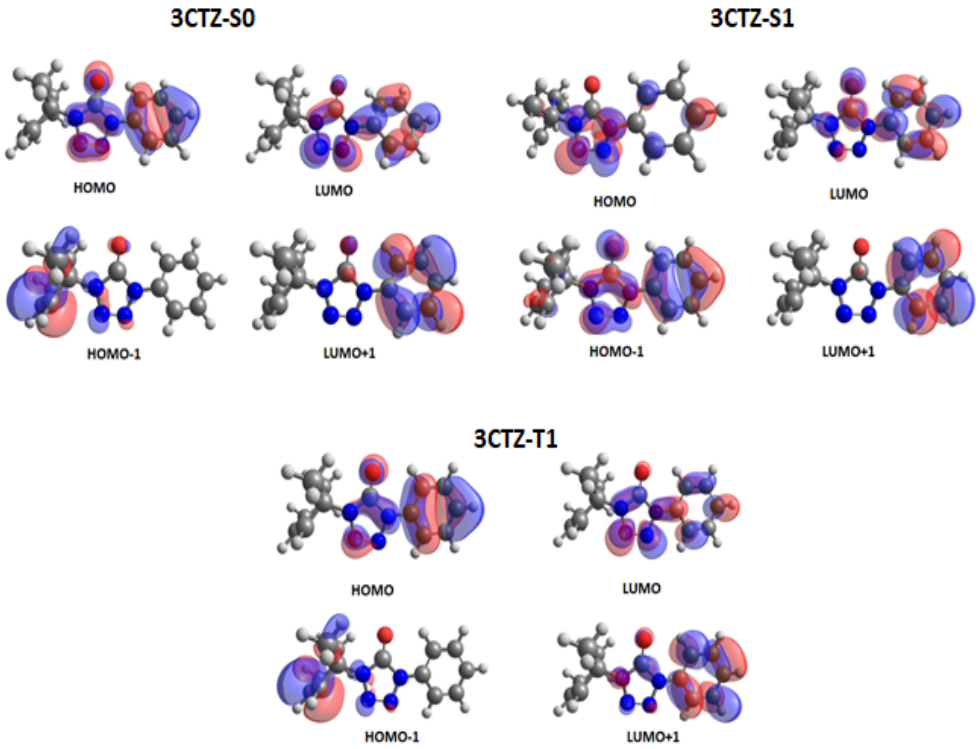


Figure A.5: Schematic representation of the HOMO-LUMO and HOMO-1-LUMO+1 molecular orbitals of 3CTZ.

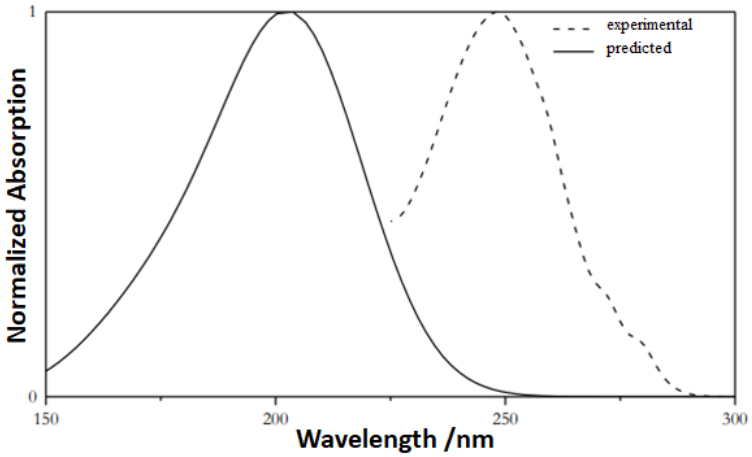


Figure A.6: Experimental $UV_{vis}$ absorption spectrum of ATZ in methanol, adapted from [136]

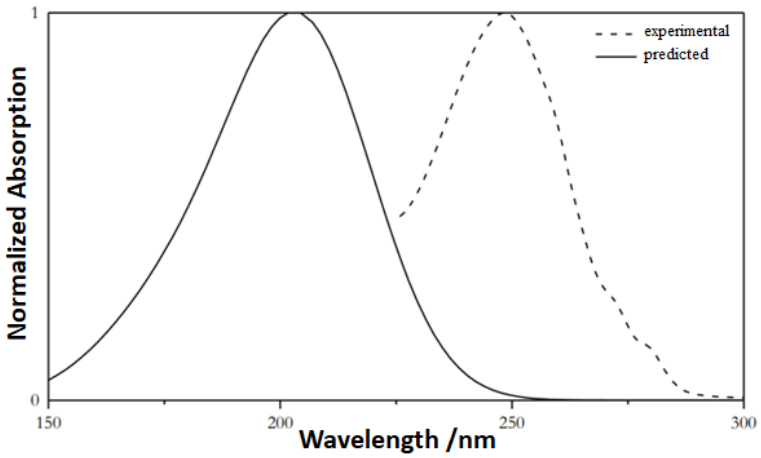


Figure A.7: Experimental $UV_{vis}$ absorption spectrum of CTZ in methanol, adapted from [136]

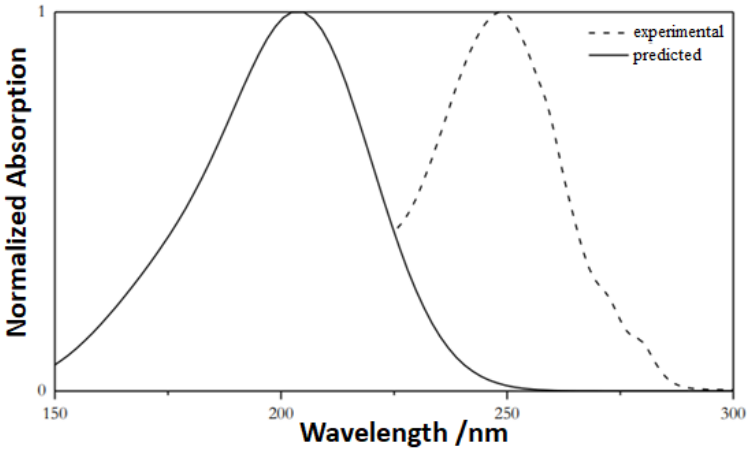


Figure A.8: Experimental $UV_{vis}$ absorption spectrum of 3CTZ in methanol, adapted from [136]

Table A.4: Physical parameters for rate constant computation with FSTF.

| | **ATZ** |
|---|---|
| $E_{kl_{(S_1-S_0)}}$ | 0.1843 Eh |
| $E_{kl_{(T_1-S_0)}}$ | 0.124 Eh |
| $E_{kl_{(T_1-S_1)}}$ | 0.060 Eh |
| $\gamma$ | 47nm |
| $M_{S_1-S_0}$ | $1.8 \times 10^{-4}$ a.u |
| $M_{T_1-S_0}$ | $1.72 \times 10^{-4}$ a.u |
| | **CTZ** |
| $E_{kl_{(S_1-S_0)}}$ | 0.1657 Eh |
| $E_{kl_{(T_1-S_0)}}$ | 0.11 Eh |
| $E_{kl_{(T_1-S_1)}}$ | 0.0547 Eh |
| $\gamma$ | 136nm |
| $M_{S_1-S_0}$ | $1.67 \times 10^{-4}$ a.u |
| $M_{T_1-S_0}$ | $1.18 \times 10^{-6}$ a.u |
| | **3CTZ** |
| $E_{kl_{(S_1-S_0)}}$ | 0.167 Eh |
| $E_{kl_{(T_1-S_0)}}$ | 0.112 Eh |
| $E_{kl_{(T_1-S_1)}}$ | 0.0558 Eh |
| $\gamma$ | 109nm |
| $M_{S_1-S_0}$ | $2.1 \times 10^{-4}$ a.u |
| $M_{T_1-S_0}$ | $2.1 \times 10^{-4}$ a.u |

Table A.5: Physical constants for unit conversion for FSTF method.

| | **Conversion factor** |
|---|---|
| eV $\rightarrow$ J | $1\text{eV} = 1.60217663 \cdot 10^{-19}\text{J}$ |
| $\text{cm}^{-1} \rightarrow$ J | $1\text{cm}^{-1} = 1.986 \cdot 10^{-23}\text{J}$ |
| a.u $\rightarrow \text{s}^{-1}$ | $1\text{a.u} = 2.41888425 \cdot 10^{-17}\text{s}$ |
| Eh $\rightarrow$ eV | 1Eh = 27.211eV |